# In the foreground

## Steps towards a clear view on the Cosmic Microwave Background

Ph.D. thesis by Sebastian von Hausegger

Cover figure: *No.8*, Mark Rothko.
From https://szeifertjudit.files.wordpress.com/2016/01/mark-rothko-no-8-1952.jpg

# In the foreground

**Steps towards a clear view on the Cosmic Microwave Background**

Sebastian von Hausegger

Niels Bohr Institute & Discovery Center,
University of Copenhagen

January 15th, 2019

Academic supervisor: Pavel Naselsky

This thesis has been submitted to the Ph.D. school
at the Faculty of Science, University of Copenhagen

# Contents


Abstract . . . . . 4
Acknowledgements . . . . . 6

**1 Introduction** **10**
1.1 Cosmology through the eyes of the CMB . . . . . 10
1.1.1 Thermodynamics and cosmic radiation . . . . . 11
1.1.2 Observation I . . . . . 12
1.1.3 Theoretical description and motivation . . . . . 14
1.1.4 Observables . . . . . 19
1.1.5 Unveiling the CMB . . . . . 23
1.1.6 Observation II . . . . . 30
1.2 Galactic microwaves . . . . . 32
1.2.1 Galactic radio continuum emission . . . . . 32
1.2.2 Millimeter and infrared emission . . . . . 36
1.2.3 Other components . . . . . 38
1.3 Summary . . . . . 42

**2 The imperfect CMB sky — Galactic Radio Loops** **44**
2.1 The Galactic radio loops . . . . . 44
2.2 Galactic Radio Loop I in the CMB . . . . . 47
2.2.1 Loop I in Planck CMB maps . . . . . 48
2.2.2 Physical reasoning . . . . . 51
2.3 Planck's response . . . . . 54
2.4 Loops and filaments . . . . . 55
2.4.1 Loop I and the filaments . . . . . 56
2.4.2 Loop IIIs . . . . . 60
2.5 Temporary conclusion . . . . . 62

**3 Evaluation of Planck's foreground separation products** **64**
3.1 Dust and the Cosmic Infrared Background . . . . . 65
3.1.1 Are comparisons among smoothed parameter maps sensible? . . . . . 66
3.1.2 Full-sky comparison . . . . . 67
3.1.3 Focusing on selected regions . . . . . 71

3.1.4 Extrapolating to CMB frequencies . . . 74
3.1.5 Discussion . . . 74
3.2 Anomalous Microwave Emission . . . 77
3.2.1 Mosaic Correlation . . . 78
3.2.2 Weighted Mosaic Correlation . . . 80
3.2.3 Discussion . . . 81

**4 Statistics of foreground maps 84**
4.1 Motivation . . . 85
4.2 Method . . . 88
4.2.1 Skewness, kurtosis and non-Gaussianity . . . 89
4.2.2 Uncorrelated vs. Correlated Data . . . 91
4.3 Analysis of sky maps — Temperature . . . 93
4.3.1 The SMICA Map . . . 93
4.3.2 The Haslam map . . . 94
4.4 Intermediate discussion . . . 100
4.5 Analysis of sky maps — Polarization . . . 103
4.5.1 Skewness and kurtosis . . . 103
4.5.2 Correlations . . . 105
4.6 Discussion . . . 107

**5 $E$- and $B$-mode decomposition on partial skies 110**
5.1 Background . . . 111
5.2 A new method for $E/B$ leakage correction . . . 113
5.2.1 Collecting $E$ and $B$ modes in the Stokes parameters . . . 113
5.2.2 Formulating the method . . . 116
5.2.3 Examples and comparison . . . 118
5.2.4 Advantages of correction in pixel domain . . . 121
5.3 Testing the level of residual after correction . . . 121
5.3.1 Zero initial B-mode . . . 122
5.3.2 Combination with the MASTER method . . . 122
5.3.3 Optimization of the posterior pixel domain apodization . . . 125
5.4 Discussion . . . 128

**6 Closing remarks 130**

**A Appendix 134**
A.1 CMB units . . . 134
A.2 Additional tables . . . 135
A.3 Additional figures . . . 136

**References 136**
More Acknowledgements . . . 156

# Abstract

The Cosmic Microwave Background is one of the strongest probes of the cosmological history of our Universe. Several experiments from ground as well as from space continue to perform measurements of the CMB with increasing sensitivity. As the detected signal contains bright microwave emission from our Galaxy as well, the careful separation of the foreground from the background becomes a delicate act. Approaching the subject from different perspectives, I argue that the physical mechanisms of foregrounds must be better understood before attempting the most ambitious measurements of primordial physics.

Residual emission from Galactic Radio Loop I in current CMB maps occupies the first chapter, where I present evidence for and arguments against its existence. I then counter these objections with further studies and discuss my findings at length. Inconsistencies also exist within different products of foreground maps as shown in the second chapter. Both chapters hint towards problems with the inherent assumptions about foreground spectra in component separation techniques. In the third chapter I explore statistics of foregrounds both in temperature and polarization. The conclusions, that foreground emission can be treated as a Gaussian process on certain scales, have positive implications for foreground simulations. Lastly, I present a method for improved treatment of polarized data on incomplete skies, which, when compared with state-of-the-art solutions performs better by orders of magnitude.

In brief, in this thesis I highlight problems in our current treatment of Galactic foregrounds at low and high frequencies by concrete examples, I argue for studying foregrounds' statistics and present such investigations, and further propose methods for the analysis of polarized data.

## Acknowledgements

I was first introduced to Cosmology at University level in courses by Niels Obers and my supervisor, Pavel Naselsky, to whom both I am grateful for the ongoing fun and excitement I experience in this field. In particular Pavel has guided me from the beginning into becoming a CMB scientist and has not left out an opportunity to increase my knowledge, be it through spontaneous in-office lectures or establishing contact to other researchers. His unconventional conceptions have accustomed me to maintain a steady suspicion in the most honest way.

I also want to express my gratitude to the Cosmologists at the Niels Bohr Institute with whom I had and have the pleasure to work, as well as from whom I was and still am able to learn:

I am thankful for all the amusing chats and interesting discussions with Andy Jackson, and the advice he has given me over the past years. His scientific enthusiasm and kind nature are truly remarkable, even at NBI. I am also grateful to Subir Sarkar, whose ideas and intellectual approach are inspiring, and who always took time for entertaining pop-up lectures. It is Pavel, Andy and Subir who have most shaped my way of thinking during these years, and I consider myself lucky to have had an environment like this.

While for a long period I had the luxury of having an office of my own, sharing the office with Anne-Mette and James has been the most pleasant and at some occasions even more productive! I also thank Amel, with whom I unfortunately never shared an office, for many fun discussions about a broad range of topics in physics and outside, and Hao for teaching me the basics of CMB data analysis and his patience, especially at the beginning of my studies. I owe special thanks to Pia for all her selfless help in the administrative jungle. Thanks also to Assaf, David, Jeppe, Jules, Philipp, Rameez, Subodh and to all other staff and students who each contributed in their own way to a most enjoyable atmosphere at the homey institute we have.

Also outside of NBI, many have made my years here as joyful as they could be. I especially thank Tullinsgade with everyone connected for being a second home, Andita for her queetness, and Fynn for the many Tuesdays no matter the weekday.

I reserve the last paragraph for my parents and my sister who have been the biggest support throughout. I am fortunate to have you so close to me, despite the long distance, and grateful for you having taught me to seek something I am passionate about.

This thesis is based on the following publications.

*Footprints of Loop I on Cosmic Microwave Background Maps*
JCAP 1603 (2016) no.03, 023 [arXiv:1511.08207]
(with Hao Liu, P. Mertsch, and S. Sarkar)

*Towards understanding the Planck thermal dust models*
Phys.Rev. D95 (2017) no.10, 103517 [arXiv:1705.05530]
(with Hao Liu, and P. Naselsky)

*The Morphology of the Anomalous Microwave Emission in the Planck 2015 data release*
JCAP 1508 (2015) no.08, 029 [arXiv:1507.05171]
(with Hao Liu)

*Skewness and kurtosis as indicators of non-Gaussianity in galactic foreground maps*
JCAP 1511 (2015) no.11, 019 [arXiv:1509.03100]
(with A. Ben-David and A. D. Jackson)

*Statistical properties of polarized CMB foreground maps*
*submitted to MNRAS* [arXiv:1811.02470]
(with A. Gammelgaard Ravnebjerg, and Hao Liu)

*Methods for pixel domain correction of EB leakage*
*submitted to PRD* [arXiv:1811.04691]
(with J. Creswell, Hao Liu, and P. Naselsky)

CHAPTER 1

# Introduction

In this first chapter various aspects of the Cosmic Microwave Background (CMB) shall be discussed. I try to tie together historical events with a theoretical overview and observational challenges. I also put emphasis on presenting the methods in use in CMB data analysis today (Section 1.1). For the theory sections I relied mainly on Weinberg (2008), and in those concerned with observational and methodological aspects I cite on the go. Subsequently, I discuss the most prominent microwave emitting processes in our Galaxy, the so-called foregrounds for CMB experiments (Section 1.2). These, together, should set the stage for the main part of my thesis. I summarize this chapter in Section 1.3.

## 1.1 Cosmology through the eyes of the Cosmic Microwave Background

There are many ways to start the story of our Universe, many of which start in ancient Greece, Persia or Egypt, accounting for the astonishingly insightful thoughts the philosophers of the time had. Some others start with the beginning of detailed astronomical studies in the late middle ages. And again others begin with the transition of Cosmology as a subject of philosophical concern to a science in the definition maintained today. This last point, according to different researchers and historians, ranges from somewhere in between the first interpretation of Hubble's law as the expansion of the Universe to the first measurements of the Cosmic Microwave Background. As there is excellent literature already covering these early developments to saturation, I shall not try to compete with them and rather focus on the development of CMB science and the advances in understanding of our Universe induced by discoveries in measurements and theory of the CMB.

### 1.1.1 Thermodynamics and cosmic radiation

Following the first observations indicating the expansion of our Universe by Lemaître and Hubble, fundamental questions of the origin of elements could be viewed in a new setting. The most important conclusion of this expansion seemed to be that one now could trace the average energy content of the Universe. Just as for an adiabatically expanding box of dimensions $a^3$, the energy in the Universe follows the first law of thermodynamics[1]:

$$\partial_t E = -P\,\partial_t V \qquad \Rightarrow \qquad \partial_t(\rho a^3) = -P\,\partial_t a^3. \tag{1.1}$$

It turns out that the picture is simplified by the fact that the number density of baryons at all times was far smaller than the number density of photons, such that one can ignore the term $\mu dN$ usually present in Equation 1.1. Just as the energy density decreases with proceeding expansion, it of course increases in reverse time direction as the Universe contracts. In this context, it is reasonable to assume that matter and radiation were in thermal equilibrium at some point far enough in the past and due to the high temperature the matter was ionized. At this point the Universe certainly was dense enough so that the photons were unable to travel very far — the Universe was opaque to radiation. As obviously it is not opaque today, one can infer that at some point in the past a transition from high to almost negligible optical depth must have occurred. In practice, this transition is triggered by the recombination of the plasma and the decoupling of radiation and matter, permitting the photons to propagate unhindered through space. If the matter indeed was in equilibrium, the energy density, $\rho_\gamma$, of photons emitted at time $t_1$ and measured at time $t_0$, today, turns out to follow

$$\rho_\gamma(\nu, t_0)\,\mathrm{d}\nu = 8\pi h\nu^3\,\mathrm{d}\nu \int_{t_1}^{t_0} \left(e^{\frac{h\nu a(t_0)}{kT(t)a(t)}} - 1\right)^{-1} \frac{\mathrm{d}}{\mathrm{d}t}\mathcal{W}(t_0, t; \nu)\,\mathrm{d}\nu \quad , \tag{1.2}$$

where $h$ is Planck's constant, $k_B$ is the Boltzmann constant, $\nu$ is the frequency of the measured photon, $T(t)$ is the temperature of the matter at time $t$, and $\mathcal{W}$ is the probability to observe a photon of frequency $\nu$ today. Assuming a rapid drop in opacity at the time of recombination $t_R$, the term $\frac{\mathrm{d}}{\mathrm{d}t}\mathcal{W}(t_0, t; \nu)$ reduces to approximately $\delta(t - t_R)$ giving rise to a black-body distribution for the photons,

$$\rho_\gamma(\nu, t_0)\,\mathrm{d}\nu = 8\pi h\nu^3 \left(e^{\frac{h\nu a(t_0)}{kT(t_R)a(t_R)}} - 1\right)^{-1} \mathrm{d}\nu \quad , \tag{1.3}$$

[1] It is reassuring that within the framework of General Relativity this appears exactly in the energy conservation $\nabla_\mu T^{\mu 0} = 0$, where $T^{\mu\nu}$ is the energy-momentum-tensor for a perfect fluid in a FRW metric.

with a temperature of $T_0 \equiv T(t_0) \equiv T(t_R)a(t_R)/a(t_0)$.

The possible existence of cosmic black-body radiation left over from recombination was first noticed by George Gamow and collaborators who attempted to calculate nuclear abundances throughout time. Subsequently, several estimates of the temperature this black-body should follow today were performed, all falling in the range of a couple up to $\sim 10$ K, fairly accurate, yet it needed observation to be able to decide amongst these results.[2]

### 1.1.2 Observation I

The first measurement of the Cosmic Microwave background[3] occurred by accident by the two radio astronomers Penzias and Wilson (1965) who were occupied in constructing and calibrating high precision radio telescopes. Their detected "Excess Temperature" could immediately be explained by Dicke et al. (1965) who were already involved in an experiment ready to measure the just encountered background radiation. Roll's and Wilkinson's results were published soon after, supporting the previous measurements (Roll and Wilkinson, 1966). In the following, many more measurements were performed, from ground but also balloons and even rockets, attempting to palpate the entire black-body distribution. A coherent and most stringent experiment was finally launched on the COBE satellite (Mather et al., 1990a), resulting in the beautiful black-body spectrum shown in Figure 1.1 aside a less known but just as impressive measurement by the COBRA experiment (Gush and Halpern, 1992), published just a few months later. Due to the tight fit, these measurements immediately constrained all sorts of theories predicting significant energy release in form of photons at early times or energy injection into CMB photons at later times, which both would contribute to distortions of the black-body shape.

[2] I skipped a ton of considerations to be made here (as I will in the following subsections as well,). The treatments by Gamow et al. were unfortunately based on a wrong assumption, namely that all elements are formed by nucleosynthesis of a host of originally solely neutrons. Only later it became clear that through multiple interactions protons and neutrons must exist at equal ratios in the early Universe, ready to combine to deuterium and other light elements, while the production of heavy elements must wait until much later (Zel'dovich, 1965; Peebles, 1966). Only through this change of perspective it was possible to perform accurate calculations of the recombination history of our Universe, taking into account even details of atomic transition levels. For sake of brevity I must refer the reader to the literature on these exiting subjects (e.g. Mukhanov (2004b); Fields et al. (2014)).

[3] For a real first, though too early to be understood, see end of Section 1.2.3.

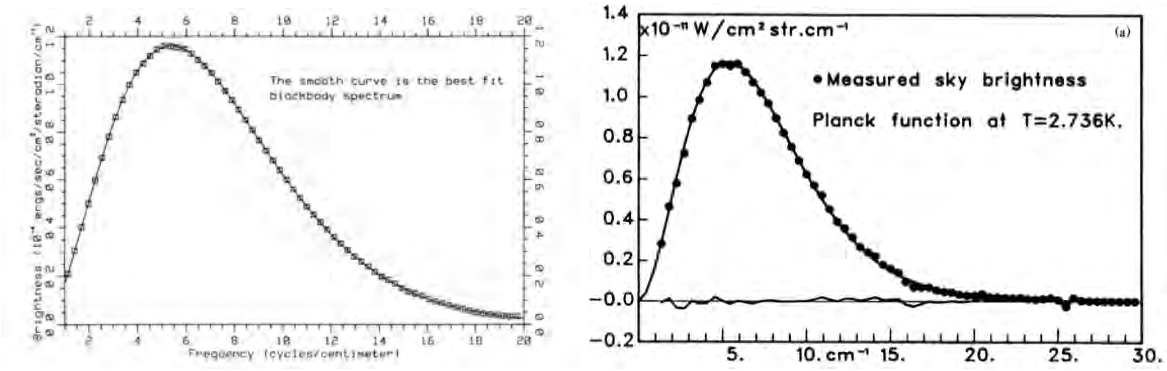


Figure 1.1 *Left panel:* Original measurement of the CMB blackbody by COBE FIRAS, resulting in a temperature of $2.735 \pm 0.06$ K. (From Mather et al. (1990b); later analysis with more data resulted in $T_0 = 2.72548 \pm 0.00057$ (Fixsen, 2009).) *Right panel:* Same measurement by the COBRA experiment, with a temperature of $2.736 \pm 0.017$ K. (From Gush et al. (1990).)

Another important question to ask aims at our relative velocity in respect to the cosmic black-body. As it seemed unlikely, that this relative velocity would be zero, quickly after the discovery of the CMB first experiments were performed to check for this additional support.

An observer boosted by the velocity $\vec{\beta}$ relative to the rest-frame of the CMB experiences the energy $E(\hat{p})$ of a photon with four-momentum $p$ as $E'(\hat{p}') = (\Lambda^{-1}\, p)^0 = \gamma E(1 + \vec{\beta} \cdot \hat{p})$, with $\gamma \equiv (1 - \beta^2)^{-1/2}$ as usual. The boosted observer finds the temperature $T$ of the CMB measured in its rest frame shifted to

$$T'(\hat{p}') = \frac{T(\hat{p})}{\gamma(1 - \vec{\beta}\,\hat{p}')} \simeq \frac{T(\hat{p})}{\gamma}\left[1 + \vec{\beta}\,\hat{p}' + \mathcal{O}\left((\vec{\beta}\,\hat{p}')^2\right)\right] \tag{1.4}$$

For the observed temperature fluctuations $\delta T'(\hat{p}')$, to linear order in $\beta$, this means

$$\delta T'(\hat{p}') = T_0\,\vec{\beta}\,\hat{p}' + \delta T(\hat{p})\left(1 + \vec{\beta}\hat{p}'\right), \tag{1.5}$$

where the CMB rest-frame temperature $T(\hat{p})$ was split up into the CMB monopole $T_0$ and the position dependent fluctuations $\delta T(\hat{p})$. While the first term describes variation of the CMB temperature with angle $\theta \equiv \arccos(\vec{\beta}\,\hat{p}')$, the second term describes effects of our relative velocity in respect to the CMB on the temperature fluctuations. One of these is the so called aberration effect, which arises as soon as $\hat{p}$ is transformed into the observers coordinates; it describes a decrease of structure size in the direction of our movement towards and an enhancement in the opposite direction of our movement towards the CMB. The second effect, is the so called dipole modulation, responsible for an increase in fluctuations in the direction of our movement

towards the CMB. There are more effects, for instance the Doppler quadrupole, which occurs at quadratic order in $\beta$, or effects of the dipole on all other multipoles. However, these effects are quite small.

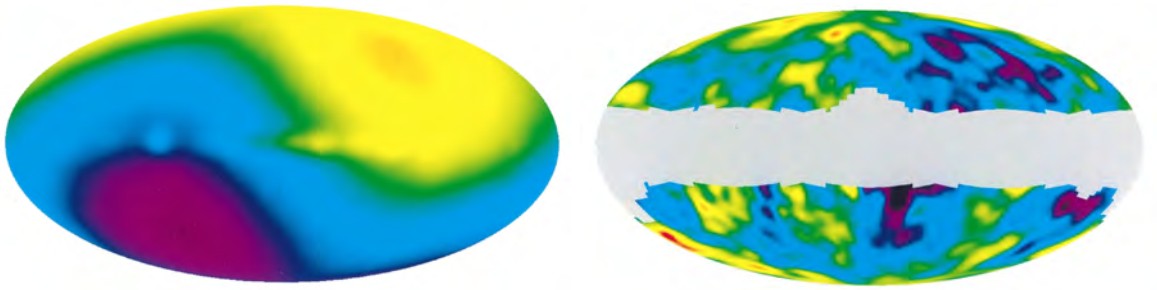

Figure 1.2 *Left panel:* The 4 yr 53 GHz DMR map, including the dipole. *Right panel*: The 4 yr DMR map, excluding the dipole, using data from 31, 53, and 90 GHz with modeled Galactic emission removed, and the Galactic custom cut applied. (From Bennett et al. (1996).) While no scales are provided, the left map's scale approximately corresponds to $-10^{-3}\,\mathrm{K} \lesssim T \lesssim 10^{-3}\,\mathrm{K}$, the right map's approximately to $-10^{-4}\,\mathrm{K} \lesssim T \lesssim 10^{-4}\,\mathrm{K}$.

The left panel of Figure 1.2 shows the Doppler dipole measured by COBE. The measurements are still consistent with the *Planck* Collaboration's update on this matter, which give a direction of $(l, b) = (264°, 48°)$ in Galactic coordinates and a velocity of $384\,\mathrm{km\,s^{-1}}$ for the solar system (however, with $\sim 20$ and 30% uncertainties of statistical and systematic nature, respectively) (Planck 2013 results. XXVII). After subtracting the dipole, the COBE measurements revealed hints of a substructure present in the CMB or in other words, slight deviations from the measured temperature in some regions of the sky, see right panel of Figure 1.2. It will need a step back to look at the accompanying theory first in order to consider whether to believe those ripples or mark them down as errors of the measurement.

### 1.1.3 Theoretical description and motivation

The expanding-box-universe from section 1.1.1 is mathematically described by a metric in the framework of General Relativity[4]. In a flat universe, assuming isotropy and homogeneity leads to the Friedmann-Lemaitre-Robertson-Walker (FLRW) metric $g_{\mu\nu}$, for which the Einstein

[4]As promised, I do not provide a summary on General Relativity. Acquaintance with the equations and their treatment is assumed. However, no involved calculations are repeated here. Rather, this section outlines a strategy towards the calculation of the perturbations in the CMB.

equations,

$$R_{\mu\nu} - \frac{1}{2}Rg_{\mu\nu} = -8\pi G T_{\mu\nu} \qquad \text{with} \qquad g_{\mu\nu} = \mathrm{diag}(-1, a^2(t), a^2(t), a^2(t)) \tag{1.6}$$

give the Friedmann equation, which governs the expansion of the Universe, and energy conservation, inherent in the definition of the theory itself[5].

$$H(t)^2 \equiv \frac{\dot{a}^2(t)}{a^2(t)} = \frac{8\pi G}{3}\rho\, a^2(t) \qquad\qquad \dot{\rho} = -3H(t)(\rho + P) \tag{1.7}$$

Above, the indices $\mu$ and $\nu$ run from 0 to 3, $R_{\mu\nu}$ is the Ricci tensor, $R = g^{\mu\nu}R_{\mu\nu}$ is the Ricci scalar, $G$ is Newton's gravitational constant, $T_{\mu\nu} = \mathrm{diag}(\rho, a^2(t)P, a^2(t)P, a^2(t)P)$ is the energy-momentum tensor, here chosen for a perfect fluid, $a(t)$ is the cosmological scale factor, known from above's expanding box's dimensions, $H(t)$ is the Hubble parameter as defined in the equation[6], and a *dot* denotes a derivative with respect to time $t$.

**Metric perturbations** The aim will now be to compute the small deviations $\delta T$ from the mean temperature value $T_0$ in the CMB[7] (structure must have clustered at some point). A seed for this clustering can be planted by perturbing the metric $g_{\mu\nu}$ by a small amount $h_{\mu\nu}$ as

$$g_{\mu\nu} = \overline{g}_{\mu\nu} + h_{\mu\nu}, \tag{1.8}$$

where now $\overline{g}_{\mu\nu}$ is the (unperturbed) FLRW metric from above. This change makes the Einstein equations a great deal more complicated. In addition, the energy density $\rho$ and the pressure $P$ are perturbed to accommodate a perturbation in the energy-momentum tensor. The resulting mess (which for obvious reasons I am not showing), is considerably ordered if one splits up the perturbations in scalar ($A$, $B$, $F$, and $E$), vector ($C_i$ and $G_i$), and tensor modes ($D_{ij}$) by use of Helmholtz' theorem[8]:

$$h_{00} = -E \quad , \quad h_{i0} = a\left[\partial_i F + G_i\right] \quad , \quad h_{ij} = a^2\left[A\delta_{ij} + \partial_i\partial_j B + \partial_i C_j + \partial_j C_i + D_{ij}\right] \tag{1.9}$$

where $i$ and $j$ run from 1 to 3. Also the perturbation to the energy-momentum tensor $\delta T_{\mu\nu}$ is decomposed in such manner (under additional consideration of dissipative corrections), though the principle should be clear. Before writing out the essential equations from perturbing the

[5] and known from section 1.1.1.

[6] The explicit time dependence of $a$ and $H$ will be dropped from now on.

[7] I do not choose a different notation for temperature than I do for the trace of the energy momentum tensor, but it should be clear from the context.

[8] Here, Helmholtz theorem requires the conditions $\partial_i C_i = \partial_i G_i = 0$, $\partial_i D_{ij} = 0$, and $D_{ii} = 0$.

Einstein equations — and I will do so only for scalar perturbations, to save time — one first picks a gauge in order to simplify things even more. In the *synchronous gauge* the metric perturbation reduces to

$$h_{00} = 0\,, \quad h_{i0} = 0\,, \quad h_{ij} = a^2(A\delta_{ij} + \partial_i\partial_j B) \tag{1.10}$$

Now the perturbed Einstein equations and the equations for energy and momentum conservation, for scalar modes, can be summarized in the three equations

$$-4\pi G a^2\left(\delta\rho + 3\delta P + \nabla^2\pi^S\right) = \partial_t(a^2\psi) \tag{1.11}$$

$$\delta P + \nabla^2\pi^S + \partial_t((\overline{\rho} + \overline{P})\delta u) + 3H(\overline{\rho} + \overline{P})\delta u = 0 \tag{1.12}$$

$$\delta\dot{\rho} + 3H(\delta\rho + \delta P) + \nabla^2\left(a^{-2}(\overline{\rho} + \overline{P})\delta u + H\pi^S\right) + (\overline{\rho} + \overline{P})\psi = 0 \tag{1.13}$$

where $\delta u$ and $\pi^S$ describe velocity perturbations and anisotropic inertia, respectively, and come from the perturbed energy-momentum tensor, and $\psi$ was defined to incorporate both scalar metric perturbations $A$ and $B$ as

$$\psi \equiv \frac{1}{2}(3\dot{A} + \nabla^2\dot{B}) = \partial_t\left(\frac{h_{ii}}{2a^2}\right). \tag{1.14}$$

**Boltzmann equations** Equations 1.11–1.13 describe how small perturbations to quantities like the energy density $\rho$ evolve. So far, the energy density does not know yet, which particles to describe in specific. If one starts the calculation at a high enough temperature $T \gtrsim 10^6\,\mathrm{K}$ such that thermal equilibrium of the matter can be assumed, but at a low enough temperature $T \lesssim 10^9\,\mathrm{K}$, such that other elementary particles are not produced, like e.g. muons via electron-positron annihilation, the species present in the Universe of that time were photons, cold dark matter (CDM), neutrinos and baryons (i.e. electrons, ions, neutral atoms). In this regime, the different components can be described hydrodynamically leading to many simplifications in the equations. However, since for the CMB especially the time of recombination, where temperatures are of order $T \sim 10^3$ K, is of interest, a kinematic approach must be chosen, which is done by formulating the corresponding Boltzmann equations in phase space. These are generally hard to follow analytically[9], which is why I only skim over the essential steps to provide a rough picture of what is happening.

[9] See, however, a brute-force approach by Mukhanov (2004a), who was able provide physical understanding despite all difficulties (at the cost of some approximations).

The Boltzmann equation generally is of the form

$$\frac{\mathrm{d}n(x^i, p_i, t)}{\mathrm{d}t} = C[n] \tag{1.15}$$

where $x^i$ and $p_i$ are the three-position and three-momentum vectors, and where the right-hand side describes all possible collisions among the particles of number density $n$ and of course is zero for collisionless considerations. In regard to the collisions the photons undergo, one finds two contributing terms: One for the photons being scattered *into* a phase space element, and one for those being scattered *out*. Precisely these fluctuations are of interest. For this purpose one lets $n \to \overline{n} + \delta n$ and sets up the Boltzmann equation for the perturbed number density, resulting in (save a ton of calculations):

$$\partial_t \delta n^{ij} + \frac{\hat{p}_k}{a}\partial_k \delta n^{ij} + 2H\delta n^{ij} - \frac{1}{4a^2} p\overline{n}'(p)\hat{p}_k\hat{p}_l\partial_t\left(a^{-2}h_{kl}\right)\left(\delta_{ij} - \hat{p}_i\hat{p}_j\right) = C^{ij}[n], \tag{1.16}$$

where the number density and hence also the collision term were promoted to a matrix, as the different polarization states for photons are not independent if scattering is taken into account, and *hats* denote normalized quantities. In the fourth term on the left-hand side one finds the metric perturbation $h_{kl}$ which was already expressed in terms of the scalar perturbations $A$ and $B$, Equation 1.10.

**Temperature perturbations** Conventionally a temperature perturbation of the baryonic plasma is defined over the number density and its perturbations as

$$\Delta_T(x^i, p_i, t) = \int_0^\infty \frac{p^3\mathrm{d}p}{(2\pi)^3}\delta n(x^i, p_i, t) \Bigg/ \int_0^\infty \frac{p^3\mathrm{d}p}{(2\pi)^3}\overline{n}(x^i, p_i, t) \tag{1.17}$$

The Boltzmann equations for $\delta n$ will therefore immediately imply a set of equations for $\Delta_T$. Furthermore, making use of the translational invariance, one can Fourier transform the temperature perturbation into $\Delta_T(q, \mu, t)$, where $\mu \equiv \hat{q}^i\hat{p}_i$, and in addition expand it into Legendre polynomials. The temperature perturbation then reads

$$\Delta_{T,\ell}(q, t) = \frac{2\ell + 1}{2}\int_{-1}^{1}\Delta_T(q, \mu, t)P_\ell(\mu)\,\mathrm{d}\mu \tag{1.18}$$

The coupled Boltzmann equations for temperature and polarization[10] (for scalar perturba-

[10] I have not discussed how the polarization perturbations are defined. In general both temperature and polarization can be consistently defined in an intensity matrix, which can just as well be plugged into the Boltzmann equation. I show both equations of motion here because they are coupled — scattering of photons can produce a net polarization.

tions) now can be formulated out. The only term not touched yet is the collision term $C^{ij}[n]$, though in addition to what was remarked above, not any more should be said here other than that all collisions are proportional to the collision rate $\omega_c(t) = \sigma_T n_e(t)$ of photons with electrons, where $\sigma_T$ is the Thomson scattering cross section and $n_e$ is the free electron number density. Making use of Bonnet's recursion formula for the Legendre polynomials leads to the Boltzmann hierarchy

$$\dot{\Delta}_{T,\ell} + \frac{q}{a(2\ell+1)}\left((\ell+1)\Delta_{T,\ell+1} - \ell\Delta_{T,\ell-1}\right) = -2\dot{A}_q\delta_{\ell 0} + 2q^2\dot{B}_q\left(\frac{\delta_{\ell 0}}{3} - \frac{2\delta_{\ell 2}}{15}\right) \\ -\omega_c\Delta_{T,\ell} + \omega_c\Delta_{T,0}\delta_{\ell 0} + \frac{1}{10}\omega_c\Pi\delta_{\ell 2} - \frac{4q}{3a}\omega_c\delta u_q\delta_{\ell 1} \tag{1.19}$$

$$\dot{\Delta}_{P,\ell} + \frac{q}{a(2\ell+1)}\left((\ell+1)\Delta_{P,\ell+1} - \ell\Delta_{P,\ell-1}\right) = -\omega_c\Delta_{P,\ell} + \frac{1}{2}\omega_c\Pi\left(\delta_{\ell 0} + \frac{\delta_{\ell 2}}{5}\right) \quad , \tag{1.20}$$

where the so called source function $\Pi \equiv \Delta_{P,0} + \Delta_{T,2} + \Delta_{P,2}$ and for (a little more) clarity the arguments $(q,t)$ of the perturbations were dropped. To suit the temperature perturbation, the perturbations $A$, $B$ and $\delta u$ were denoted as Fourier amplitudes defined via

$$A(\vec{x},t) = \sum_n \int \mathrm{d}^3q\, \alpha_n(\vec{q}) A_{nq}(t) e^{i\vec{q}\vec{x}}\,, \qquad B \text{ and } \delta u \text{ equivalently.} \tag{1.21}$$

The stochastic variables $\alpha_n(\vec{q})$ thereby favor certain modes according to their underlying spectral function $\mathcal{P}_{nm}(q)$ defined via

$$\langle \alpha_n(\vec{q})\alpha_m^*(\vec{q}')\rangle = \mathcal{P}_{mn}(q)\delta^3(\vec{q}-\vec{q}'). \tag{1.22}$$

It is this spectral function $\mathcal{P}$ which governs the initial conditions for the perturbations $A$, $B$, etc. Hence, finding the perturbations from observation is not enough to fix the cosmological theory; one must also find a theory which predicts the origin of these very fluctuations by a prediction of $\mathcal{P}$. Taking into account the evolution of the scalar perturbations from Equations 1.11–1.13, Equations 1.19 and 1.20 can be solved for $\Delta_{T,\ell}(q,t)$.

Note that, I only considered scalar perturbations here. Vector perturbations are commonly ignored as they decay quite quickly and therefore play a completely negligible role if they are not sourced by some specific process. The temperature perturbations, for low multipoles $\ell$, obtain a contribution from the tensor modes as well, which should not be forgotten in a complete treatment of the subject. However, as tensor modes evolve independently from the scalar modes, their respective power spectra simply add up, so that our above treatment must only be extended, not altered.

### 1.1.4 Observables

Finally, it is time to take a look at the sky and translate the content of the previous section to quantities one can observe. For this purpose, spherical harmonic functions come in handy, which can decompose a signal $s(\hat{n})$ on the celestial sphere into contributions from different scales, $\ell$:

$$s(\hat{n}) = \sum_{\ell=0}^{\infty} \sum_{m=-\ell}^{\ell} a_{\ell m} Y_{\ell m}(\hat{n}), \tag{1.23}$$

$$\text{or} \quad a_{\ell m} = \int \mathrm{d}\hat{n}\, s(\hat{n}) Y^*_{\ell m}(\hat{n}). \tag{1.24}$$

By already having introduced a Legendre decomposition in the previous section only one last step is needed to find the desired relation: For a particular choice of $\alpha(\vec{q})$, the spherical harmonics for the observed CMB sky at time $t_0$ today, read

$$a_{T,\ell m} = \pi T_0 i^\ell \int \mathrm{d}^3 q\, Y^*_{\ell m}(\hat{q}) \alpha(\vec{q}) \Delta_{T,\ell}(q, t_0), \tag{1.25}$$

and of course, analogous to Equation 1.24,

$$\Delta T_{CMB}(\hat{n}) = \sum_{\ell=2}^{\infty} \sum_{m=-\ell}^{\ell} a_{T,\ell m} Y_{\ell m}(\hat{n}), \tag{1.26}$$

$$\text{or} \quad a_{T,\ell m} = \int \mathrm{d}\hat{n}\, \Delta T(\hat{n}) Y^*_{\ell m}(\hat{n}). \tag{1.27}$$

Note that, here the modes $\ell = 0$ and $\ell = 1$ (the monopole and dipole) have not been included in the sum: The temperature *fluctuations* by definition ignore the full-sky average temperature, and since isotropy is assumed throughout the standard cosmological history, the only contributor of a dipole term can be a non-cosmological motion of the observer themself (as seen in section 1.1.2). And since the signal on the sky is a real quantity, $a_{\ell m} = a^*_{\ell -m}$. A further property of our standard cosmology is that the fluctuations are considered *statistically* isotropic and homogeneous. Therefore, for a given scale $\ell_*$ the spherical harmonic coefficients $a_{\ell_* m}$ of particular modes $m$ should not be meaningful quantities — only the "total power" per scale counts. For this purpose the temperature fluctuations' expected two-point function is described by the corresponding power spectrum

$$\langle a_{T,\ell m} a^*_{T,\ell' m'} \rangle = \delta_{\ell \ell'} \delta_{m m'} C^{TT}_\ell. \tag{1.28}$$

In practice, however, only one sample of the CMB can be recorded, and the average over $a_{\ell m}$s therefore cannot be evaluated. One thereto defines an estimate of the power spectrum as

$$\widehat{C}_\ell^{TT} = \frac{1}{2\ell+1}\sum_{m=-\ell}^{\ell}|a_{T,\ell m}|^2, \tag{1.29}$$

which must carry sampling uncertainties. The quadratically increasing number of terms in the sum for increasing $\ell$ luckily saves these from being $\mathcal{O}(1)$ and one finds

$$\left\langle\left(\frac{C_\ell - \widehat{C}_\ell}{C_\ell}\right)^2\right\rangle = \frac{2}{2\ell+1}. \tag{1.30}$$

These tools at hand, sets the stage for analysis of the CMB's temperature patterns.

**Polarization** Of course, also the polarization perturbations lead to a specific pattern on the sky. Due to the two helicity states of polarization, the signal $a_{P,\ell m}$ is expressed in terms of a linear combination of the two Stokes parameters $Q$ and $U$, in order to match the observed signal in the two polarization directions. $Q$ and $U$ are two of the, in total, four Stokes parameters (also including the intensity $I$ and the circular polarization parameter $V$) which completely describe polarization angle and amplitude of incoming light.[11] They depend on the choice of a local coordinate system and transform with rotation around the line of sight as

$$\begin{pmatrix} Q(\hat{n}) \\ U(\hat{n}) \end{pmatrix}' = \begin{pmatrix} \cos 2\psi & \sin 2\psi \\ -\sin 2\psi & \cos 2\psi \end{pmatrix} \begin{pmatrix} Q(\hat{n}) \\ U(\hat{n}) \end{pmatrix}. \tag{1.31}$$

The polarization intensity, however, is defined to be rotationally invariant:

$$P(\hat{n}) \equiv \sqrt{Q^2(\hat{n}) + U^2(\hat{n})}, \tag{1.32}$$

and the polarization fraction $p(\hat{n}) \equiv I(\hat{n})/P(\hat{n})$, since the relation $I^2(\hat{n}) \geq P^2(\hat{n})$ reaches equality in the case of 100% polarized light ($p = 1$). Lastly, the polarization angle (the direction of the electric field vector given the chosen reference) computes to

$$\phi(\hat{n}) = 0.5\tan^{-1}\frac{\mathrm{U}(\hat{\mathrm{n}})}{\mathrm{Q}(\hat{\mathrm{n}})}. \tag{1.33}$$

[11] The CMB is not expected to be circularly polarized, and therefore $V$ will be ignored in the following.

One may also construct a spin-2 quantity, equivalent to Equation 1.31:

$$ {}_{\pm2}X(\hat{n}) = Q(\hat{n}) \pm iU(\hat{n}), \tag{1.34} $$

which transforms as ${}_{\pm2}X'(\hat{n}) = e^{\mp 2i\psi}\,{}_{\pm2}X(\hat{n})$. With the help of spin-weighted spherical harmonics, the corresponding harmonic coefficients read

$$ a_{\pm2,\ell m} = \int \mathrm{d}\hat{n}\, {}_{\pm2}X(\hat{n})\, {}_{\pm2}Y^*_{\ell m}(\hat{n}). \tag{1.35} $$

Instead of this local measure of polarization, conventionally $E$- and $B$-modes are defined (Zaldarriaga and Seljak, 1997; Zaldarriaga, 1998), inspired by the $E$- and $B$-field decomposition in electrodynamics, where the (conservative) $E$ field is curl-free and therefore can be expressed as a gradient of a scalar field, and the $B$-mode is divergence-free and therefore can be expressed as a curl of a vector field (again a Helmholtz decomposition). From this it is immediately clear that $B$-modes in the CMB cannot be generated by scalar perturbations[12], only via vector or tensor perturbations. On the other hand, $E$-modes can be generated by all kinds of perturbations. This supports the choice of this additional decomposition and proves itself very helpful in the search for tensor perturbations, potentially produced in a theory of primordial fluctuations.[13]

The $E$- and $B$-modes are defined as

$$ \begin{aligned} a_{E,\ell m} &\equiv -(a_{+2,\ell m} + a_{-2,\ell m})/2 \\ a_{B,\ell m} &\equiv i(a_{+2,\ell m} - a_{-2,\ell m})/2. \end{aligned} \tag{1.36} $$

From these, it is possible to construct power spectra equivalent to the one seen for temperature perturbations

$$ \widehat{C}_\ell^{EE} = \frac{1}{2\ell+1} \sum_{m=-\ell}^{\ell} |a_{E,\ell m}|^2 \tag{1.37} $$

$$ \widehat{C}_\ell^{BB} = \frac{1}{2\ell+1} \sum_{m=-\ell}^{\ell} |a_{B,\ell m}|^2 \tag{1.38} $$

$$ \widehat{C}_\ell^{XY} = \frac{1}{2\ell+1} \sum_{m=-\ell}^{\ell} a_{X,\ell m} a_{Y,\ell m}, \tag{1.39} $$

where in the last line the cross-spectrum between two modes (from $T$, $E$, and $B$) is defined.

[12] At least not directly — gravitational lensing is one effect which can distort $E$-modes so much that they end up becoming $B$-modes. Although this is a late-time effect.

[13] It should said already now, that our view on the CMB is corrupted by Galactic foregrounds. The foregrounds' polarized emission of course is not constrained by these arguments and can shine in both $E$- and $B$-modes. A misidentification of astrophysical with primordial $B$-modes must therefore inhibited at all events.

Maps of the $E$- and $B$-modes can be reconstructed as

$$\begin{aligned} E(\mathbf{n}) &= \sum a_{E,\ell m}\, Y_{\ell m}(\mathbf{n}), \\ B(\mathbf{n}) &= \sum a_{B,\ell m}\, Y_{\ell m}(\mathbf{n}). \end{aligned} \tag{1.40}$$

Recently, some effort has gone into the construction of tools which combine both the Stokes $Q/U$ and the $E/B$ parameters (Liu et al., 2018; Rotti and Huffenberger, 2018). Their idea is to separate $Q$ and $U$ maps into those parts which will contribute into maps of $E$ and $B$ after transforming. I review this separation in Section 5.2.1.

**Inferring Cosmology from the CMB** Unfortunately, solving the Boltzmann equations gives little insight into the physical processes. Still, it was found which factors play a role in forming the ripples observed in the CMB as early as with the COBE satellite: Baryonic matter, dark matter, radiation (and neutrinos) contribute to the energy density and pressure terms in Equations 1.11–1.13, as does the scale factor in the metric as well as the perturbations to the metric, Equation 1.9. The metric perturbations' stochastic parameters, conduct the initial conditions from which to start the calculations. And finally, all interactions are collected and evolved with time in the Boltzmann hierarchy 1.16, by construction including photon decoupling.[14] This leads to five of the six independent cosmological parameters of the standard model of cosmology, namely the (physical) baryon density parameter $\Omega_b h^2$, the (physical) cold dark matter density parameter $\Omega_c h^2$, the age of the universre today $t_0$, and finally two parameters determining the initial conditions for the metric perturbations $n_S$ and $A_S$, the spectral index and the amplitude of scalar perturbations. There is a sixth parameter to be included in this list, the optical depth at reionization $\tau$. Reionization describes an event in the late Universe, when the first population of hydrogen stars ionized in part the neutral medium via their UV radiation. Luckily, the density of matter / the optical depth at that time ($z \sim 6$) was low enough that not all CMB photons interacted with the free electrons, yet it was enough to "wash out" the fluctuations in the power spectrum to some degree. These six parameters (more can subsequently be inferred) can be extracted from a measurement of the CMB's power spectrum in the setting of the standard model of cosmology.

[14] To precisely include the processes at recombination, atomic processes have to be included by hand. The formation of light elements has been mentioned briefly in earlier chapters. For a quantitative review I again refer the reader to the literature, e.g. Sunyaev and Chluba (2008).

### 1.1.5 Unveiling the CMB

There are a number direct influences on the CMB photons at different times after last scattering, some of which have been mentioned in previous sections. Properly identifying these effects in principle is not a problem and has been tested extensively in simulations. However, in addition to *background* photons, CMB surveys also record microwave radiation from other sources. Unfortunately[15], living within a galactic disk means the presence of an overwhelming amount of radiation from our Galaxy. In the context of CMB studies, the different Galactic emission phenomena are collectively referred to as *foregrounds* as opposed to the background radiation. This section deals with methods which have been developed to overcome the influence of foreground emission, and to obtain a clear view on the CMB. Only then reasonable parameter estimation, as in the previous chapter, can begin.

Figure 1.3 shows average spectra of foreground emission in comparison to the level of emission expected from the CMB; the shown amplitudes of the spectra are characteristic of the emission at high Galactic latitudes. Beside this, I show a sky map recorded by the *Planck* satellite at 70 GHz — a frequency, where the CMB anisotropy dominates over the foregrounds, and can be seen as the small ripples at away from the Galactic plane and its emission, as can be anticipated from the left panel.

There are two strategies of how to obtain a trustworthy cosmological signal: 1. Observe the sky at different frequencies. In the right units[16], the contribution of foregrounds will change, and under certain assumptions, one can subtract this contribution from the signal common to all observations. The resulting image is a map of the CMB which readily can be transformed into its power spectrum. 2. Observe the sky at a frequency, where the CMB anisotropy is more pronounced than the foregrounds' emission. Mask out parts of the sky, transform the rest into a power spectrum, and remove possible residual contamination, again, under certain assumptions.

The *Planck* collaboration does both — and combines their results by using "1." for large scales, and "2." for small scales. I outline both methods here, with emphasis on the former, as my thesis will be concerned with those methods and their products, primarily.

There are two classes of foreground cleaning algorithms. Those which make specific assumptions on the foregrounds' spectral behavior (informed methods), and those which do not (blind

[15] For observation, not for us as potential observers.

[16] At this point it should be mentioned that the units, with which are conveniently worked in CMB science, are those of CMB thermodynamic temperature. They have the advantage that the CMB anisotropy spectrum is frequency independent, while (hopefully) all other signals can be detected by their variation with frequency. I define these units in Appendix A.1.

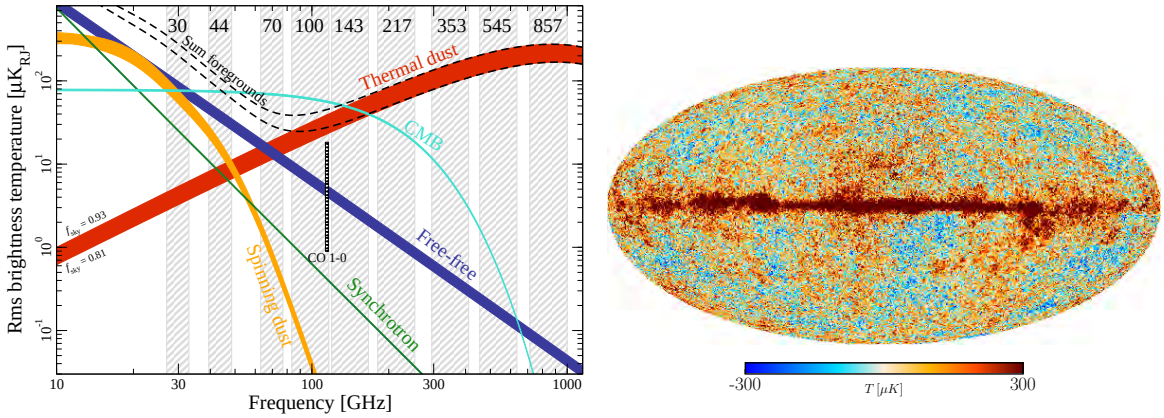


Figure 1.3 *Left panel:* Spectra of Galactic foregrounds and CMB anisotropy, with amplitudes characteristic for high Galactic latitudes. (From Planck 2018 results. I.) *Right panel:* The *Planck* LFI 70 GHz map as of PR3.

methods). While the former is able to not only remove, but also to disentangle the contributions from different foregrounds, the latter cannot and simply results in an estimate of a CMB map. As I will show in section 4.1, also the so-called blind foreground removal algorithms make assumptions on the foregrounds' behavior — the two seemingly different approaches therefore might share inherent traits.

**Cleaning sky maps — Foreground removal algorithms** A commonly used framework to understand blind foreground subtraction algorithms is that of Internal Linear Combination, or ILC, which has been introduced to CMB science by the *WMAP* collaboration (Bennett et al., 2003). Sky maps of different frequency are linearly combined with the aim to arrive at a map of the CMB anisotropy. More sophisticated algorithms are in use today, see e.g. Planck 2015 results. IX, albeit they result in CMB products consistent with an ILC solution. In this section I shall briefly review essential elements and assumptions of the ILC method, as a representative of such blind foreground removal techniques.

The method goes as follows (Eriksen et al., 2004). Consider a signal, $s_\nu(\hat{n})$, on the sky consisting of only CMB anisotropy, $\Delta T(p)$, and a term describing the foreground, $f_\nu(\hat{n})$, in each sky direction $\hat{n}$, measured at frequency $\nu$, and in units where the CMB's contribution is frequency independent. A weighted sum over all frequency maps reads

$$\mathcal{S}(\hat{n}) = \sum_\nu w_\nu S_\nu(\hat{n}) = \Delta T(\hat{n}) + \sum_\nu w_\nu F_\nu(\hat{n}), \tag{1.41}$$

for which one assumes

$$\sum_{\nu} w_{\nu} = 1 \tag{1.42}$$

and where for later convenience I defined

$$\begin{aligned} S_{\nu}(\hat{n}) &\equiv s_{\nu}(\hat{n}) - \langle s_{\nu} \rangle_{\Omega}, \\ \Delta T(\hat{n}) &\equiv T(\hat{n}) - \langle T \rangle_{\Omega}, \\ F_{\nu}(\hat{n}) &\equiv f_{\nu}(\hat{n}) - \langle f_{\nu} \rangle_{\Omega}, \end{aligned}$$

and the angular brackets $\langle ... \rangle_{\Omega}$ denote the average over the entire region $\hat{n} \in \Omega$, the region of the sky under consideration. The intention of the ILC method is to fix the weights $w_{\nu}$ such that the last term in Equation (1.41) vanishes. This is not generally possible, which is conventionally solved by requiring the variance of $\mathcal{S}$ to be minimal. The variance of Equation (1.41) then reads

$$\langle \mathcal{S}^2 \rangle_{\Omega} = \langle \Delta T^2 \rangle_{\Omega} + 2 \sum_{\nu} \langle \Delta T \, F_{\nu} \rangle_{\Omega} \, w_{\nu} + \sum_{\nu\mu} \langle F_{\nu} \, F_{\mu} \rangle_{\Omega} \, w_{\nu} w_{\mu}. \tag{1.43}$$

The first term in Equation (1.43) corresponds to the variance of the CMB signal, the second describes the chance correlations between the CMB and the total foreground in the frequency band $\nu$, and the last term depends on the cross-correlation matrix of the foregrounds at frequencies $\nu$ and $\mu$. All these quantities are evaluated in the entire region $\Omega$.

Seeking for the minimum of Equation 1.43 under consideration of the constraint 1.42 by, for example, the use of Lagrange multipliers one finds:

$$w_{\mu} = \frac{\sum_{\mu} \widehat{C}^{-1}_{\nu\mu}}{\sum_{\mu} \sum_{\lambda} \widehat{C}^{-1}_{jk}}, \tag{1.44}$$

where the signal covariance matrix was defined as

$$\widehat{C}_{\nu\mu} = \langle S_{\nu}(\hat{n}) S_{\mu}(\hat{n}) \rangle_{\Omega}. \tag{1.45}$$

Applying eq. 1.42 to eq. 1.41 yields the estimator for the CMB map. As one can see, the weights $w_{\nu}$ are independent of $\hat{n}$. The ILC therefore inherently assumes the sky to be composed of templates, which each are scaled through frequency with a constant factor. This assumption will be treated in more detail in Section 4.1

In practice, the pure ILC method produces relatively noisy results compared to exten-

sions/modifications, of which there are many (Harmonic ILC (HILC; Kim et al. (2008)), Needlet ILC (NILC; Basak and Delabrouille (2012)), Scale-discretized directional wavelet ILC (SILC; Rogers et al. (2016)), ...). The *Planck* Collaboration therefore (mostly) refrains from using an ILC in its simplest form.

Also the SMICA method (Spectral Matching Independent Component Analysis; Delabrouille et al. (2003)), the favorite of the *Planck* Collaboration (it leaves the lowest residuals), is based on a linear combination of the signals observed at different frequencies. It works in the harmonic domain; there, if $\Omega$ is taken to be the full sky, Equation 1.41 reads

$$\mathcal{S}(\ell, m) = \sum_{\nu} w_{\nu}(\ell) S_{\nu}(\ell, m), \tag{1.46}$$

and again the weights are calculated to

$$w_{\nu}(\ell) = \frac{\sum_{\mu} C^{-1}_{\nu\mu}(\ell)}{\sum_{\mu}\sum_{\lambda} C^{-1}_{\mu\lambda}(\ell)}. \tag{1.47}$$

The great difference between a harmonic version of the ILC approach (as was originally introduced by Tegmark and Efstathiou (1996)) and the SMICA method is that the covariance matrix $C_{\nu\mu}(\ell)$ is the *expected* cross power spectrum between, not, $\widehat{C}_{\nu\mu}(\ell)$, the estimated one:

$$C_{\nu\mu}(\ell) \equiv \langle S_{\nu}(\ell m) S^{*}_{\mu}(\ell, m)\rangle \neq \frac{1}{2\ell+1}\sum_{m} S_{\nu}(\ell, m) S^{*}_{\mu}(\ell, m). \tag{1.48}$$

Under various, flexible assumptions about the CMB term, $\Delta T$, and the foreground components, $F$, the SMICA method attempts to find the *best* estimate of $C_{\nu\mu}(\ell)$, given the data $S_{\nu}(\ell, m)$. For a measure of "best" it relies of a Gaussian likelihood, where the model of $C_{\nu\mu}(\ell)$ is determined as follows. The specific assumptions made by (Planck 2015 results. IX), include independence of $\Delta T$ and $F$,[17] and $\ell$-independent foreground spectra, which fix the model of $C(\ell)$. If $F$ only contains one foreground component, the model reads

$$C_{\nu\mu}(\ell) = C^{TT}_{\nu\mu}(\ell) + C^{FF}_{\nu\mu}(\ell) = \tag{1.49}$$

$$= C^{TT}_{\nu\mu}(\ell) + a_{\nu} a_{\mu} C^{AA}(\ell), \tag{1.50}$$

[17] Of course the *Planck* collaboration also includes detector noise, not listed here, which also is assumed to be independent of $\Delta T$ and $F$, and to further have no correlation across frequency bands.

where I defined

$$F_\nu(\ell, m) = a_\nu A(\ell, m), \tag{1.51}$$

and $C^{AA}(\ell) = \langle A(\ell, m) A^*(\ell, m) \rangle$ accordingly. ($G > 1$ foreground components would be added linearly in $F$, promoting $C^{AA}(\ell)$ to a matrix of shape $G \times G$ and also adding an extra dimension $G$ to the scaling constants $a_\nu$.) One can see that the foreground template $A(\ell, m)$ is scaled through frequencies $\nu$ without any possibility for variation in the spectral properties — similar to the assumptions in the ILC method.[18] From the determined $C_{\nu\mu}(\ell)$ the harmonic weights in Equation 1.47 can be calculated. Eventually, this leads to an estimate of the CMB, just as before. In general, all foreground removal methods relying on linear combination of sky maps, in whichever form, will produce similar results, as their defining assumptions resemble each other. The big advantage of the SMICA map, compared to other foreground estimation techniques, is the ignorance toward specific calibrations: the parameters in the model for $C_{\nu\mu}(\ell)$ can accommodate for any calibration errors etc. automatically.

The SMICA map, as any other linear combination method, can equally be applied to polarization maps. In the case of *Planck*'s SMICA implementation, $E$ and $B$ maps are used, and only later transformed to $Q$ and $U$ maps, for comparison with the other methods.

**Cleaning sky maps — Foreground separation algorithms** As opposed to blind techniques, parametric model fitting algorithms utilize models of foreground emission spectra, to tell CMB and foreground emission apart from each other, as well as distinguish foregrounds of different sort. A model of the sky as a frequency $\nu$ then can be written as

$$m_\nu(\hat{n}) = \Delta T(\hat{n}) + \sum_g a_{g,\nu}(\vec{\theta}_g(\hat{n})) A_g(\hat{n}), \tag{1.54}$$

where the index $g$ runs through the number of different foreground components. The foreground $g$ is described as an amplitude, $A_g$, scaled by the function $a_\nu$ through frequencies. The spectral

[18] I should mention that small spectral variations can, in principle, be accommodated by linear mixture methods. Consider a power law foreground spectrum with $a_\nu = a_\nu(\ell, m) \propto (\nu/\nu_0)^{\beta(\ell,m)}$. If $\beta(\ell, m) = \beta + \delta\beta(\ell, m)$ and $\delta\beta(\ell, m) \ll \beta$, one can write

$$F_\nu(\ell, m) = a_\nu(\ell, m) A(\ell, m) \propto (\nu/\nu_0)^{\beta(\ell,m)} A(\ell, m) \tag{1.52}$$

$$\approx (\nu/\nu_0)^{\beta} A(\ell, m) + \ln(\nu/\nu_0) \delta\beta(\ell, m) A(\ell, m). \tag{1.53}$$

A foreground component *with small* spectral variation can be treated as two separate, but correlated components, each *without* spectral variation. Naturally this requires data from more frequency bands. As will become clear in the next sections, the number of foreground parameters already exceeds currently available bands (and further $\delta\beta \ll \beta$ is not a given for every component).

shape $a_{g,\nu}$ depends on the parameters $\vec{\theta}_g$, characteristic for the respective component. Both $A_g$ and $\vec{\theta}_g$ are generally free to vary across the sky. The crucial part of this approach is to get the functions $a_{g,\nu}$ right for each component $g$. Obviously it is of everyone's interest to keep the total number of parameters $\vec{\theta}_g$ as low as possible, which can be done at the cost of simplifying assumptions about the foregrounds' behavior, or by introducing effective parameterizations and approximations. Section 1.2 will give an overview over some of the most important foreground phenomena and their most common parameterizations.

While above model can be fit via any sort of pixel-based fitting technique, in the presence of noise and degeneracies, it is most helpful to rely on a Bayesian approach. Classically, the posterior distribution of the parameters is written as

$$p(\boldsymbol{\theta}|\mathbf{S}) \propto p(\mathbf{S}|\theta)\mathcal{P}(\boldsymbol{\theta}) = \mathcal{L}(\theta)\mathcal{P}(\boldsymbol{\theta}) \tag{1.55}$$

for the collected signal data $\mathbf{S}$ (including all $S_\nu$) and parameters $\boldsymbol{\theta}$ (besides all $\theta_g$ now also including the amplitude of the CMB anisotropy $\Delta T$), and since the noise is approximately Gaussian, described by the noise covariance matrix $N$, the Likelihood $\mathcal{L}$ is constructed to be Gaussian as well

$$\mathcal{L}(\boldsymbol{\theta}) \propto \exp\left(-\frac{1}{2}\sum_\nu \left[S_\nu - m_\nu(\theta)\right] N^{-1} \left[S_\nu - m_\nu(\theta)\right]\right). \tag{1.56}$$

Planck 2015 results. X employs the Commander algorithm (Eriksen et al., 2004, 2008) as an efficient Gibbs sampling method. In their 2018 (PR3) release (Planck 2018 results. IV) they completely overhauled the algorithm which now works in harmonic space, rather than pixel space, and also alters certain parameterizations of foregrounds. Since, in this thesis, I present results from work based on the products from the 2015 (PR2) release, I will continue to describe the *Planck* results in terms of the methods and assumptions as of PR2.

The application to polarized sky maps is easier in terms of the reduced numbers of parameters, since only synchrotron and dust contribute significantly to foreground polarization, yet it is more challenging in terms of the lower sensitivity measurements. The Commander algorithm fits its foreground models to sky maps of the Stokes $Q$ and $U$ parameters. Due to lower sensitivity, the spectral parameters obtained from the temperature analysis are copied and held fixed, while only amplitudes are fitted. This may pose a problem for the extracted CMB maps, as the respective foreground spectra need not be the same in temperature and polarization.

**Cleaning the power spectrum** As mentioned before, cosmological parameter inference is done by comparing theoretically/computationally generated power spectra to those obtained from the CMB. Just above, it was shown how a (hopefully) clean CMB map can be calculated, which subsequently could be investigated in terms of its power spectrum, through Equations 1.27 and 1.29. Recalling the right panel of Figure 1.3, one could argue that in maps, like the one shown at 70 GHz, "enough CMB" peeks out from the Galactic foreground emission already, such that by simply barring the Galactic emission, one could estimate the CMB's power spectrum from the remaining sky.[19] This is, in fact, the main methodology of the *Planck* Collaboration for cosmological parameter estimation (as well as of earlier missions) and shall here be outlined briefly. (Planck 2015 results. XI)

After maps at frequencies close to the CMB maximum are selected and their Galactic planes masked, a likelihood approach is formulated as

$$\mathcal{L}(\widehat{\mathbf{C}}|\widehat{\mathbf{C}}(\Theta)) \propto \exp\left(-\frac{1}{2}\left[\widehat{\mathbf{C}} - \mathbf{C}(\Theta)\right]^{\mathsf{T}} \mathsf{C}^{-1} \left[\widehat{\mathbf{C}} - \mathbf{C}(\theta)\right]\right). \tag{1.57}$$

$\widehat{\mathbf{C}}$ contains the sky maps' power spectra, $\mathbf{C}(\Theta)$ is the model power spectrum with parameters $\Theta$, and $\mathsf{C}$ is the covariance matrix of power spectra from a fiducial cosmology, which is iteratively updated with the maximum likelihood search. The parameters $\Theta$ are of particular interest, since they not only describe the cosmology of interest, but also cover other aspects of the experiment, such as instrumental systematics, as well as foregrounds. Even after masking, a certain level of Galactic foreground emission is expected, and so are point sources, etc. For instance, inspired by observations at high frequencies, dust emission is modeled to scale as

$$C_\ell^{TT,\mathrm{dust}} \propto (1 + h\,\ell^k\,e^{-\ell/t}) \times (\ell/\ell_p)^n \tag{1.58}$$

with fixed(!) constants $h$, $k$, $t$, $n$ and a pivot scale $\ell_p$ — the spectral shape is fixed for all frequencies considered, and only an overall dust amplitude is left free per map (similarly for other foreground effects). With models and parameters at hand, the likelihood is maximized through Markov Chain Monte Carlo techniques, which conveniently are provided by CosmoMC, a program designed for this purpose (Lewis and Bridle, 2002).

With $2\ell+1$ modes for each multipole $\ell$, at small scales (high $\ell$) there is enough data to render the likelihood Gaussian and justify the parameterization 1.57. At large scales (low $\ell$), however, this is not the case and in order not to commit errors by using a overly optimistic likelihood

[19] One might rightfully argue that attempting to estimate quantities related to spherical harmonics, defined on the full sphere, from only parts thereof comes with additional problems; and indeed it does. This shall not be of concern here, but will be reviewed in Section 5, where such attempts are performed on polarization maps, where this problem is exacerbated. For now, it should be sufficient to state that there are solutions to this.

function, a hybrid approach is chosen: Up to a certain multipole $\ell_h$ the power spectrum is estimated from the COMMANDER CMB solution, and above it is estimated as described here. The likelihood at low $\ell$ does not have to account for anything else than CMB signal and noise, and its non-Gaussian shape is accounted for by a Blackwell-Rao likelihood (Chu et al., 2005).

### 1.1.6 Observation II

As seen in section 1.1.3, the anisotropies seen in the COBE maps in fact were expected. And in the previous section it was shown that through detailed study of these fluctuations is it possible to infer great knowledge about the Universe's history. Many experiments from the ground and from balloons were initiated to trace out the behavior of these fluctuations up to smaller and smaller scales. Simultaneously measuring both the large and the small scales, however, requires the launch of a satellite mission to detect this signal on the entire sky. After *WMAP* citep0067-0049-208-2-20 set new records on the precision to which the power spectrum could be measured, the *Planck* satellite topped this record again (Planck 2018 results. I). The SMICA map, the result of one of the CMB extraction algorithms, is shown in Figure 1.4 along with the measured and fitted power spectrum extracted from the data.

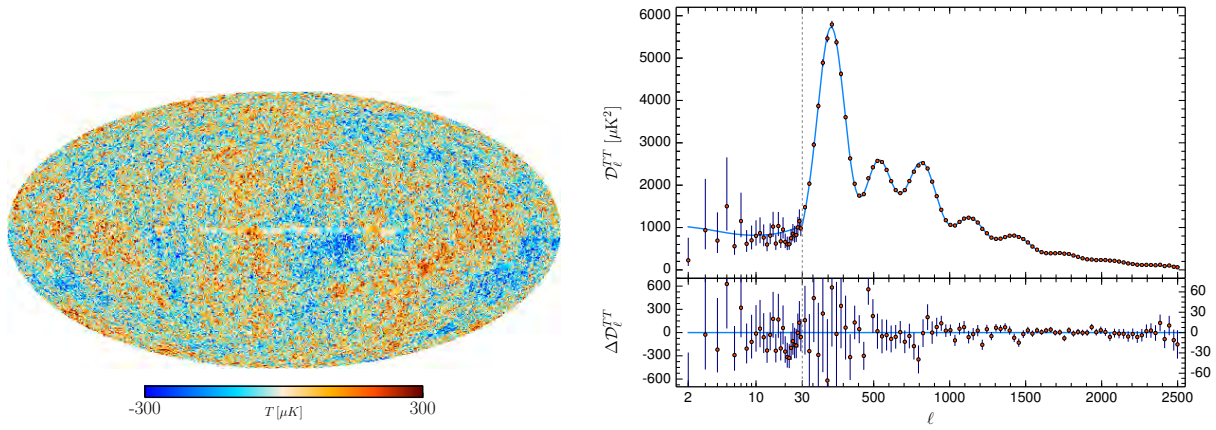


Figure 1.4 *Left panel:* The SMICA map as of PR3. *Right panel:* The full CMB temperature power spectrum ($\mathcal{D}_\ell^{TT} \equiv C_\ell\,\ell(\ell+1)/2\pi$) measured by the *Planck* Collaboration, as of PR3. (From Planck 2018 results. VI.)

Through Compton scattering during recombination, the CMB photons were polarized (the same effect, yet much weaker, occurs again during reionization). As was seen, also the metric perturbations produce such polarization. It is difficult to measure the fluctuations of the CMB polarization, and far more difficult to do so for the $B$-modes as their signal strength lies more

than five orders of magnitude below that of the temperature fluctuation signal. However, it is the power spectrum of especially the $B$-modes which provides the deepest insight into the perturbations present in the early Universe, most specifically their strength at low multipoles provides a measure for the energy scale of inflation, a mechanism I have not lost a word about yet; in short, it is the so far best candidate of theories to explain the growth of early quantum fluctuations to the structure we see in the Universe today (Baumann, 2011). As mentioned before, the strength of the $B$-modes at low multipoles relates to the ratio, $r$, of tensor to scalar perturbations[20]. For sake of completeness, I only show the result obtained so far by the *Planck* Collaboration for the $E$-mode power spectrum, $C_\ell^{EE}$ without going into details. The $B$-mode power spectrum of the CMB has not been measured yet. Instead, I show theoretical $B$-mode power spectra compared to best estimates of foreground cleaning residuals for planned CMB-S4 experiments. It should be emphasized that one must clean the observed polarization signal from all polarized foregrounds, and that the foreground removal shown here, still portrays a best case scenario. This thesis in concerned about making advances in understanding the foregrounds, described in the following chapters.

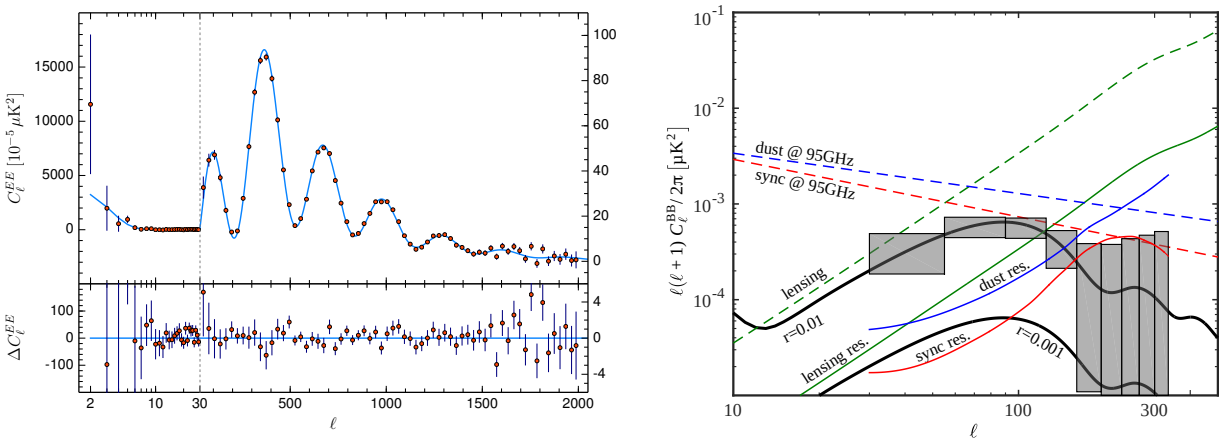


Figure 1.5 *Left panel*: The full CMB $E$-mode power spectrum measured by the *Planck* Collaboration, as of PR3. (From Planck 2018 results. VI.) *Right panel*: Theoretical CMB $B$-mode power spectra compared to forecasted residual contributions of foregrounds (in the cleanest 3% of the sky, and at the foreground minimum of 95 GHz) and lensing. Grey boxes depict the forecasted error bars of the binned power spectrum. (From Abazajian et al. (2016).)

[20]Recall, that only tensor perturbations contribute to the $B$-modes.

## 1.2 Galactic microwaves

Galactic emission is roughly classified into radiative properties of electrons (in synchrotron and free-free emission), dust grains (thermal emission as well as more exotic resonance behavior for historical reasons pooled into the term Anomalous Microwave Emission (AME)) and even (yet less pronounced) molecular absorption and emission. A basic understanding of these processes is essential for a critical examination of any treatment of CMB data including their results. The following sections should brief the reader on the most interesting characteristics of Galactic foregrounds, where emphasis is put on the spectral shapes commonly employed in foreground separation techniques. Section 1.2.1 covers synchrotron radiation and free-free emission, section 1.2.2 summarizes properties of thermal dust emission, and lastly, Section 1.2.3 lists aspects of AME, molecular line emission, and a suggested, and not yet understood component, the Galactic Microwave Haze. Other foreground effects, such as Zodiacal light, Galactic point sources, and extragalactic foregrounds, are not covered here. An excellent address to learn about these subjects are the papers by the *Planck* Collaboration on these foregrounds.

### 1.2.1 Galactic radio continuum emission

At frequencies of a few tens of GHz is where radio astronomy and CMB science overlap. Emission from thermal and non-thermal electrons provides the strongest low-frequency foreground (i.e. "low" in terms of CMB frequencies). In this context, mostly (however not always correctly) thermal radiation is understood to be equal to free-free emission and non-thermal emission to synchrotron radiation. Depending on the energy and the environment of the electrons, unexpected phenomena can occur, also such as thermal synchrotron radiation, or non-thermal free-free emission. This section provides a short overview of the more standard emission, in line with the foreground models currently employed in CMB science. For more advanced information I refer to Condon and Random (2016).

**Synchrotron radiation** The most dominant source of diffuse emission at frequencies of about a MHz up to tens of GHz is synchrotron radiation — bremsstrahlung by relativistic cosmic ray (CR) electrons accelerated by Galactic magnetic fields, in particular within the shock fronts of supernova explosions. The propagation of cosmic rays obviously depends on the structure of the magnetic field as well as their input momenta. The energy distribution of

these electrons is measured to approximately follow a power law,

$$n(E)\,\mathrm{d}E \propto E^{-\delta}\,\mathrm{d}E, \tag{1.59}$$

with spectral index $\delta$, where $n(E)$ is the number density of electrons per energy $E$. The brightness temperature of the emitted radiation inherits this power law and, for optically thin sources, one finds

$$T_B(\nu) \propto B^{(\delta+1)/2}\nu^{(5-\delta)/2} \equiv B^{3-\beta}\nu^{\beta}, \tag{1.60}$$

where I introduced the synchrotron spectral index $\beta$ which will appear repeatedly in this thesis. $\beta$ (or $\delta$) depends on the Mach number $M$ of the shock as $\beta = -(5M^2-1)/(2M^2-2)$, which for violent shock fronts leads to $\beta \approx -2.5$. Although, since the $M$ itself depends on varying quantities such as the local gas density, values between $-2.5$ and $-2.8$ are expected.

For observers this means that the synchrotron radiation detected in a particular direction on the sky is the line-of-sight integration of the bremsstrahlung, produced by the acceleration of different cosmic ray electron populations in different environments. While these differences are expected to be smoothed out to some degree, variations in the spectral index across the sky are expected, and have indeed been observed (e.g. Lawson et al. (1987); Platania et al. (2003); Guzmán, A. E. et al. (2011)).

At frequencies in the primary focus of CMB experiments, synchrotron radiation conventionally is modeled as a perfect power law, with a spectral index close to $-3.1$. In the Commander algorithm, the *Planck* collaboration, even though employing a spectral template from GalProp (a CR propagation code), essentially fit the synchrotron emission with

$$T_{\mathrm{B,syn}}(\hat{n}) = T_{\mathrm{syn},0}(\hat{n})(\nu/\nu_0)^{\beta(\hat{n})} \quad \text{and} \quad \beta(\hat{n}) = -3.11 = const. \tag{1.61}$$

Given the available data, the best fit was obtained, when keeping this index constant across the entire sky. However, keeping above measurements of spectral index variation in mind, it is likely that degeneracies with other low-frequency foregrounds, as free-free emission or Anomalous Microwave Emission (AME), discussed below, might lead to wrong conclusions. A representative image of our Galaxy's synchrotron emission (from our point of view) can be seen in Figure 2.1 below.

Since the CR electrons radiate in synchrotron, they lose energy, proportional to $E^2$, which softens their spectrum towards higher frequencies. At the same time, "fresh" CR electrons are

injected into the ISM, again via supernovae, hardening the overall spectrum to some extent. These processes may balance to another power law at higher frequencies of $\beta_{CI} = \beta - 0.5$. There are also other models than the Continuous Injection (CI) model (Pacholczyk, 1970) which discuss different energy loss mechanisms (see, e.g., Kardashev (1962)). Eventually, at high enough frequencies, an exponential cutoff develops (Jaffe and Perola, 1973).

Also here, a certain smoothing of (now broken) spectra is expected at observation (Basu et al., 2015). So far, breaks in synchrotron spectra have only been detected for other galaxies (Paladino et al., 2009; Klein et al., 2018). In current performance forecasts possible curvature is modeled via the unphysical parameterization used in Kogut (2012), $\beta \to \beta + C \log \nu/\nu_c$. An application of the more realistic model fits of non-thermal emission in our Galaxy must await the advent of higher-sensitivity broad band surveys.[21]

So far, determining cosmological parameters is done without particular attention to polarized synchrotron emission. Still there is reason in understanding its possible influence on obtaining clean CMB maps, especially at large scales. Synchrotron polarization should follow approximately the same spectrum as in intensity. However, a range of depolarization effects exist which alter its spectral shape, again, dependent on sky direction.

The most prominent is Faraday rotation. The evolution of polarization angles through a purely Faraday rotating medium is well understood: the complex fractional polarization $(Q + iU)/I)$ changes as

$$p(\lambda) = p_{\rm init} \exp\left(\psi_{\rm init} + \mathrm{FD}\lambda^2\right), \tag{1.63}$$

where $\lambda$ is the wavelength of the traveling light, $\psi_{\rm init}$ is the initial polarization angle, and FD is the Faraday depth, dependent on electron density and parallel magnetic field along the line of sight. However, any slightly more realistic model becomes sufficiently complicated. For instance, a medium in which Faraday rotation *and* further synchrotron emission occur

[21] In the to-be-published work Basu et al. (2019), not included in this thesis, it is forecasted that, in combination with upcoming C-BASS South data, and perhaps other low-frequency experiments, it will be able to constrain models capturing a break. These measurements, which will be performed at frequencies $\lesssim 10$ GHz, can predict emission to much higher frequencies, relevant for observations of the CMB. The synchrotron model proposed there reads

$$T_{\rm B,syn}(\nu) = T_{\rm syn,0} \frac{(\nu/\nu_0)^\beta}{[1 + (\nu/\nu_{\rm br})^\gamma]}, \tag{1.62}$$

where the index $\gamma$ governs the slope of the spectrum for frequencies $\gtrsim \nu_{\rm br}$, and $\nu_0$ is a reference frequency.

simultaneously, one already finds (Burn, 1966)

$$p(\lambda) = p_{\text{init}} \operatorname{sinc}\left(\mathrm{FD}\,\lambda^2\right) \exp\left(\psi_{\text{init}} + \frac{1}{2}\mathrm{FD}\lambda^2\right). \tag{1.64}$$

A long list of possible variations within the medium of propagation can be imagined, some of which already have been worked out, see Sokoloff et al. (1998).

None of this is directly used in this thesis. It is still helpful to keep in mind possible deviations from the models usually employed. Since Faraday rotation is mainly a low frequency phenomenon (it scales with $\lambda^2$) upcoming experiments targeting specifically this domain will have to consider these effects.

Maps of synchrotron polarization can be found in Figures 2.2 and 2.3.

**Free-free emission** Another kind of bremsstrahlung, free-free emission, is produced when thermal (non-relativistic) electrons scatter off ions/atomic nuclei in the interstellar medium, instead of magnetic fields. This process can be — save some quantum mechanical corrections — explained by simple Coulomb interactions. Again, the observed photon spectrum in a particular direction on the sky is an integration over the electron density along the line-of-sight and their input energy distribution. As they are assumed to be thermal the only parameter affecting this distribution is the electron temperature $T_e$, which typically lies between about 4000 K and 10000 K. In contrast to synchrotron radiation, and in the optically thin limit, free-free emission in the range of CMB experiments typically follows a flatter spectrum ($\beta_{ff} \approx -2.1$) and thereby can be present up to frequencies of a couple 100 GHz. The Commander algorithm employs a two-parameter model by Draine (2011), where $T_e$ is free to vary across the sky[22], thereby slightly changing the spectral index, though effectively it does not vary by much, and it was shown by Dickinson et al. (2003) that selecting above choice for $\beta_{ff}$ only biases the amplitude of free-free emission by $\lesssim 2\%$. .

As most ions in the ISM are protons, regions of free-free emission can be traced fairly well by H$\alpha$ emission maps, given that the H$\alpha$ emission is not scattered or absorbed by dust grains[23]. Of course, these maps can be abused as templates for an extraction of free-free emission, but are more useful as cross checks and in helping to estimate the electron temperature variation over different regions of the sky.

Typically, i.e. in a representative direction in the sky, one expects free-free emission to make

[22] Compare the applied prior on $T_e$ of $\mathcal{N}(7500\ K, 500\ K)$ to the typical values listed above!

[23] Depending on the region in the sky, data from other surveys can assist as well, such as HII emission or radio recombination lines, as well as using the star formation rate as a tracer. For a brief review about caveats of these methods, see Planck 2015 results. XXV.

up about 10% of all radio continuum at 1 GHz. Given its flat spectral slope, it becomes the strongest component of Galactic emission up until thermal dust emission sets in at around 80 GHz (200 GHz) at high (low) Galactic latitudes

### 1.2.2 Millimeter and infrared emission

At frequencies above a couple hundred GHz up to the far IR, Galactic emission is dominated by thermal dust emission — vibrational radiation from dust grains heated to an equilibrium temperature with the local radiation field. The dust temperature is comparably cold with values around 20 K. Interstellar dust grains can come in different sizes and compositions, accrete more material, and shatter through shock waves or single, highly energetic particles. Early, yet extensive observations from the COBE satellite found consistency with Polyaromatic Hydrocarbons (PAHs), as well as with silicate and graphite grains (Dwek et al., 1997). Especially the larger dust grains with characteristic sizes of $\sim 1\mu$m contribute most to the emissivity. For smaller dust grains, other mechanisms can become important, leading to modified behavior at lower frequencies (see Section 1.2.3 for a review of AME).

Just as before, the observed dust emissivity is the result of the light by all emitting dust grains along the line of sight. However, dense regions with high dust opacity absorb emission as well. For the frequencies of interest to CMB experiments, the final emission spectrum can be approximated as a so called modified black-body (MBB) spectrum, i.e. $\propto \tau(\nu)B_\nu(T_d)$, where $\tau(\nu)$ is the optical depth, defined as the product of frequency dependent dust opacity and gas column density, and $B_\nu(T_d)$ is *Planck*'s black-body spectrum at the dust temperature $T_d$. This purely empirical relation holds for $\tau \ll 1$ as happens to be the case for most regions of the sky. This shall be explored further in Section 3.1, where also images of the dust sky are shown, e.g. Figure 3.1.

It is pointed out in the review section of Planck 2013 results. XI that due to effects of possible variation of dust temperature and grain size along the line of sight on the spectral shape of the observed emission the quantities fit via this parameterization are not necessarily up for physical interpretation. Of course, more elaborate models have been built (e.g. Draine and Li (2007)), yet full inclusion into CMB foreground separation algorithms requires more data to accommodate for the increased number of parameters.

Lastly, asphericities in the dust grains' shape, allow for anisotropic emission profiles, and combined with metallic inclusions leads to alignment with Galactic magnetic fields: The thermal emission by dust becomes polarized. Polarization levels of this diffuse emission range up to 20%

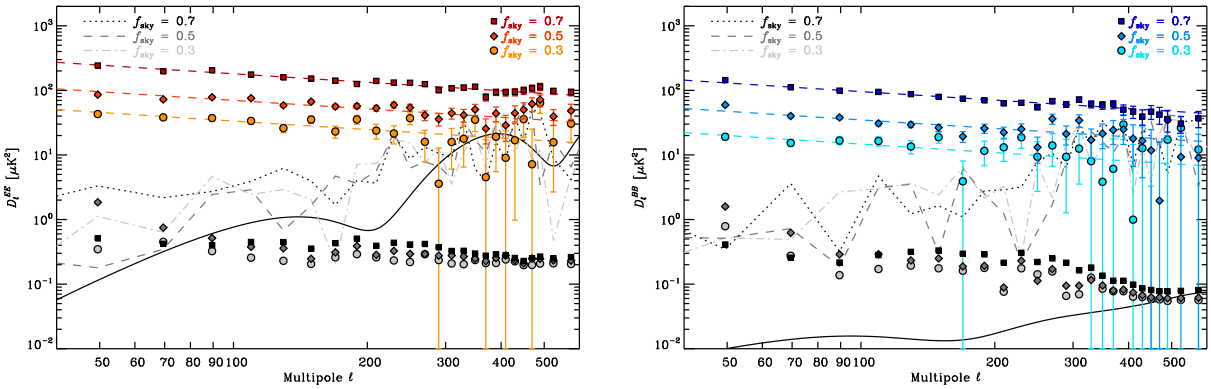


Figure 1.6 *Planck* 353 GHz polarized spectra showing power law behavior with multipole $\ell$. *Left panel:* The $EE$ power spectra. *Right panel:* The $BB$ power spectra. (From Planck intermediate results. XXX.)

outperforming those of the CMB. Around 100 GHz, where the CMB reaches its maximum dust is the strongest foreground and needs to be removed extremely carefully. A huge amount of effort has already gone into the characterization of dust, in particular its power spectra. In Figure 1.6 I reprint polarized power spectra, taken from emission at 353 GHz and at high Galactic latitudes, where the dust contribution is the weakest. For comparison of amplitudes, the solid black lines mark the expected $EE$ signal in the left and a $r = 0.2$ $BB$ spectrum in the right panel. Up until $\ell \sim 300$ scatter is comparably weak in both $E$ and $B$ modes. One could therefore be optimistic that despite the high amplitudes, subtraction of dust power via a simple model, as that shown in Equation 1.58, is viable also in polarization.

### 1.2.3 Other components

This section was written only to press for the reader's condolence regarding the seemingly hopeless task in telling apart all the different foregrounds: it is not enough that the foregrounds discussed above pose interpretational problems already; there are even more astrophysical phenomena contaminating our view on a clear picture of the CMB. I here pick out three effects which in most cases are part of component separation algorithms in some form. There are of course more phenomena, also of extragalactic origin, which are conveniently dealt with in pre- or post-processing, including point sources, the Sunyaev-Zeldovich effect, the Cosmic Infrared Background (not actually a background like the CMB) and even gravitational lensing, let alone atmospheric phenomena, essential in ground-based experiments. These all, even though interesting in their own regard are not dealt with here, at this point. The presentation is kept terse, as it does not immediately relate to active work from my side (– yet).

**Anomalous microwave emission (AME)** The three radiative components of the interstellar medium mentioned so far, in defiance of small modeling fragilities, are considered well understood and have always been part of foreground fits in CMB component separation methods. Intrigued by correlations of low frequency (tens of GHz) data with dust tracers at IR frequencies, speculations about an additional dust component emitting at low frequencies have been growing louder, baptizing this new yet unexplained component "Anomalous Microwave Emission" (Kogut et al., 1996; Leitch et al., 1997). Non-thermal emission by spinning dust, dust grains with an electric dipole moment rotating in the presence of magnetic fields, turned out to match precisely the missing component in spectra of peculiar regions in the sky (Draine and Lazarian, 1998). It appears, however, that also other exotic dust models can fit the spectra at low energies almost degenerately; such as magnetic dust models (Draine and Lazarian, 1999; Draine and Hensley, 2013), which instead of an electric dipole exhibit a magnetic dipole moment. There, external excitations disturb the aligned electron spins which subsequently seek to relax back into their state of minimal Coulomb energy under the emission of radiation.

Both these models have found support in observations (for a review, see Dickinson et al. (2018)). However, the many parameters determining the respective spectral shape, such as elementary composition of the dust grains, their size and shape, and dielectric behavior, can only be tested via observation, and to date are fairly unconstrained. More measurements at low frequencies are expected to break the degeneracy and reveal which of these dust models' emissions is/are actually present in our Galaxy (e.g. Dickinson et al. (2015)).

The most recent effort to include an anomalous dust component in full-sky foreground fits was done by the *Planck* Collaboration in Planck 2015 results. X. A compromise made of picking a model with the least number of parameters and obtaining satisfactory fitting results, they chose the spinning dust model of Draine and Hensley (2013); Draine and Lazarian (1998) compiled in the SpDust2 code (Ali-Haïmoud et al., 2009; Silsbee et al., 2011). The spectral form was fixed beforehand, to subsequently be shifted in the frequency–brightness temperature space as well as only in brightness temperature by corresponding parameters. (The similarity of the spectra of vastly different dust types, up to these two parameters, allows for this effective modeling.) However, in order to accommodate for the data a *second* spinning dust component had to be introduced artificially. This, in the context of spinning dust, is certainly unphysical and strongly hints towards necessary improvement in understanding what the AME is really composed of. Nevertheless, the results of the fit including this altered spinning dust model can be used for investigations into the relation between the different components, as discussed in Section 3.2.

The question to whether it is necessary to include magnetic dust as an additional component in such fits becomes greatly important in polarization measurements. While the two dust models (given the data to date) can be roughly degenerate in intensity, they exhibit significant differences in their polarization properties; spinning dust models describe polarized emission to levels not larger than 1% (Lazarian and Draine, 2000), magnetic dust models predict polarization fractions of up to 40% (Draine and Lazarian, 1999). Furthermore, their polarization direction is expected to be rotated by 90° with respect to each other. It is therefore of utmost importance to understand the subtleties in selecting the correct model if the extraction of the polarized CMB is to be reliable.

**Galactic Haze** By subtracting templates of above components from *WMAP*'s sky maps, Finkbeiner (2004a) identified a *haze* of residual emission, some tens of degrees in diameter, centered around the Galactic center, which he first interpreted as free-free emission from hot plasma. Subsequent work rather lead to interpreting this supposed excess emission as synchrotron radiation from electrons and positrons, produced by dark matter annihilation (Finkbeiner, 2004b; Hooper et al., 2007) or ejected by pulsars (Harding and Abazajian, 2010; Kaplinghat et al., 2009). With the publication of the $\gamma$-ray data from the Fermi-LAT satellite, additional support was found for the hazy excess emission (Dobler et al., 2010; Fermi-LAT Collaboration et al., 2014), morphologically similar to the counterpart at microwave frequencies [24], which in turn was followed by an own set of explanations (e.g. Su et al. (2010); Cheng et al. (2011);

[24] Though the microwave Haze has less pronounced edges, especially towards higher Galactic latitudes. Due to its pronounced shape(Su et al., 2010) the *Fermi Haze* now might be better known as the *Fermi Bubbles*.

Mertsch and Sarkar (2011) for a leptonic explanation). The leptonic construal has, in contrast to the hadronic hypothesis, the nice feature (amongst others) of offering a connection to the microwave Haze, i.e. synchrotron radiation and inverse Compton scattering is expected to be present at lower frequencies as well, which makes the establishing of the *WMAP* haze as an additional foreground component worthwhile. Following this, there has been a range of studies since, all finding a Haze by employing similar template subtraction methods — most recently by the *Planck* Collaboration in (Planck Intermediate Results. IX). It should be mentioned that skepticism towards the use of templates at an early stage was pronounced by Linden and Profumo (2010) concerning the $\gamma$-ray haze and by Mertsch and Sarkar (2010) concerning the Haze at microwave frequencies. While the Fermi Bubbles seem to stand strong despite this concern, more recent results from template subtracting analyses suggest only a lower amplitude of the *WMAP*/*Planck* Haze, in better agreement with proposed leptonic acceleration models.

Investigations of the spectral dependence of the Haze emission find approximately $B_\nu \propto \nu^{-0.5}$ or $T_B \propto \nu^{-2.5}$, consistent with a $\gamma$-ray spectrum of $\mathrm{d}N/\mathrm{d}E \propto E^{-2}$ detected with Fermi-LAT and spectrally distinct from both, synchrotron (approx. $T_B \propto \nu^{-3}$) and free-free emission (approx. $T_B \propto \nu^{-2}$). Additional information about the physics behind this occurrence is expected from polarization studies, however, to this date no polarization of the Haze has been detected. This is mainly due to noise and systematic effects in polarization measurements, but also due to limited understanding of the polarization of other components. It is curious to notice that the Haze is only extracted from microwave data if template subtraction methods are applied. If this signal indeed is present, pixel-by-pixel spectral fits, such as Commander, which so far do not consider any additional component designed to specifically target the Haze emission, will absorb the Haze emission into other components. In *Planck*'s Commander algorithm it most likely will be absorbed by AME — the only non-synchrotron and non-free-free emission process at low frequencies.

I show a map of this residual haze in Figure 1.7, where for visual purposes, I changed to color scale to enhance the structure. The shape of the structure is incredibly stable with respect to the templates and masks employed. However, given above discussion about component separation, one must be cautious still.

**CO and molecular line emission** About half the weight of the neutral ISM is measured to be due to molecular gas. At frequencies of $\sim 100\,\mathrm{GHz}$, emission from rotational state transitions of carbon monoxide molecules is the most dominant. Naturally, these transitions produce

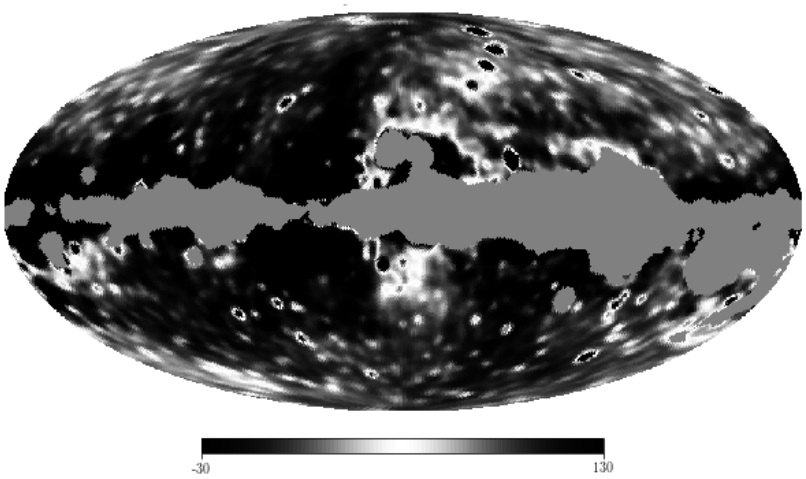


Figure 1.7 Image of the Galactic microwave haze (below the Galactic center, perhaps also above), as a detected residual after template fitting. The units are arbitrary.

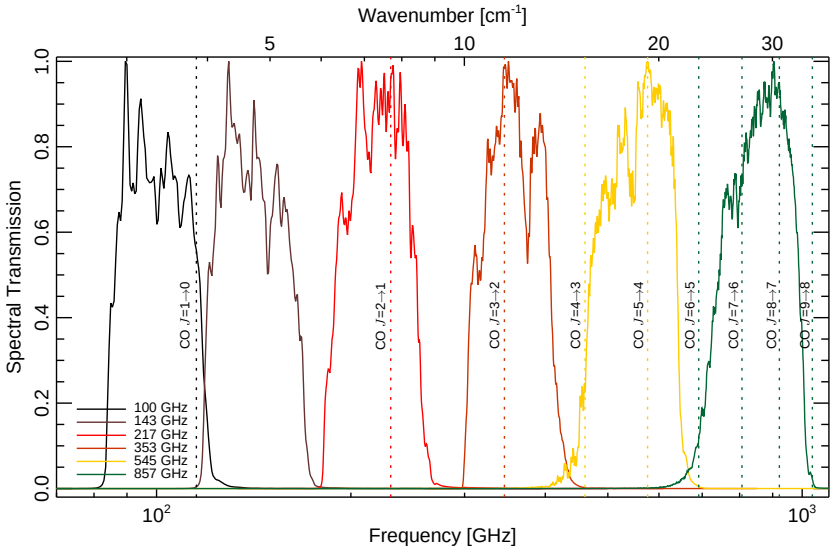


Figure 1.8 The average spectral response for each of the HFI frequency bands. The vertical dashed lines represent the first nine $^{12}$CO rotational transitions assuming zero velocity. (From Planck 2013 results. XIII.)

line emission in contrast to foregoing continuous spectra. While CO line emission in various molecular clouds and larger fractions of the sky was extensively studied, due to its multi-channel design the *Planck* satellite firstly has the opportunity to present full-sky maps of the respective transitions. Figure 1.8 shows lines of the $^{12}C^{6}O$ isotopologue in comparison to the detector responses of *Planck*'s HFI channels. Only the first three — J = $(1 \to 0)$, $(2 \to 1)$, and $(3 \to 2)$ — can be reliably extracted from the data; at higher frequencies thermal dust emission dominates the picture. But also these three frequencies are not without flaws, taking into account transition lines of $^{13}C^{6}O$ — another isotopologue of carbon monoxide — and calibration uncertainties, like the bandpass correction, the resulting maps carry up to ~ 10% systematic error (Planck 2013 results. XIII). The different CO extraction methods each have their caveats, though the systematic bias from these are thought to be included in quoted uncertainties. The right panel of Figure 1.8 shows the COMMANDER solution for the CO$(1 \to 0)$ transition (the maps for the other transitions can be obtained by simply scaling the shown map with factors 0.595 and 0.297, for CO$(2 \to 1)$ and CO$(3 \to 2)$, respectively); the CO maps obtained by the two other algorithms appear to be consistent with this one. It can be seen that the emission mainly concentrates to regions tightly following the Galactic plane. Furthermore, CO emission is found to be polarized only at the ~ 1% level (Greaves et al., 1999) and therefore is ignored in studies of CMB polarization. (see, however, Puglisi et al. (2017))

On the note of molecular lines, it is curious that the first detection of the CMB could have been already announced in 1941 when McKellar evaluated *absorption* lines from CN molecules in starlight spectra to find a non-zero population for the first exited rotational state corresponding to a temperature of ~ $2.3\,K$. At the time it was not understood which excitation mechanism was responsible for the abundance of excited cyanogen. Only later (Thaddeus and Clauser, 1966; Field and Hitchcock, 1966) it was seen that the absorption of CMB photons was the only viable mechanism.

## 1.3 Summary

Kick-starting the field of Cosmology, the discovery of the CMB has lead to answers but also many questions about our Universe. Well-understood statistical tools for the analysis of the CMB and other large data sets are becoming increasingly important to advance in deciphering the signature of the past. A range of upcoming surveys should will provide the necessary material for such investigations, but most certainly will also provoke new questions. Concerning Galactic foregrounds, there is much recent activity in adding information to CMB surveys by more precise measurements of radio foregrounds, such as C-BASS (Jones et al., 2018),

GreenPol (Fuskeland et al.), QUIJOTE (Génova-Santos et al., 2015), S-PASS (Krachmalnicoff et al., 2018), and a dish of the SKA (Basu et al., 2019). Chapters 2, 3.2 and 4 deal with low-frequency data; upcoming results from these surveys are greatly anticipated. After *WMAP* and *Planck*, proposals of other CMB satellite surveys have been made, such as CORE (Bouchet et al., 2011), LiteBIRD (Hazumi et al., 2012), and PRISM (André et al., 2014) which would make important contributions to CMB foregrounds at low and high frequencies. Chapter 3.1 presents current disagreements between foreground products measured with different data sets; also here an advancement in understanding foregrounds better would be achieved. However, a range of ground-based experiments such as ACTPol (Louis et al., 2017), BICEP2 (Ade et al., 2015a), CMB-S4 (Abazajian et al., 2016), POLARBEAR (Ade et al., 2017), the Simons Observatory (Aguirre et al., 2018), and SPT-3G (Anderson et al., 2018) are currently taking up data or are planned to do so in the near future. Their method do not always overlap with those appropriate for all-sky experiments. In particular for polarization studies this might lead to problems. The last part of my thesis, Chapter 5, addresses one of these problems. While necessary for ground-based experiments, the proposed method is also applicable to analyzing data from full-sky surveys.

In summary, this introduction attempted to give an overview of which techniques and which future data sets will illuminate our understanding of a many of astrophysical and eventually cosmological processes, and further even solve a range of current problems. Not in every case there is a straightforward way of solving it, but it is helpful to keep in mind the assumptions made initially which could lead to corresponding bias or misinterpretation in the data. In the following chapter I shall begin with elaborating on one such problem.

CHAPTER 2

# The imperfect CMB sky — Galactic Radio Loops

In light of the many late time influences on CMB photons, of the various, measurement-disturbing astrophysical phenomena (Section 1.2), as well as the necessarily approximate CMB extraction methods (Section 1.1.5), it must be made clear, that a pure CMB signal can only be obtained to a degree set by the knowledge of these impairments as well as the availability of a suitable solution. A certain level of shortcoming, however, is predetermined, and in this chapter I shall provide one particular example: the apparent residual emission in CMB maps by Galactic radio Loop I.

Like all main chapters in this thesis I begin with a chapter-specific motivation and introduction (Section 2). I then present results supporting the hypothesis that current CMB maps contain an imprint of prominent Galactic emission in form of a radio loop (Section 2.2). Thereafter I recapitulate arguments against these results (Section 2.3) which I discuss and counter with results of further investigations (Section 2.4). I conclude and also outline possible directions for future research in Section 2.5.

*The content of this chapter is based on von Hausegger et al. (2016).*

## 2.1 The Galactic radio loops

In chapter 1.2.1 it was outlined how Galactic synchrotron emission originates from non-thermal, relativistic Cosmic Ray electrons accelerated through magnetic fields in our Galaxy. Some of the most contributing sources of relativistic electrons are supernova explosions, or simply supernovae, which occur at a rate of $\sim 10^{-2}\,\mathrm{yr}^{-1}$ within the Milky way (Bergh and Tammann,

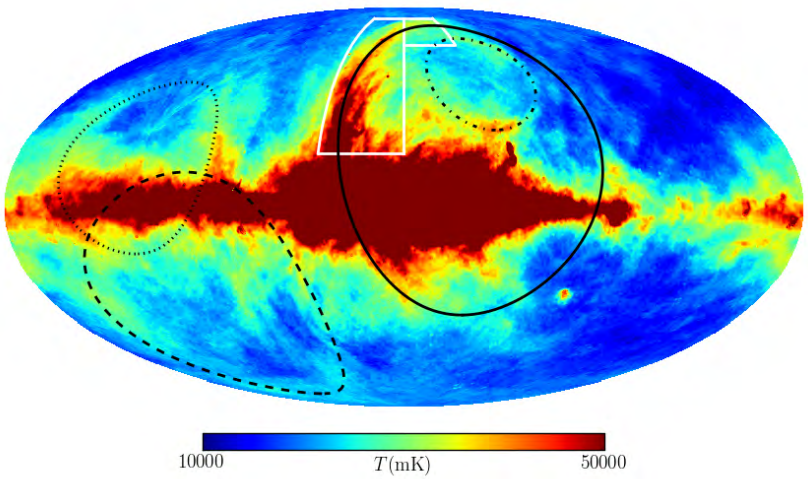


Figure 2.1 The 408 MHz Haslam map, as remastered by Remazeilles et al. (2015). Galactic Radio Loops I-IV are marked by black lines. Loop I is given by solid black. The white zones are parts of the so-called North Polar Spur (NPS). (From Liu et al. (2014).)

1991). Their strong shocks compress both magnetic fields and material from the interstellar medium making them appear as lit shells of diameters up to a few hundred pc before the end of their radiative phase. Given their occurrence rate, it is not surprising to find a hand-full of such supernovae close to us, and their shells therefore appear clearly visible on the radio sky. Figure 2.1 shows the radio sky in temperature as recorded by two ground-based surveys at 408 MHz, known as the Haslam et al. map (1982), or simply, 'Haslam map'.

The figure labels the four Galactic radio loops (the spherical supernova shells are projected onto the sky as loops) in our immediate environment. My primary interest will lie in the closest of them, Loop I, whose outline has been determined already early on by Berkhuijsen et al. (1971). Due to the strong shock front created by the outburst of material, the magnetic fields around such supernovae become exceptionally aligned, which, in addition to efficient particle (betatron) acceleration, leads to highly polarized synchrotron emission: One expects preferred polarization angles along the loop, which clearly delineate its shape. Indeed, imaging Loop I in polarization makes it even more visible, and by comparing the two images, one may ask whether the Loop's outline is perhaps better traced in polarization. I shall return to this point later in this chapter and for now will only mention that different emission mechanisms might be at play at different positions of the loop, which leads to features pronounced in temperature or in polarization, but not necessarily in both simultaneously. Nevertheless, in recent studies (Vidal et al., 2015; Ade et al., 2016b) the outlines of Loop I, and other loops and filamentary structures were determined by means of synchrotron maps of polarization intensity.

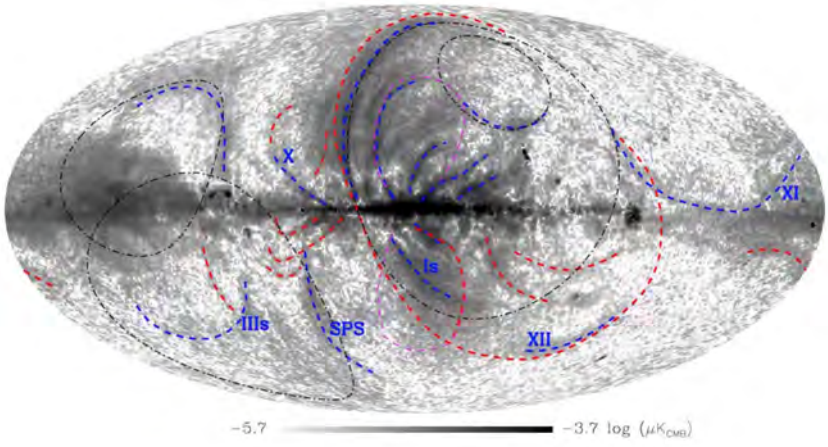


Figure 2.2 The 30 GHz *Planck* LFI map of polarization intensity as prepared by the *Planck* Collaboration (2016b). Outlines of loops and filaments as proposed in their paper are imposed onto the map. From Planck 2015 results. XXV.

With regards to Loop I they result in slightly different parameters. I show the corresponding map (the 30 GHz *Planck* LFI map) of the more recent work in Figure 2.2. There, Loop I is even presumed to be not one closed structure, but rather to be composed of two arcs, defined on grounds of aligned polarization angles in this map.

That the polarization is aligned along the approximately circular structure of supernova loops implies another property of the polarized sky: As seen in Chapter 1.1.4, the decomposition of a polarized signal on the sky into $E$- and $B$-modes makes use of rotational properties of the signal. In particular, the $E$-mode of polarization tends to pick up circular structures like those given by the Galactic radio loops. Dividing up the polarized synchrotron sky into $E$- and $B$-modes therefore leads to two maps, of which the $E$ map carries much more power than its complement, cf. Figure 2.3. In the next section I will present studies of possible contamination of CMB temperature maps by emission from loops, or in specific from Loop I. Clearly, contamination of the $B$-modes in CMB maps would have a dramatic effect on inferences of primordial physics, as outlined previously. According to Figure 2.3, $B$-modes might suffer less from contamination by structures like Loop I. On the other hand, any possible $B$-mode contamination due to unaccounted emission within the loop might also be less obvious to detect. Due to still comparably large uncertainties in polarization data and their products, studies of contamination in polarized CMB product is left for future work. The results to be presented here should, however, advise caution when considering CMB maps (of temperature or polarization) for the inference of cosmology, without respecting more local, astrophysical influences.

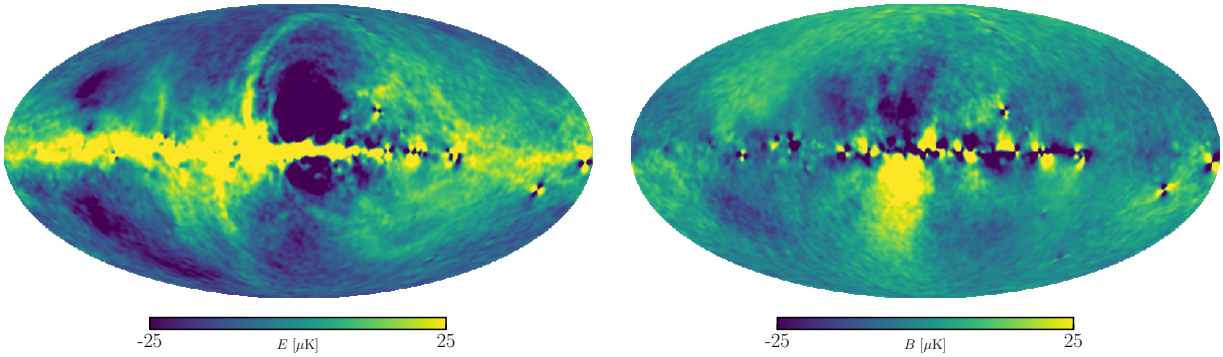


Figure 2.3 $E$- and $B$-mode maps of *Planck*'s 30 GHz LFI polarization measurements. Note the presence of Loop I in the $E$ map (*left panel*) and its near absence in the $B$ map (*right panel*).

## 2.2 Galactic Radio Loop I in the CMB

Since their first publication, CMB maps have been under constant scrutiny regarding their compliance with the eventually established standard model of cosmology. Particular attention was raised by the occurrence of so-called *anomalies* — statistical discordances with the expectation given by the concordance model (for a recent review, see Schwarz et al. (2016)). Most of them describe more-or-less unlocalized features which call into question the principles of statistical isotropy, but do not directly point towards a possible culprit. Alternatively, rather than performing searches for unlocalized peculiarities in the CMB maps, one might ask specific questions aimed at identifying contaminants of known origin. Such a contaminant might be some spatially localized astrophysical structure, whose influences left traces in CMB maps. The unusual properties of supernova remnants, compared to the average region in the sky, exhibit equally unusual spectra, which may cause difficulties in their separation from the microwave background. This was precisely the motivation of Liu et al. (2014), to hunt for traces of the Galactic Radio Loops in *WMAP*'s latest ILC map. In fact, they found a significant evidence for residual emission from Loop I, the most pronounced of the nearby Radio Loops, therewith immediately raising skepticism about the validity of current foreground separation/removal techniques. I will briefly review their methods and some of their findings first before turning to the updated analysis in von Hausegger et al. (2016).

If there was residual emission in the ILC map of the CMB caused by Loop I, one would expect to find a signal which, on average, is larger along the brightest parts of the loops, as compared to a level expected for a random realization of a CMB map, given our cosmology. Circumventing the look-elsewhere effect, Liu et al. therefore defined the region of interest to be

a narrow, ±2° band along the circular coordinates of Loop I as initially proposed by Berkhuijsen et al. (1971), namely a 116° wide small circle centered around $(l, b) = (329°, 17.5°)$. They filtered the ILC map to contain power only from multipoles $\ell \leq 20$ and found this map's mean value within the band to amount to $23.9\,\mu$K. CMB simulations based on *WMAP*'s best-fit ΛCDM power spectrum evaluate this to a $p$-value of 1%. Motivated by this, they proceeded to perform a cluster analysis aimed at testing whether the temperature of the hot peaks of this filtered CMB map in the vicinity of the defined circle, in this case a ±10° band along the loop, is correlated with their distance from it. The expected (negative) correlation (i.e. "pixels with higher temperature are closer to Loop I") could be found and they constructed a statistic[1] which, compared with simulations, gives a $p$-value of only $1.8 \cdot 10^{-4}$. Also other loops were investigated for that work; none, however, gave as significant results as Loop I. After the publication of the *Planck* products, these results were to be updated and with this reissue the opportunity was used to justify and improve previously made assumptions and statistics.

### 2.2.1 Loop I in Planck CMB maps

Since the foreground separation/removal techniques have essentially not changed since the release of the *WMAP* data, it is not surprising that the same signal along Loop I can be found in *Planck*'s CMB maps as well. However, the methodology of Liu et al. (2014) was to be improved to make the results more stable — their conclusions stand strong. In addition to presenting the results for the newer *Planck* maps, the contributions made by von Hausegger et al. (2016) are the following:

- The filtering to $\ell \leq 20$ is justified using a model of the Loop
- The validity of the results after barring the Galactic plane via various Galactic masks is tested
- An updated correlation statistic replaces the binned clustering statistic
- The question to whether other loops should be visible as well is addressed quantitatively

I present the results corresponding to the first three points in this order below. The last point will be taken up in the following discussion of section 2.2.2.

[1] This statistic, to create a cleaner view on things, includes binning the pixels within the band along Loop I according to their temperature, and subsequently evaluates the average distance of the pixels within the four hottest bins only.

**Low-pass filtering** The CMB maps used in the analyses above (and those below) all are reduced in angular resolution to only contain power from multipoles $\ell \leq 20$. A justification for the application of a low-pass filter is to be found in the relation of the map's correlation structure to the signal of interest. More specifically, it is expected that the *random* fluctuations intrinsic to the CMB will dominate starting at some scale such that any systematic offset in the map, as expected from remaining contamination, will be "washed out". Therefore a maximum angular scale is chosen suitable to these purposes, according to the correlation angle of the CMB. The signal of interest in this case is Loop I, whose emission can be described via a model proposed by Mertsch and Sarkar (2013), see Figure 2.4, and the (smallest) angular scale of interest is determined by the width of Loop I, which I estimate by measuring the full width at half-maximum (FWHM) of the loop's profile, as shown in the right panel of the same figure. Depending on the definition of the profile's maximum, I obtain values, $\theta_{\mathrm{loop}}$, for the FWHM of roughly between 7° and 11°. On the other hand, the correlation angle $\theta_c$ of a field is defined as the angle at which the two-point correlation function $C(\theta)$ reaches half its maximum value, $C(\theta_c) = C(0)/2$. This is seen by expanding the two-point correlation function around zero as

$$C(\theta) = C(0) + \frac{1}{2}C''(0)\cdot\theta^2 + \ldots \approx C(0)\left(1 - \frac{1}{2}\frac{\theta^2}{\theta_c^2}\right), \tag{2.1}$$

where primes indicate differentiation with respect to $\theta$ and further

$$\theta_c^2 \equiv -\frac{C(0)}{C''(0)} = \frac{2\sum_{\ell=2}^{\ell_{max}}(2\ell+1)\,C_\ell}{\sum_{\ell=2}^{\ell_{max}}(2\ell+1)(\ell+1)\,\ell\,C_\ell}, \tag{2.2}$$

where $\theta_c$ only depends on $\ell_{max}$ for a given power spectrum $C_\ell$. The two scales $\theta_{\mathrm{loop}}$ and $\theta_c$ should be made comparable by choice of $\ell_{max}$. For the SMICA map, the choice $\ell_{max} \simeq 20$ provides a good average value, and it does not change much for other CMB maps or even the best-fit power spectrum, see left panel of Figure 2.5. A map of the CMB reduced to these multipoles can be seen in the right panel of the same figure with the Galactic loops indicated.

**Masking** As in Liu et al. (2014), I first compute the average temperature of the $\ell \leq 20$ CMB maps in a ±2° band along the Loop I and compare this to values obtained from simulations for an estimate of significance, see table 2.1, which lists the mean values and corresponding probabilities to obtain an equally large or larger mean value in simulations, for both the *Planck* 2015 SMICA map as well as the *WMAP* 9yr ILC map, for comparison. Both maps are additionally masked with their respectively suggested masks to investigate the effect on the significances. The $p$-values of the ILC9 and SMICA map agree with one another, as expected. When masks

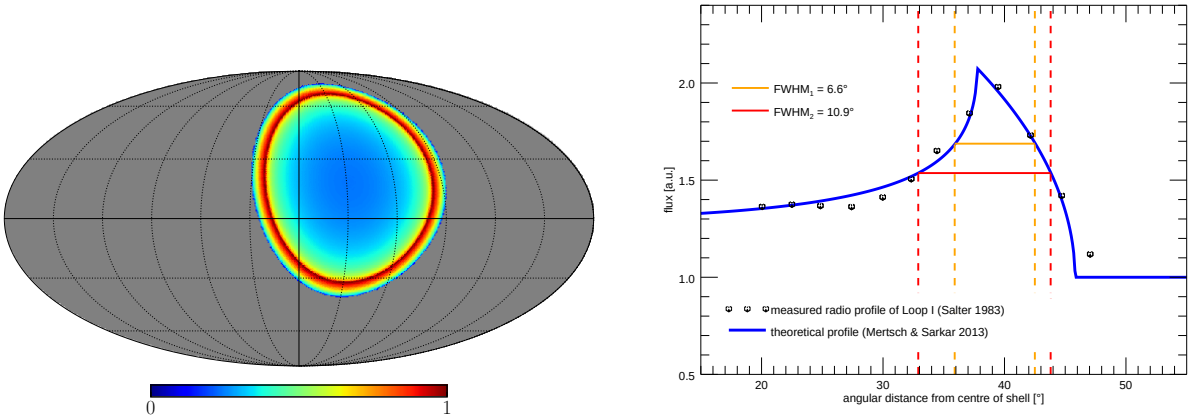


Figure 2.4 *Left panel:* The emission model for radio loops of Mertsch and Sarkar (2013) with the parameters of Loop I. *Right panel:* Profile of the model with the FWHM angle $\theta_{\text{loop}}$ indicated.

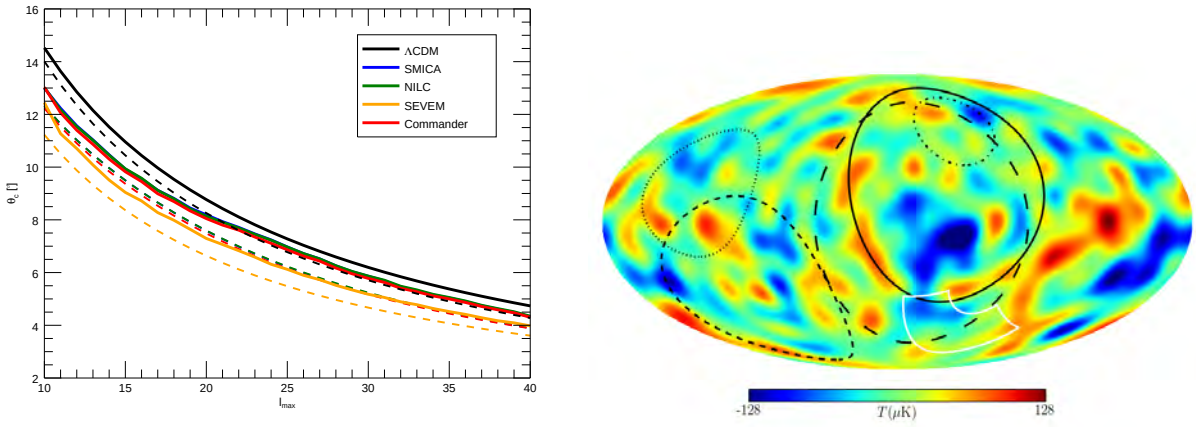


Figure 2.5 *Left panel:* CMB maps' correlation angles vs. $\ell_{\text{max}}$. *Right panel:* SMICA map filtered to $\ell_{\text{max}} = 20$ with Galactic radio loops indicated.

are applied the rise in $p$-values (while still retaining percent levels) is attributed, in part, to the increased sample variance due to decreased sky fraction. Thereby, the much smaller SMICA mask leads also to a smaller increase in $p$-value.

**Correlation statistic** To underline that the previous observation of increasing pixel temperature with decreasing angular distance between the corresponding pixel and the center of Loop I is a *global* effect and not just determined by the four highest temperature bins, von Hausegger et al. (2016) presents a bin-free statistic, essentially a Pearson's cross correlation coefficient of pixel temperature $T(p)$ and pixel distance $G(p)$, for all pixels within the $\pm 10°$ band:

$$K(G,T) = \frac{\sum_{\mathrm{p}}(G(\mathrm{p}) - \overline{G})(T(\mathrm{p}) - \overline{T})}{\sqrt{\sum_{\mathrm{p}}(G(\mathrm{p}) - \overline{G})^2 \sum_{\mathrm{p}}(T(\mathrm{p}) - \overline{T})^2}}, \tag{2.3}$$

where $\overline{G}$ and $\overline{T}$ are the sample average values of $G(\mathrm{p})$ and $T(\mathrm{p})$, respectively, for pixels p within the Loop I region. The results are consistent with the previous findings and are shown in table 2.1 as well. Also here, the $p$-values calculated for the SMICA map remain within the same order of magnitude, even with the Galactic plane mask applied. It should be emphasized that the correlation coefficient is normalized such that it only respects relative deviations from the mean, and not absolute amplitudes. The $p$-values show that the alignment of hot spots along Loop I remains peculiar at a level of $10^{-4}$, even in the presence of masks. In fact, most hot spots of Loop I lie outside the Galactic plane masks appropriate for the respective maps. If still the anomalous signal is attributed to contamination from the Galactic plane, the sizes of the proposed masks according to this test, are chosen not conservative enough. However, it is entirely possible that the way current understanding of Galactic foregrounds is built into foreground separation algorithms is insufficient.

### 2.2.2 Physical reasoning

Assuming that above tests established the presence of residual emission from Loop I in the CMB maps, two questions still remain to be answered: 1. How could this emission emission pass through the foreground removal algorithms? and 2. Other supernova remnants on the sky are known. Where are their imprints in the CMB maps?

As elaborated in Section 1.1.5 (and discussed more in Section 4.1), the ILC method, makes very specific demands on the foregrounds' behavior. Most importantly, it requires a spatially

Table 2.1 *Two left columns:* The mean temperature in a ±2° band along Loop I and the corresponding chance probabilities in various CMB maps. *Two right columns:* The cross-correlation $C(d,T)$ between the distance of pixels and their temperature value in a ±10° band along Loop I.

| map | mask | $\overline{T}\,[\mu K]$ | $p$-value | $C(d,T)$ | $p$-value |
|---|---|---|---|---|---|
| ILC9 | none | 23.9 | 0.01 | -0.22 | $7 \cdot 10^{-4}$ |
| ILC9 | KQ85 | 15.4 | 0.09 | -0.17 | $1.5 \cdot 10^{-2}$ |
| SMICA | none | 22.8 | 0.01 | -0.20 | $1.4 \cdot 10^{-3}$ |
| SMICA | SMICA | 21.8 | 0.02 | -0.20 | $2.6 \cdot 10^{-3}$ |

constant spectral scaling. Finding an excess signal in a specific region of the sky might therefore hint towards a violation of this requirement. In fact, the ILC weights computed on those parts of the sky excluding the Loop I region and those computed within the Loop I region differ substantially, as was already shown by Liu et al. (2014). Furthermore, the same authors argued that, surprisingly, synchrotron radiation cannot account for the entire excess detected — the accepted spectral index of synchrotron emission is readily "zeroed" by the ILC approach (also within the loop). Rather they proceeded to investigate multi-component dust models and (with the limited information on higher frequencies given by *WMAP*) conclude that a second dust component may indeed be present in the sky. To be consistent with the observations at all *WMAP* frequencies, they suggested magnetic dipole emission (Draine and Lazarian, 1998; Draine and Hensley, 2013) as a possible source. For this to be true, dust grains within the shock front of the remnant would have to contain a sufficient fraction of metallic iron without being shattered apart by the pressure wave. Detailed investigations of this hypothesis as well as an explanation for the non-appearance of higher polarization fractions in this region are still outstanding. Finding a signal in CMB products from spectral fits (e.g. Commander), which do not necessarily assume spatially constant spectral indices, also leave open the possibility of an additional, not modeled component. As shall be seen below, the AME component utilized by the Commander algorithm gives puzzling results, which may be a hint of a component which is not well enough described by the chosen parameterization.

The second question can be answered rather quickly by arguing that not every supernova remnant must have the same emission characteristics, e.g. by different dust grain content. Their ejecta depend strongly on the type of the progenitor system, the specific explosion dynamics, as well as their local environment. However, we would have to call ourselves particularly unlucky to have the one supernova remnant with untamable emission spectra right in front of our face.

As there are no noticeable imprints of the other three close-by remnants, it should at least be expected that some of the many thousand remnants distributed over the Galactic plane exhibit similar properties. This question was picked up in von Hausegger et al. (2016), where the estimated total column density of the nearby loops and a simulated distribution of supernova remnants within the Galactic disk (as described in Mertsch and Sarkar (2013)) was compared with the likewise estimated column density of Loop I. This rough comparison leads to the conclusion that emission from supernova remnants within the Galactic plane only dominates the emission from Loop I within latitudes $|b| \lesssim 5°$ on average, see Figure 2.6. It should be repeated, that not all "loops" are expected to contribute the same amount of emission, let alone the anomalous emission suspected from Loop I; this estimate therefore is most likely an overestimation.

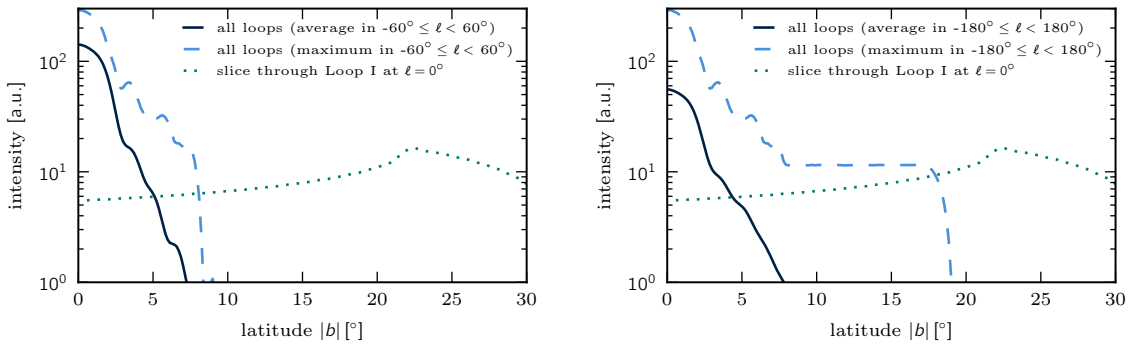


Figure 2.6 Latitudinal profiles of the column density through the simulated Galactic population (Mertsch and Sarkar, 2013) of all loops in the longitude intervals indicated, compared to a slice through Loop I.

In Planck 2015 results. XXV, the *Planck* Collaboration replies to the claims presented in the sections above, and presents their own, different interpretation of these results. In the next section I recapitulate their counter arguments and contrast them with further considerations. While magnetic dust was hypothesized as a possible culprit, it should be said, however, that to this date no further studies which would provide additional support for or against this hypothesis were undertaken. It is hoped for that broadband polarimetric measurements at radio bands with high sensitivity will settle the question about the nature or AME (e.g. by the SKA (Dickinson et al., 2015)) and therewith that about the signal in Loop I — so far, polarization measurements are simply not sensitive enough.

## 2.3 Planck's response

Confronted with the claim of residual contamination in their main CMB products, the Planck 2015 results. XXV chooses a different viewpoint to interpret the $\sim 3\sigma$ anomaly. They see this interpretation supported on several grounds. For the sake of a complete discussion I list these grounds here. In short, they read:

- The model, a band with constant width along a small circle, is not appropriate:
  - Perfectly circular structures on the sky are unlikely. Loop I should therefore not be modeled as a small circle, as distortions are expected.
  - The coordinates of this model were defined using data from the Northern hemisphere only; it therefore is not supported by measurements in the South.
  - More precise measurements of the loop's parameters can be done via polarization measurements.
  - Real thermal dust emission data and even synchrotron emission data both look different than the small circle band (the small circle was fitted upon the latter of the two).
- The alignment of the CMB's hotspots with the proposed loop can occur by chance — the look-elsewhere effect has not been taken into account.
- If anomalous emission (AME, or anything else for which was not accounted) from Loop I made it past the foreground removal, where is the residual from the other $\mathcal{O}(100)$ loops, expected in the Galactic plane?

I answer to these arguments in opposite order:

- In section 2.2.2 the question to whether a signal from other SNRs should be expected was addressed already: Estimates give column densities, larger than those along Loop I only within latitudes $|b| \lesssim 5°$ — latitudes where the CMB products are usually masked due to large uncertainties. Planck 2015 results. XXV point out rightfully, that even though the signal along the Galactic plane is cautiously masked, all CMB maps (except SEVEM) show no such excess at said latitudes.

  As stated before, the estimate was made assuming that all SNRs contribute emission at the same level. Due to various reasons (different dust content, different compression

factors, different ages) this need not be the case. In addition, their spectra may be different, wherefore the foreground removal algorithms may "react" differently to them than to the emission from Loop I. The predicted anomalous emission along the Galactic plane therefore easily is an overestimate. Further, one could assume other components whose emission correlates strongly with the anomalous emission's Galactic plane part, to "absorb" this emission more effectively than within Loop I. To date, this issue is not yet settled.

- I argue that the look-elsewhere effect cannot be requested here, as the calculations are based on a fixed model, namely emission concentrated within a band along a small circle. The motivation (however flawed it may be) to seek for such emission specifically forbids variation or introduction of parameters, such as the loops position or shape.

- Finally, the model in use is questioned and correlations with more realistic emission properties than a small circle are suggested to be preferred. In particular those emission patterns Loop I shows directly in synchrotron maps or thermal dust maps are said to be better models of potential residual contamination in CMB maps, and additionally polarization measurements would provide better tracers of the loop's parameters.

  If the contaminating emission indeed comes from magnetic dust, no specific "template" exists; using the full Haslam map or a map of thermal dust emission as templates therefore would have its own flaws. The same holds for polarization maps. A rough model, like the simple loop chosen here therefore might be preferable, although a certain degree of bias also here is unavoidable. Never the less, additional tests can be performed to exclude preoccupation towards an oversimplified model. To this effect, I present in the next section an analysis similar to that above, but instead of employing a loop as determined from the Haslam map, I employ filaments, which were measured by Vidal et al. (2015) on a polarization intensity map, and rubber-stamped in Planck 2015 results. XXV.

## 2.4 Loops and filaments

In section 2.2 the coordinates of Loop I were fixed by adopting the parameters listed in Berkhuijsen et al. (1971) and derived from temperature observations. Vidal et al. (2015) and later also Ade et al. (2016b) ((Planck 2015 results. XXV)) argue that since the loops as well as filamentary structures appear more pronounced in polarization, measurements of Galactic structures must be done here instead of in temperature, hence also the parameters of Loop I must be updated: In an attempt to catalogue and characterize polarized structures on the radio

sky Vidal et al. (2015) analyzed a de-biased map of *WMAP*'s K-band polarization intensity. Amongst these were the well known Radio Loops I-IV. Repeating above analysis on these updated segments of Loop I addresses two of the points raised by the *Planck* collaboration: 1. Loop I most likely is not described by a small circle, and 2. Polarization intensity measurements might describe the loop's coordinates more accurately.

Besides the Radio Loops also other known as well as previously unknown structures could be identified. Most of these structures, according to the authors, could only be found in maps of the polarization intensity, not in temperature maps, and seem to follow *segments* of small circles on the sky, some reaching up to about 60° off the Galactic plane. All arcs were shown to have in common Galactic magnetic field lines aligned with the direction of the loops and exhibit comparably high polarization-to-intensity ratios at about 30%. While not all these structures are well pronounced on temperature maps, their underlying mechanism should still contribute to emission at a lower level. Assuming that their exceptional appearance is due to exceptional features in their respective emission process, motivates to question whether foreground removal in these regions has been successful. Employing the same methods as before I investigate all filaments reported by Vidal et al. (2015) with regard to their appearance in temperature maps of the CMB. Any significant finding would again hint towards shortcomings in the removal of astrophysical influences.

### 2.4.1 Loop I and the filaments

Vidal et al. (2015) provide the parameters of the loops along which the arcs they found lie.[2]

Figure 2.7 shows a reproduction of their arcs where each one was defined by selecting a segment of its corresponding loop.[3] I have highlighted the arc they denote "IIIs" in yellow, as well as "I", "Is", and "XII" in green as they will merit further attention in the remainder of this chapter.

**Low statistical moments in filaments** As before, I begin by computing mean value, variance, skewness, and kurtosis of the temperature distributions in the CMB map in each of the segments; again, I employ the *Planck* 2015 SMICA map (Planck 2015 results. IX), smoothed

[2]With exception of the radii for loops V, and VI, and arcs IIIs, X, XI and XII all other parameters are adopted in this work. Said radii seemed to be off by factors of 2. The corrected values can be found in table A.1 in the appendix of this paper. The corrections have been confirmed with the authors.

[3]Even though the segments themselves were selected solely by visual inspection of Figure 2 in their paper, the statistics employed here do not react sensitively to small changes in the extent of the particular segments.

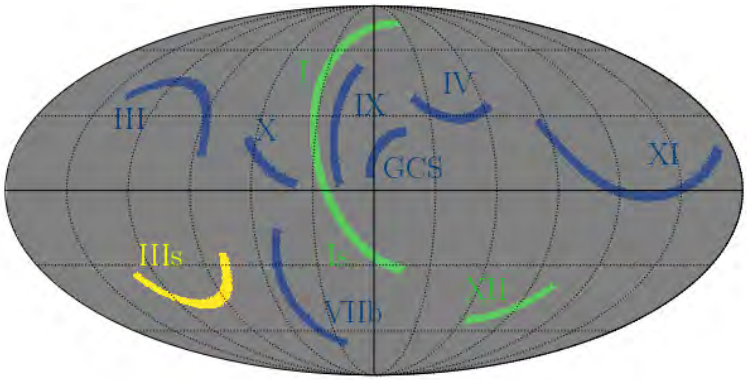


Figure 2.7 Positions and extents of the arcs taken from Vidal et al. (2015) with the corrections listed in table A.1. All arcs are shown with a width of ±2°. The graticule has a spacing of 30°.

to only contain multipoles $\ell \leq 20$, and at HEALPix resolution $N_{\mathrm{Side}} = 128$. It should be noted that even though this range of multipoles was determined by the characteristic width of Loop I this width need not apply to all loops/arcs found on the sky. However, in order not to include more free parameters I here retain all the parameters chosen previously for all loops/arcs investigated here and therewith also pick the same $\ell_{max} = 20$. I have tried out a range of different parameters under which my conclusions remain unchanged. In addition to defining the region of interest to be only within an arc of given width, I compare my results to those obtained after masking the same region with the *Planck* 2015 Common mask[4].

Table 2.2 shows the results for all arcs shown in Figure 2.7, after having applied the mask. Many loops/arcs appear peculiar at the percent level according to different moments — a level which calls for more attention, especially given the crude statistics used here.[5] The arc connecting the NPS part of Loop I with its southern "appendix" has a $p$-value at the very same level as the full loop. Also Loop III and its arc selected by Vidal et al. seem to have an unexpectedly low variance — a connection which I will touch upon below. In this context it is of interest to find that arc IIIs appears to lie on a comparably cold patch of the CMB, as told by the large $p$-value of its average temperature.

**Distance–Temperature correlation in filaments** Keeping contamination along arcs in mind and motivated by named $p$-values I turn to investigate ±10° bands along the respective

[4]This mask includes all of the SMICA mask and additionally masks parts of the Fan region and of the Galactic center.

[5]Note that I did not define the $p$-values symmetric ("what is the frequency with which a value *larger* than the one calculated is obtained by chance"), such that values close to unity are just as unusual as those close to zero.

Table 2.2 $p$-values of statistical moments calculated on the unmasked and the masked SMICA map with $\ell \leq 20$. (Probability of finding the computed value or *higher*)

| Loops | Mean | Variance | Skewness | Kurtosis |
|---|---|---|---|---|
| I | 0.023 | 0.574 | 0.827 | 0.561 |
| II | 0.246 | 0.353 | 0.985 | 0.029 |
| III | 0.547 | 0.97 | 0.082 | 0.214 |
| IV | 0.683 | 0.591 | 0.943 | 0.052 |
| Arcs | | | | |
| I+Is | 0.013 | 0.761 | 0.921 | 0.049 |
| III | 0.746 | 0.957 | 0.36 | 0.266 |
| IV | 0.416 | 0.903 | 0.29 | 0.282 |
| GCS | 0.147 | 0.208 | 0.767 | 0.799 |
| IIIS | 0.946 | 0.624 | 0.86 | 0.218 |
| VIIb | 0.215 | 0.887 | 0.359 | 0.668 |
| IX | 0.263 | 0.182 | 0.33 | 0.926 |
| X | 0.467 | 0.707 | 0.636 | 0.798 |
| XI | 0.477 | 0.582 | 0.812 | 0.578 |
| XII | 0.168 | 0.512 | 0.239 | 0.872 |

arcs, with the correlation statistic, $K(G,T)$, as before. The resulting correlation values along with their probability to occur by chance can be found in table 2.3.

As before, the $p$-values decrease by an order of magnitude when Loop I is viewed through the correlation statistic. Also the $p$-values for the combination of arcs, I+Is, shrink by a factor of a few and remain unusual. This shall be discussed below. The peculiarity of Loop/arc III, from Table 2.2, however, is not supported by the correlation statistic. However, arc IIIs stands out significantly with $p$-values on the order of $10^{-3}$–$10^{-4}$. Before turning to these two cases in more detail in the following section (2.4.2), I briefly mention the filament denoted "GCS", or Galactic Center Spur, which also in the SMICA map follows warmer pixels whose temperature decreases with increasing distance from the central band. Due to its small extent (when masked with the Common mask, almost the entire structure is covered) not much departure from expectation can be found; however, it should be kept in mind that contamination from these structures might be present none the less.

Table 2.3 Correlation values and corresponding $p$-values calculated on the masked SMICA map with $\ell \leq 20$. (Probability of finding the computed value or *lower*)

| | No mask | | Common int. mask | |
|---|---|---|---|---|
| Loops | C(G,T) | $p$-value | C(G,T) | $p$-value |
| I | -0.2 | 0.0009 | -0.2 | 0.0018 |
| II | -0.05 | 0.2233 | -0.11 | 0.0949 |
| III | 0.03 | 0.6366 | -0.06 | 0.2333 |
| IV | 0.16 | 0.9082 | 0.17 | 0.919 |
| Arcs | | | | |
| I+Is | -0.23 | 0.0097 | -0.2 | 0.0198 |
| III | -0.0 | 0.4986 | 0.01 | 0.5297 |
| IV | 0.06 | 0.5968 | 0.12 | 0.6891 |
| GCS | -0.46 | 0.0437 | -0.58 | 0.0149 |
| IIIs | 0.53 | 0.9988 | 0.54 | 0.9992 |
| VIIb | 0.02 | 0.5489 | 0.01 | 0.5145 |
| IX | -0.11 | 0.2709 | -0.05 | 0.4221 |
| X | 0.01 | 0.5199 | -0.18 | 0.3416 |
| XI | -0.03 | 0.4217 | 0.33 | 0.9348 |
| XII | 0.18 | 0.7633 | 0.15 | 0.7287 |

**Combinations of filaments** The *Planck* Collaboration writes "We consider it plausible that filament XII represents the outer boundary of Loop I" (Planck 2015 results. XXV). Filament XII appeared as rather unremarkable in the previous section. Nevertheless, prompted by the suspicion that filaments I+Is and XII (marked green in Figure 2.7) belong to the same structure, I compute above $p$-values also for the combination of them: Again drawing a ±2° wide band along both arcs I find mean values of 37.7 $\mu K$ (35.4 $\mu K$) for the unmasked (masked) case with corresponding $p$-values of 0.016 (0.019). These are as low as the $p$-values obtained from the "old", full Loop I! If filaments I, Is, and XII indeed are part of the same structure, again, support is found for there being excess emission along parts of its outline. I also quote the measurements of the correlation statistic in ±10° bands, which give -0.19 (-0.16) with corresponding $p$-values of 0.0113 (0.0309). This reduced significance was to be anticipated from the respective measurements of the correlation in table 2.3, where the correlation within filament XII is found to have opposite sign of that of I+Is.

If one follows Planck 2015 results. XXV and rather puts trust the filaments attributed to Loop I (I, Is, and XII) than Berkhuijsen's parameters one will have to admit that the percent level deviation from expectation of the mean value of the SMICA map in not only filaments I+Is, but also the combination of I+Is and XII is a strong indicator for contamination from foreground emission associated with these regions. The departure from circularity of Loop I and the only effective description of the position of the loop's edge by detached filaments may be taken as an explanation why the correlation statistic does not show $p$-values at levels as low as previously estimated for the perfect loop. However, finding a better description of the dynamics of this region (e.g. its shape and magnetic field) seems essential to testing contamination properly.

### 2.4.2 Loop IIIs

The discovery of the unusually cold temperature following filament IIIs was rather unexpected: Within the (yellow) ±2° band shown in Figure 2.7 the average temperature of the $\ell \leq 20$ SMICA map is $-35.8 \mu K$ and even decreases to $-39.3 \mu K$ after having applied the Common mask. While its mean value did not appear all too peculiar, it was the correlation statistic which singled out this region from simulations, showing a *positive* correlation value, corresponding to an *increase* in temperature with *increasing* distance from the central band. It is implied by Vidal et al. that Filament IIIs manifests the Southern hemisphere part of Filament III (part of Loop III). By the same argumentation as in the previous subsection, I investigate the combination of both structures: Again, the statistical moments give no evidence for abnormality stronger than at

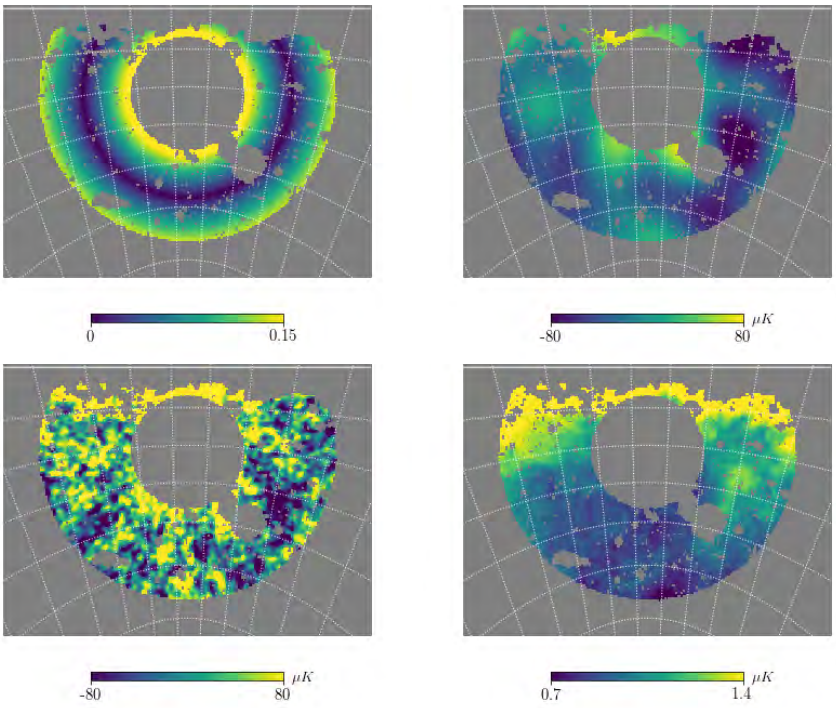


Figure 2.8 Maps of Loop "IIIs" with the *Planck* Common Intensity mask applied. From top left to bottom right: The angular distance from the loop's center; the $\ell \leq 20$ SMICA map; the *Planck* 100 GHz map at 1° resolution; the 408 MHz Haslam map scaled to 100 GHz for comparison.

the percent level: for the unmasked (masked case) I find the $p$-values 0.9139, 0.9542, 0.9502, 0.0392 (0.9262, 0.9493, 0.9549, 0.0414) for mean, variance, skewness, and kurtosis, respectively. The correlation statistic, computed in ±10° bands, amounts to 0.32 (0.31) with corresponding $p$-values 0.9989 (0.9979) and thereby remains unusual. It must, however, be noted that the correlation found in filament III alone is essentially zero. Therefore no increase in significance for the combination IIIs+III was expected; the combined correlation is merely dominated by that within IIIs.

The unusually cold filament IIIs (perhaps including filament III) in the SMICA map could be appearing due to over-subtraction during the attempt to remove foreground contamination in the microwave maps. However, given that the structure can hardly be seen in temperature data as opposed to *WMAP*'s polarization data, it is difficult to imagine that the entire cold structure is seen in the SMICA map solely due to this reason. In fact, *Planck*'s measurement at 100 GHz, where Galactic emission is expected to be minimal in comparison to the CMB, exhibits similarly cold features in this very region leading to a very similar cross-correlation value, see Figure 2.8. A non-exhaustive search for foreground emissions spatially (anti-)correlated with

the low CMB temperature pattern in this region has only resulted in finding the 408 MHz Haslam map to have features approximately aligned with the cold and hotspots in the SMICA map. I show the Haslam map in Figure 2.8 scaled to 100 GHz with a constant spectral index of $\beta = -3$ to enable comparison with the foregrounds at 100 GHz. Should synchrotron emission have been over-subtracted off the SMICA map it therefore can only contribute marginally to the unusually cold regions. One could therefore suspect that the CMB is indeed surprisingly cold along filament IIIs, with no substantial relation to foregrounds. As Vidal et al. report, this region (as most of those identified by the authors) exhibits polarization ratios of around 30% and a strongly aligned magnetic field. The question therefore arises why the CMB should have exceptionally low temperature just along the same filament appearing so well ordered in *WMAP*'s polarization measurement of the low frequency foreground.

## 2.5 Temporary conclusion

In this chapter I reviewed, reanalyzed and eventually supported claims by Liu et al. (2014) about contamination in CMB maps by Galactic structures, namely Galactic Radio Loop I, and extended the analysis to a range of Galactic filaments reported by Vidal et al. (2015). By justifying previously made assumptions about the smoothing scale of the CMB maps, masking the maps, and introducing a new correlation statistic, the results were made more robust (section 2.2.1). I discussed reasons for possible foreground contamination and responded to the interpretations in Planck 2015 results. XXV in sections 2.2.2 and 2.3. In particular I performed calculations on combined sets of filaments, I+Is and XII, to meet the suggestion by Planck 2015 results. XXV that these structures carry the same origin, and still find $p$-values of $\sim 10^{-2}$ (section 2.4.1). While the precise reason for the foreground leakage could not be clarified, residual emission by Galactic Radio Loop I in current CMB maps cannot be dismissed.

In addition to Loop I or its filaments, another prominent structure appeared, the newly proposed structure Filament IIIs (section 2.4.2). The underlying mechanism for the particularly cold temperature along filament IIIs is unknown to date. While physical interactions forming Loop III have been investigated (Kun, 2007), no considerations regarding filament IIIs have been made yet. On the contrary, the existence of a real mechanism along filament IIIs is even questioned by the *Planck* Collaboration (Planck 2015 results. XXV) as to whether it is merely an artefact in the *WMAP* K-band polarization data, since it does not appear as pronounced in *Planck*'s measurements at 30 GHz. (This proposal has to be traded off against the polarization measurements of the C-BASS experiment at 5 GHz (Taylor, 2018) as well as recent claims about systematics present in *Planck*'s 30 GHz map (Weiland et al., 2018).) At the current stage

this coincidence cannot be resolved and therefore, for now, must be added to the list of CMB anomalies. Future measurements (by e.g. the QUIJOTE wide survey (Rubino-Martin et al., 2010; Genova-Santos et al., 2015), the C-BASS experiment (Irfan et al., 2015), and perhaps, by using a large opening angle, the GreenPol experiment (Fuskeland et al.)) might provide new explanations for this phenomenon, perhaps with aid of polarization measurements at low frequencies.

Generally, it is not too far fetched to imagine systematic bias in the removal of foreground emission which could contribute to both the found anomalies. Even for high frequency foregrounds, such as thermal dust emission, inconsistencies in the extracted parameters were pointed out in Liu et al. (2017), and should be presented in the next section. Only if findings as those presented in Liu et al. (2014), and here are taken seriously high-precision measurements of the CMB can be considered accurate.

There is more known contamination present in CMB maps, deposed by e.g. point sources, bright molecular clouds, and errors along the Galactic plane. In cosmological analyses of the CMB maps, the most disturbing regions of the sky are masked out, not to interfere with the results. However, as every measurement is deficient to some degree, applying a mask equates to finding a compromise. It should therefore be of at least equally high priority to understand better the astrophysical foregrounds.

CHAPTER 3

# Evaluation of Planck's foreground separation products

The previous section provided a specific example of potential failure of foreground separation. Given the strong assumptions welded into the algorithms, also unspecific, e.g. not localizable, failures could be thinkable. In the introduction to this thesis I stressed that the final CMB products of the various foreground separation and removal methods are largely consistent, also repeatedly claimed by the makers. While this may seem preferable, given the assumption that there remains some level of contamination, this circumstance does not turn out to be very helpful. In this chapter I will present a look on some of the products of these algorithms, but instead of background maps of the CMB I will investigate the foreground maps produced by one or more such methods.

In the first part, Section 3.1, I will occupy myself with the maps of thermal dust emission produced by the *Planck* collaboration by different methods. I perform comparisons only among maps which depict the thermal dust sky (and parts of the CIB). The findings suggest that additional constraints in the different methods predetermine the outcome of their results. The second part, Section 3.2 focuses on the map of AME, which constitutes a special type of dust emission. Correlations of this map with the accompanying products of *Planck*'s foreground separation results are given using the method of mosaic correlations.

*The content of this chapter is based on Liu et al. (2017) and von Hausegger and Liu (2015).*

## 3.1 Dust and the Cosmic Infrared Background

The *Planck* Collaboration has provided the most precise full-sky measurements of the microwave and millimeter sky to date. The wide frequency coverage of their HFI enables them to tightly constrain thermal dust emission, in temperature as well as in polarization. As was seen in the unfortunate example of the BICEP2 results (Ade et al., 2015b), polarized emission from dust can affect the measurement of the CMB's $B$-modes, if not taken into account properly. Since fitting of the polarized dust signal comes with additional complications, in this section, I shall be concerned with the simpler of the two, the intensity data, and investigate different dust products published by *Planck*, to see whether they agree.

In the optically thin limit, the spectral energy density of thermal dust emission at frequency $\nu$ and in direction $\mathbf{n}$ can be modeled as a so called modified black-body (MBB) (Planck 2013 results. XI):

$$I_\nu(\mathbf{n}) = \tau_0(\mathbf{n}) \left(\frac{\nu}{\nu_0}\right)^{\beta(\mathbf{n})} B_\nu(T_d(\mathbf{n})), \tag{3.1}$$

where $\tau_0$ is the dust optical depth at a reference frequency $\nu_0$, and $\beta$ is the dust spectral index.

$$B_\nu(T_d(\mathbf{n})) = \frac{2h\nu^3}{c^2} \left(e^{\frac{h\nu}{kT_d(\mathbf{n})}} - 1\right)^{-1} \tag{3.2}$$

is the Planck black-body spectrum with dust temperature $T_d$. The assumptions gone into this model are certainly not fully realized by Nature (different dust populations along the line-of sight at potentially different temperatures would require many more modifications than shown); never the less this parameterization has proven itself handy and is commonly in use in Astrophysics.

Also the *Planck* collaboration utilizes this three-parameter model and provides solutions to the thermal dust sky, i.e. maps of each of the three parameters. The fits were performed in essentially each pixel separately, via three slightly different approaches, namely *Planck*'s 2013 full sky model of the first public release (Planck 2013 results. XI) (hereafter P13), *Planck*'s Commander solution from the second data release (Planck 2015 results. X) (hereafter C15), and a CIB-free solution derived in the so called GNILC framework (Remazeilles et al., 2011) also from *Planck*'s second data release (Planck intermediate results. XLVIII) (hereafter P16). Each method produces maps of the three MBB parameters, $\beta$, $\tau_0$, and $T_d$. These maps will be subject to analysis below. The differences of the three methods are listed is table 3.1.

Table 3.1 Differences in the *Planck* thermal dust emission products. The last column indicates whether the CIB was treated separately in the fitting or not.

| Method | *Planck* data | PR | External data | Algorithm | CIB |
|---|---|---|---|---|---|
| P13 | 353 – 857 GHz | PR1 | IRAS 3000 GHz | $\chi^2$ (MPFIT) | ✗ |
| C15 | 30 – 857 GHz | PR2 | *WMAP* (23 – 94 GHz) Haslam (408 MHz) | COMMANDER | ✗ |
| P16 | 353 – 857 GHz | PR2 | IRAS 3000 GHz | GNILC | ✓ |

After a justification of applying a common smoothing to all maps for a fair comparison (3.1.1), I compare the maps in all regions of the sky collectively by measures such as their power spectra, distribution functions, and correlations (3.1.2). Subsequently, I zoom in on two localized regions on the sky, the BICEP zone and a region around the North Celestial Pole (3.1.3), and finally investigate differences in the thermal dust solutions after extrapolating to a lower frequency, where the CMB becomes dominant (3.1.4). Lastly I discuss the findings (3.1.5).

### 3.1.1 Are comparisons among smoothed parameter maps sensible?

The three maps, $\beta(\mathbf{n})$, $T_d(\mathbf{n})$ and $\tau_0(\mathbf{n})$ come at different angular resolutions and smoothings for the different methods which produced them: The C15 maps are smoothed with a 1° Gaussian beam, significantly larger than the 5′ those of P13 and P16 have. In order to make a reliable comparison between the three solutions, their angular smoothing must agree, and corresponding adjustments need to be done. Due to the strong non-linearity of the thermal dust model, Equation 3.1, these adjustments must be done with care. The most natural way would be to degrade all frequency maps which were used in the respective thermal dust fits down to a common angular resolution $\theta$ by applying a Gaussian filter $G\left[(\mathbf{n}-\mathbf{n}')^2/2\theta^2\right]$ and subsequently repeat the parameter fits. Unfortunately, due to the large computational cost the re-running of the parameter fits would require this procedure is hardly feasible and should not be done here. Instead I argue, that the resulting, higher resolution maps of $\tau_0(\mathbf{n})$, $\beta(\mathbf{n})$, and $T_d(\mathbf{n})$ can be smoothed in regions where their variation is small compared to their mean value, leading to

equivalent results. A smoothed intensity map, $I_\nu^\theta(\mathbf{n})$, can be written as follows.

$$I_\nu^\theta(\mathbf{n}) = \int G\left[(\mathbf{n}-\mathbf{n}')^2/2\theta^2\right] I_\nu(\mathbf{n}')\, d\mathbf{n}' = \sum_{\ell m} G_\ell a_{\ell m} Y_{\ell m}(\mathbf{n}), \tag{3.3}$$

where $G_\ell$ is the Gaussian beam in multipole space and $a_{\ell m}$ are the spherical harmonic coefficients of the un-smoothed intensity map $I_\nu(\mathrm{n})$.

Expanding all parameters into mean value (overlines) and spatial variation ($\Delta$), and additionally considering $\Delta\beta(\mathbf{n})/\overline{\beta}$ and $\Delta T_d(\mathbf{n})/\overline{T}_d$ to be small for all $\mathbf{n}$, the intensity of dust emission Equation 3.1 can approximated to first order,

$$\begin{aligned} I_\nu(\mathbf{n}) \approx (\overline{\tau}_0 + \Delta\tau_0(\mathbf{n}))\left(\frac{\nu}{\nu_o}\right)^{\overline{\beta}} B_\nu\left(\overline{T}_d\right) \times \\ \times\left[1 + \Delta\beta(\mathbf{n})\cdot\ln\left(\frac{\nu}{\nu_0}\right) + \left.\frac{d\ln B_\nu}{d\ln T_d}\right|_{\overline{T}_d} \cdot \frac{\Delta T_d(\mathbf{n})}{\overline{T}_d}\right]. \end{aligned} \tag{3.4}$$

Indeed the observed variations $\Delta\beta$ and $\Delta T_d$ turn out to be small enough for this approximation to hold. In contrast, the variation of the optical depth, $\Delta\tau_0$, cannot be considered small compared to $\overline{\tau}$ for all regions of the sky; as shown below, $\tau_0$ spans multiple orders of magnitude. However, for those regions of the sky where $\Delta\tau_0/\tau_0$ *can* be considered small, Equation 3.4 reduces to

$$\begin{aligned} I_\nu(\mathbf{n}) \approx \overline{\tau}_0\left(\frac{\nu}{\nu_o}\right)^{\overline{\beta}} B_\nu\left(\overline{T}_d\right) \times \\ \times\left[1 + \frac{\Delta\tau_0}{\overline{\tau}_0} + \Delta\beta(\mathbf{n})\cdot\ln\left(\frac{\nu}{\nu_0}\right) + \left.\frac{d\ln B_\nu}{d\ln T_d}\right|_{\overline{T}_d} \cdot \frac{\Delta T_d(\mathbf{n})}{\overline{T}_d}\right], \end{aligned} \tag{3.5}$$

and using Equation 3.3 leads to the desired approximate relationship

$$I_\nu^\theta(\tau, \beta, T_d; \mathbf{n}) \approx I_\nu(\tau^\theta, \beta^\theta, T_d^\theta; \mathbf{n}). \tag{3.6}$$

As Gaussian smoothing is applied to a map via a linear operator, cf. Equation 3.3, under the circumstances discussed here, smoothing the dust intensity map as suggested above is equivalent to smoothing the individual parameter maps $\tau(\mathbf{n}), \beta(\mathbf{n})$ and $T_d(\mathbf{n})$ in hindsight.

### 3.1.2 Full-sky comparison

The smoothing angle I applied to all maps for a fair comparison corresponds to a FWHM of 2°. In Figure 3.1 I show maps of all parameters for all three thermal dust fits. Even by naked eye

it is noticeable that both the spectral index and the temperature maps have strong differences, despite their similar mean values. The maps of the optical depth, however, appear very similar (although the presentation on the log scale might be influence one's perception).

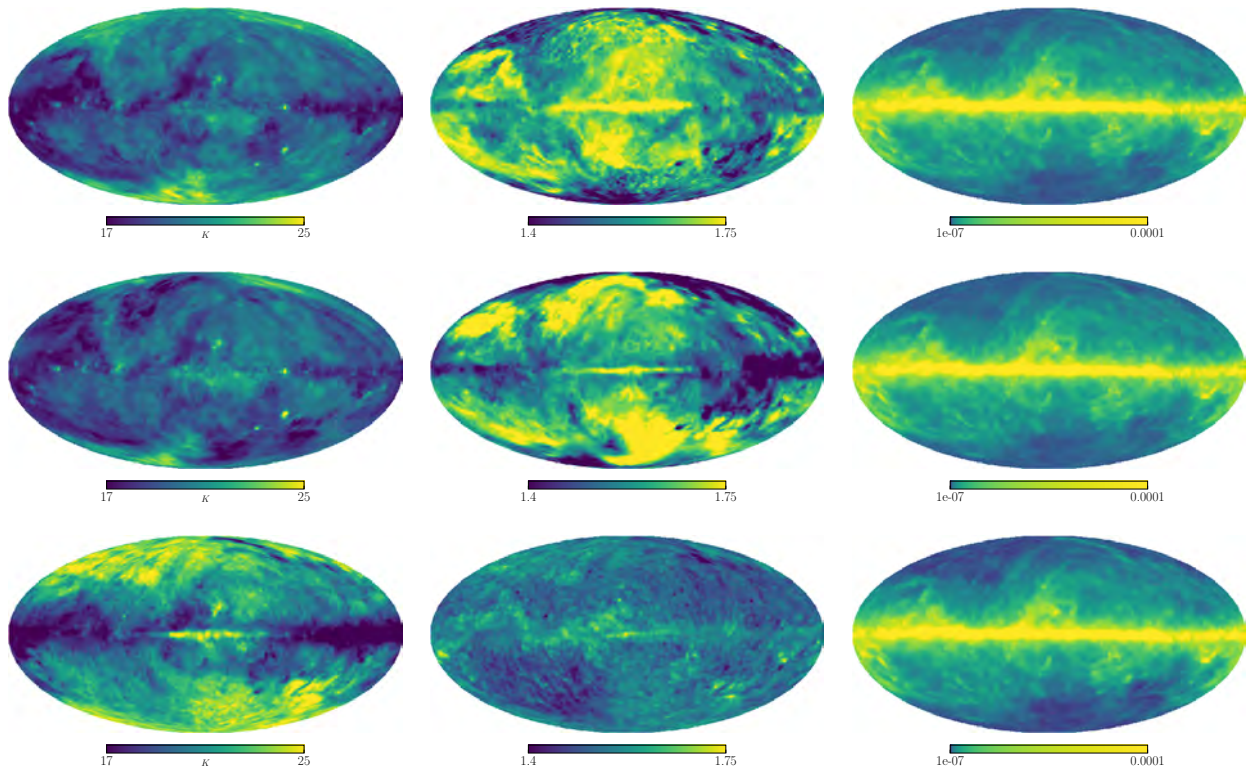


Figure 3.1 The thermal dust emission parameter maps for $T_d$, $\beta$, and $\tau_{353}$ (*from left to right*), given by P13, P16, and C15 (*from top to bottom*). Note, that the optical depth of C15 is provided at a reference frequency of 545 GHz, to allow for comparison I rescale it down to 353 GHz given the corresponding map of the spectral index.

These differences may also be analyzed by computing power spectra of the maps. To this end, the following decomposition of the respective parameter maps into spherical harmonics $Y_{\ell m}(\mathbf{n})$ can be made:

$$\begin{Bmatrix} \tau(\mathbf{n}) \\ \beta(\mathbf{n}) \\ T_d(\mathbf{n}) \end{Bmatrix} = \sum_{\ell=0}^{\infty} \sum_{m=-\ell}^{\ell} \begin{Bmatrix} \tau_{\ell m} \\ \beta_{\ell m} \\ T_{d,\ell m} \end{Bmatrix} Y_{\ell m}(\mathbf{n}) \tag{3.7}$$

where $\tau_{\ell m}, \beta_{\ell m}, T_{d,\ell m}$ are the corresponding harmonic coefficients. The scaled power spectrum

Table 3.2 Monopoles and standard deviations for the various full-sky parameter maps

| Method | | $T_d$ [$K$] | $\beta$ | $\tau_{353}$ |
|---|---|---|---|---|
| P13 | mean | 19.7 | 1.61 | $1.97 \cdot 10^{-5}$ |
| | std. | 1.34 | 0.09 | $5.14 \cdot 10^{-5}$ |
| P16 | mean | 19.4 | 1.60 | $1.89 \cdot 10^{-5}$ |
| | std. | 1.15 | 0.12 | $4.85 \cdot 10^{-5}$ |
| C15 | mean | 20.9 | 1.54 | $1.86 \cdot 10^{-5}$ |
| | std. | 2.08 | 0.04 | $4.41 \cdot 10^{-5}$ |

$\mathcal{D}_\ell^{XX}$ for each of the parameters $X$ reads:

$$\mathcal{D}_\ell^{XX} = \frac{\ell(\ell+1)}{2\pi(2\ell+1)} \sum_{m=-\ell}^{\ell} |X_{\ell m}|^2 \tag{3.8}$$

The monopoles for the respective parameters are comparable and a look at the standard deviations supports the above remark concerning small spatial variation $\Delta\beta$ and $\Delta T_d$, cf. Table 3.2.

In Figure 3.2 I show the full sky power spectra for all three parameters. While the respective monopoles hardly differ, the multipole dependences of the different $\mathcal{D}_\ell^{XX}$ reveal a significant mismatch, especially distinct for the spectral index. In comparison to P13 and P16, the C15 solution is characterized by a lower and flatter power spectrum for the spectral index $\beta$ at low multipoles, $\ell \lesssim 70$, where $\mathcal{D}_\ell \approx const.$ This seems to be compensated by more power in the temperature map on all scales. This trade-off could already be seen in the sky map of Figure 3.1 and will be mentioned below again in the context of parameter degeneracies. The optical depth experiences a loss of power towards higher $\ell$ at around $\ell \gtrsim 40$, and here the map of C15 carries consistently less power than both P13 and P16. Needless to say, all the maps presented in Figure 3.2 reveal significant statistical anisotropy, clearly seen in the even/odd parity asymmetry of the power spectra (the amplitude of $\mathcal{D}_\ell$ for even $\ell$ is systematically greater than for odd multipoles), most pronounced in the power spectrum of the optical depth, due to the concentration of the signal along the Galactic plane. There, despite its overall lower power, this asymmetry appears strongest in the C15 solution.

To get an idea of which values are taken across the full sky, Figure 3.3 shows empirical distribution functions (EDF) of the respective parameter values. The distributions are normalized to the total number of pixels in the maps.[1] It appears that the C15 distributions for $T_d$ and

[1] A similar comparison was also presented in figure 11 of Planck intermediate results. XLVIII. However, they omitted to compare the parameter maps at a common resolution. That smoothing has a great effect on the

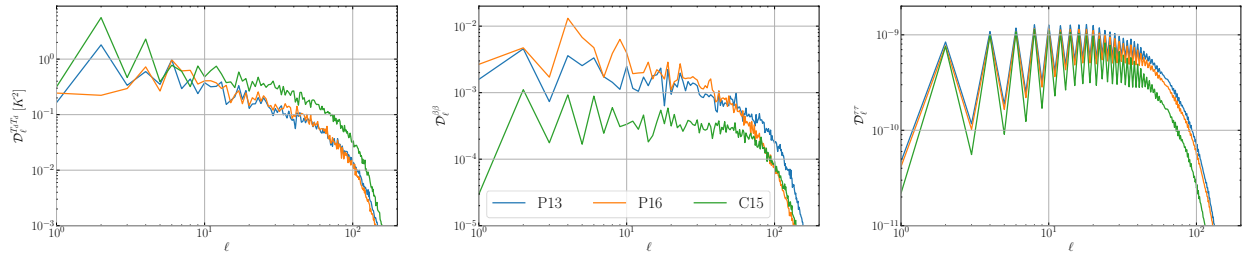


Figure 3.2 The power spectra, $\mathcal{D}_\ell^{XX}$, as defined in Equation 3.8, for $T_d$ (*left*), $\beta$ (*middle*), and $\tau_{353}$ (*right*) computed from the P13, P16, and C15 parameter maps. The cut-off at $\ell \gtrsim 50$ corresponds to the 2° Gaussian smoothing.

$\beta$ follow Gaussians. For comparison I plot the priors reported for the algorithm, whose amplitudes were chosen by hand in an attempt to match the distributions. The Gaussian priors in C15 are $\mathcal{P}(\beta^{C15}) = \mathcal{N}(1.55, 0.1)$ and $\mathcal{P}(T^{C15}) = \mathcal{N}(23, 3)$; $\tau$ is calculated from a combination of the previous parameters and the dust amplitude, a parameter constrained only to be positive. Note that in P13 the allowed ranges of variation are $1.0 \leq \beta^{P13} \leq 2.5$ and $10 \leq T^{P13} \leq 60$ K, i.e. approximately flat priors. In spite of different treatment regarding the CIB, the temperature and optical depth distributions of P13 and P16 look very similar. Only the distributions of the spectral index exhibit a discrepancy at $\beta \simeq 1.7$; it stands to reason that this difference is likely caused by the CIB.

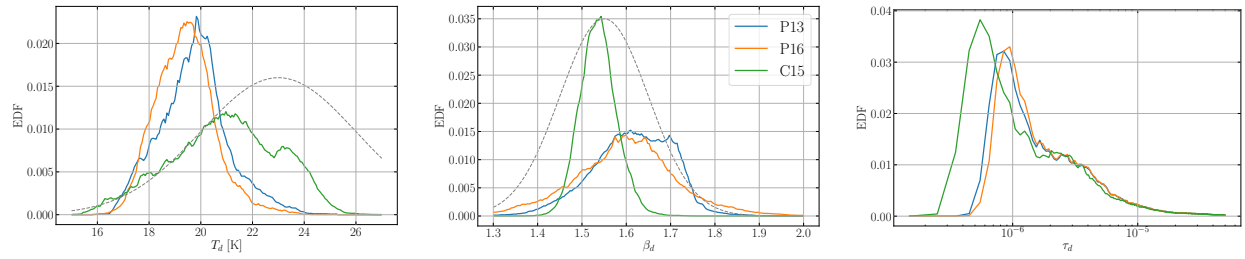


Figure 3.3 The distribution functions for $T_d$, $\beta$, and $\tau_{353}$ (*from left to right*), given by P13 (black), P16 (blue) and C15 (red) for the full sky maps. For comparison the C15 priors are plotted in gray dashed lines.

Finally, full-sky cross-correlations between $T_d$ and $\beta$ as well as $T_d$ and $\tau$, are shown for each of the solutions, see Figure 3.4 and Table 3.3. The negative correlation between $T_d$ and $\beta$ is a well known feature of the chosen model, Equation 3.1, and was discussed in P13 and is also reproduced by P16. It was noticed that noise and also the CIB contribute to this negative correlation, although at a smaller level than present in the data (Planck 2013 results. XI).

distributions of the parameters was shown by, e.g. Planck 2013 results. XI (figure 6).

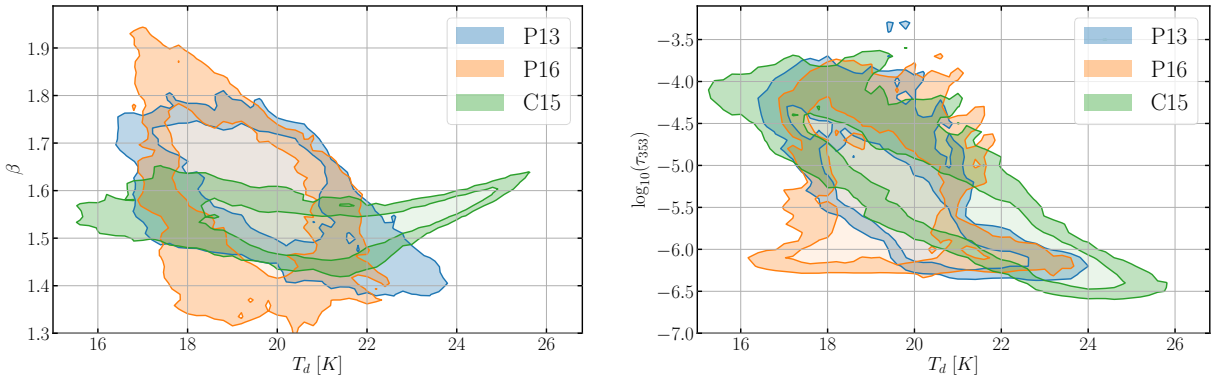


Figure 3.4 T-T plots for $\beta$ vs. $T_d$ (*left*), and for $\log_{10}(\tau_{353})$ versus $T_d$ (*right*). The solid contours correspond to 1 and 2 $\sigma$ standard deviations of the 2-dimensional distributions of the points.

Table 3.3 Correlation values for the T-T plots of Figure 3.4

| Method | $T_d \times \log\tau$ | $T_d \times \beta$ | |
|---|---|---|---|
| P13 | mean | −0.69 | −0.58 |
| P16 | mean | −0.80 | +0.01 |
| C15 | mean | −0.09 | −0.53 |

Also from the P13 and P16 maps in Figure 3.1 one finds that for most regions of the sky lower temperature regions are accompanied by higher spectral index regions and vice versa. While the C15 solution at low temperatures shows negative correlation as well — yet less pronounced — it turns to become strongly positive at temperatures $T_d \gtrsim 21\,K$. Again referring to Figure 3.1, the regions in which dust temperatures this high occur, happen to lie at higher Galactic latitudes $|b| \gtrsim 50°$, those regions where the CIB begins to dominate. The negative correlation between $T_d$ and $\tau$ present for the P13 solution, is well reproduced by C15, marginally however for P16.

### 3.1.3 Focusing on selected regions

Two regions are of immediate interest when it comes to questioning the consistency of thermal dust models. The first is the BICEP zone in the southern hemisphere. The BICEP collaboration, since only measuring at two frequencies (95 and 150 GHz), relies on the foreground predictions of other experiments with wider frequency coverage, such as those from the *Planck* experiment. As seen above, the predictions must be used with care and systematic differences in the solutions must be taken into account. The second region is of personal interest of my

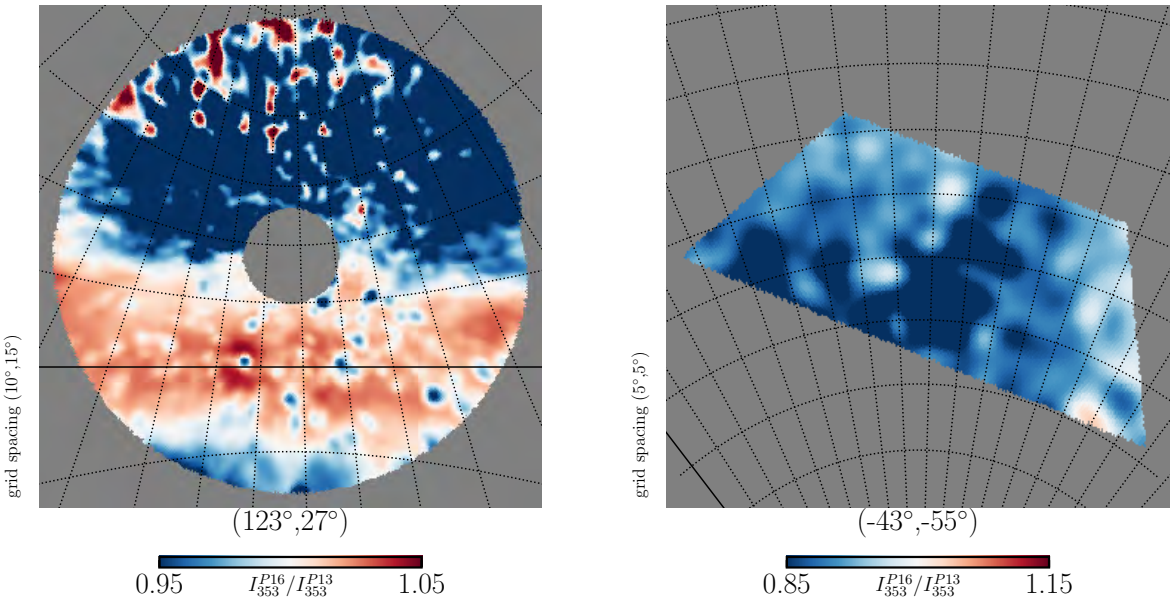


Figure 3.5 The ratio $I_{353}^{P16}/I_{353}^{P13}$ of the dust intensities given by P16 and P13 evaluated at 353 GHz. The sky regions shown are a possible observation region around the NCP by the GreenPol experiment (*left*) and the BICEP zone (*right*).

group, a zone around the North Celestial Pole (NCP) accessible via the GreenPol experiment.[2] As an appetizer I show the ratio of the P13 and P16 dust solutions at 353 GHz in those two regions, in Figure 3.5. While the GreenPol region shows areas of both, over- and underestimation of the P16 thermal dust solution with respect to that of P13, it completely undershoots the P16 solution in essentially all of the BICEP region.

To see how this difference comes about in terms of the dust parameters, repeating some of the results shown above for the two regions separately is useful. I show the distributions of the dust parameters and the T-T plots/correlations in Figures 3.6 and 3.7.

Since the P16 solution should depict the dust emission only (without the contribution of the CIB) finding less signal at high Galactic latitudes, as the case for the BICEP region, was expected. What was not expected is the large difference in the P13 and C15 solutions.

[2]The specifications of the measurement setup have not been determined to date and the future observation of different sky fractions/regions is possible. In Section 5, I will present results for another 'GreenPol region'. For the present treatment, however, the specific region does not matter much.

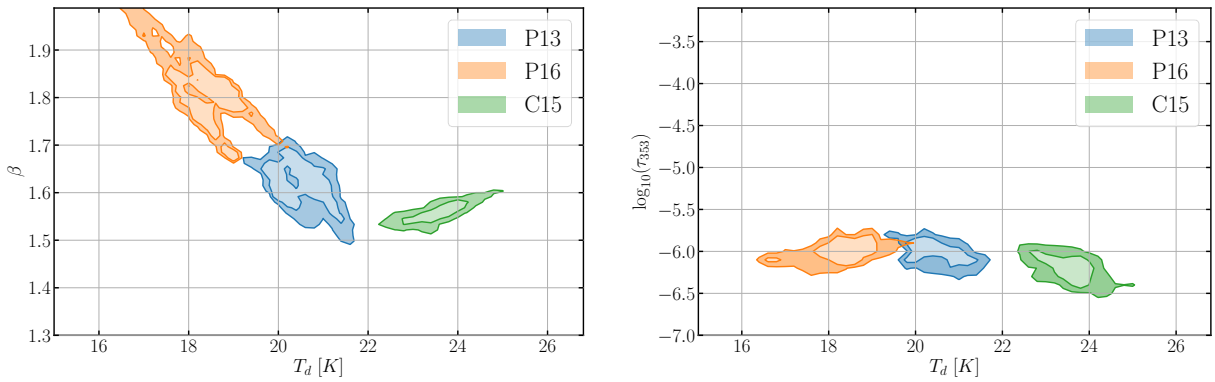


Figure 3.6 Same as Figure 3.4 but for the BICEP region.

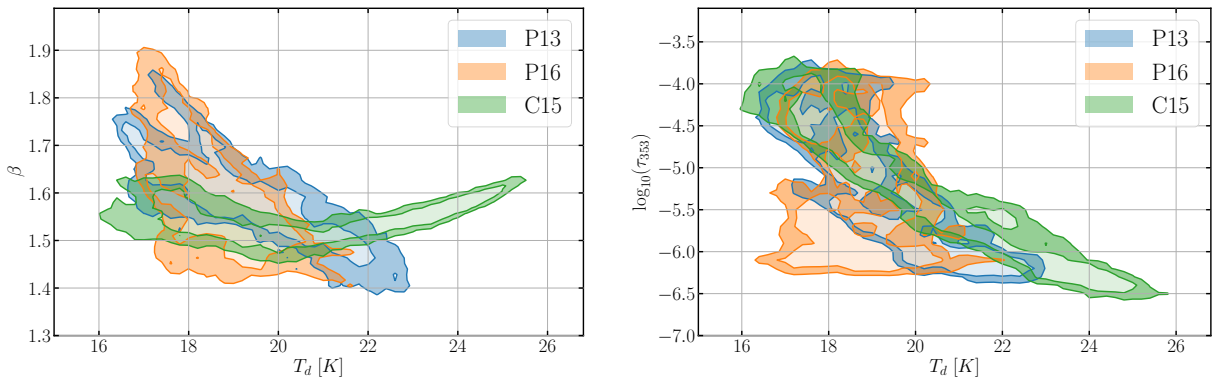


Figure 3.7 Same as Figure 3.6 but for the GreenPol region.

### 3.1.4 Extrapolating to CMB frequencies

To make a brief connection to CMB recovery I construct full-sky maps of thermal dust emission using the parameter sets of the three methods considered, and extrapolate them to 80 GHz, as an example of a frequency where the CMB dominates the foregrounds. Even though the estimates of the respective parameters might be biased by the CIB, once fitted they should ensure reliable extrapolation of the full dust emission's intensity to at least the frequencies relevant for CMB analyses. Comparison of the different thermal dust skies then serves as a measure of the systematic uncertainties affecting the CMB map. (Here "systematic" refers to the data treatment, or, in this case, the way one chooses to fit the emission by Galactic dust.)

The differences of the three solutions lie in the range of $\pm 5\mu$K, or even higher along the Galactic plane, which is about the same level as their statistical uncertainties! (It should be obvious that the large-scale differences seen in Figure 3.8 do not result from these statistical uncertainties, as clear systematic trends are observed.) All solutions appear to have about the same level of differences at high Galactic latitudes, where the CIB should gain influence in the fits. At higher frequencies it is the P16–C15 map which carries the lowest difference amplitudes at high Galactic latitudes.

### 3.1.5 Discussion

Despite the supposed understanding of dust foregrounds in temperature, the three solutions by *Planck* investigated here do not appear consistent as qualitatively shown via maps, Figure 3.1, their power spectra, Figure 3.2, or their distribution functions 3.3. Quantitative differences were shown in Table 3.2 and by calculating differences of these solutions at a characteristic CMB frequency, $\nu = 80$ GHz. While at first I was concerned with the full sky, in the following I also focused on two example regions of the sky, which both claim to be among the cleanest regions of our sky.[3] Of particular interest was the degree to which correlations among the different parameter maps are distinct for the three different fitting techniques.

The negative correlation between dust temperature and the dust optical depth, as shown in the right panel of Figure 3.4, is most pronounced for the C15 solution, the one containing the least amount of high frequency information (or which may be biased more towards lower frequencies). This can be understood from viewing the dust model, Equation 3.1, in its

[3] While they still be among the cleanest regions, it is the current understanding of foreground emission in these regions which may need some cleaning.

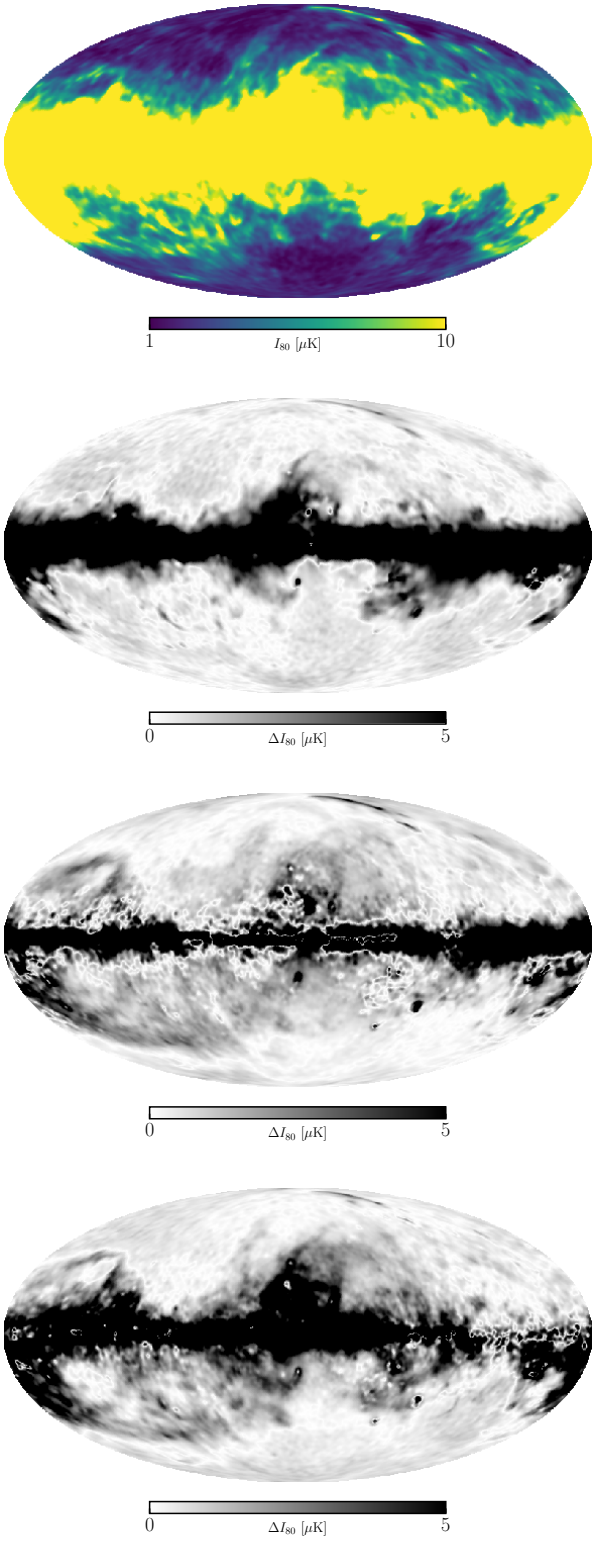


Figure 3.8 Extrapolated dust temperatures to 80 GHz and absolute values of the differences of the different solutions. *From top to bottom:* The P13 solution, The differences P13–P16, P16–C15, and C15–P13.

Rayleigh-Jeans limit, $h\nu \ll k_B T_d(\mathbf{n})$, but expanded up to second order:

$$I_\nu^{\mathrm{R}J}(\mathbf{n}) \propto \tau_0(\mathbf{n}) T_d(\mathbf{n}) \nu^{2+\beta(\mathbf{n})} \left(1 - \frac{h\nu}{2k_B T_d(\mathbf{n})}\right). \tag{3.9}$$

At first order the degeneracy between $\tau_0$ and $T_d$ is inevitable, and is only broken at second order. In other words, high frequency measurements are key to determining these two quantities better. And, indeed, P16 which includes higher frequency measurements, does not exhibit as strong of a negative correlation. P13, however, shows a similarly negative correlation as C15. Even though Planck 2013 results. XI showed that the CIB has negligible influence on the parameter degeneracies, this results may contradict — it seems possible that the separate CIB treatment in 16 avoids strong anti-correlation in $\tau_0$ and $T_d$.

Regarding the left panel of Figure 3.4, the term exhibiting the degeneracy between dust temperature and spectral index (or its spatial variation) becomes clear from expanding $\beta(\mathbf{n}) = \overline{\beta} + \Delta\beta(\mathbf{n})$ around $\Delta\beta \ll 1$. Then Equation 3.9 contains a term

$$I_\nu^{\mathrm{R}J}(\mathbf{n}) \propto \tau_0(\mathbf{n}) T_d(\mathbf{n}) \Delta\beta(\mathbf{n}). \tag{3.10}$$

Also here, out of the same reason as above, one finds the degeneracy to be broken at second order in $h\nu/k_B T_d$, or with inclusion of higher frequencies.

For the CMB scientist having a fully physical model of thermal dust emission is certainly of secondary rank. The purpose of this effective modeling of dust emission as a MBB is keeping the balance between a low number of free parameters and high degree of foreground capture for the recovery of a clean CMB map. I do not address potential problems of biasing the CMB recovery by the choice of an unphysical, yet effective, model here. However, I assume, that using a model which already in temperature measurements gives large discrepancies when essentially jackknifing the input data, poses correspondingly bigger problems for the capture of thermal dust polarization where also other effects such as line-of-sight integration of polarized emission or depolarization come into play. Especially considering the presence of more exotic dust components, as are dubbed Anomalous Microwave Emission, or AME, such effective treatment becomes increasingly dangerous.

## 3.2 Anomalous Microwave Emission

*Planck*'s COMMANDER algorithm is the most lengthy component separation method presently in use. In Planck 2015 results. X the *Planck* Collaboration applied it to their data of PR2 and therewith presented an array of foreground products including maps of just discussed synchrotron, free-free, thermal dust, as well as Anomalous Microwave Emission. As mentioned above, these maps are valid decompositions of the sky only under the specific assumptions made; nevertheless, it is interesting to test their validity via internal cross checks or additionally, with external data. Most attention should be, of course, given to the newest and least understood component, AME.

The Collaboration itself, presented a first correlation analysis of their AME map with potential tracers of the anomalous dust grains (Planck 2015 results. XXV). After masking out point sources and regions with low signal-to-noise ratio, they find significant linear correlation with tracers of dust emission (up to some curvature reportedly introduced by dust temperature variations), as is expected for spinning or magnetic dust models. They also investigate correlations with HI and CO emission (a tracer for HII emission). Even though the linear relationship between each of these quantities is still established by the statistic, there is noticeably more scattering in the plots. I will return to this circumstance shortly. First, it is important to mention the work by Hensley et al. (2016) in which the authors extend the correlation analysis begun by the *Planck* Collaboration to include tracers of polycyclic aromatic hydrocarbons (PAHs) — up until that date, the prime candidates for spinning dust grains (cf. Section 1.2.2; see, however Hensley and Draine (2017)). Their results surprisingly disfavor spinning PAHs explaining the AME but not only those: as the PAH tracers trace not only abundance of PAHs in specific but of *all* very small dust grains, the spinning dust hypotheses in general seems to be in conflict with *Planck*'s AME product.

In this light it seemed important to establish the correlations the map of AME has with the other COMMANDER products, specifically addressing the scattering problem mentioned above — deviations from the linear correlation in their full-sky T-T plots cannot be assigned to specific regions on the sky, though potentially arising from those very regions only. I therefore compute correlations in patches distributed over the sky, rather than finding solely a full-sky average — due to its tiled design, this type of correlation will be referred to as "mosaic correlation". (see also Verkhodanov et al. (2009))

Section 3.2.1 introduces mosaic correlations and applies them to foreground maps. Thereafter, in Section 3.2.2 the correlations are weighted by the statistical uncertainties in the maps to obtain more reliable estimates. I end this short section with discussing the results in Section 3.2.3.

### 3.2.1 Mosaic Correlation

The goal of this section is to introduce a way to investigate correlations of maps taking into account the possibility for spatial variation of the maps' statistical properties. Hereto, Pearson's cross correlation coefficient, $K$, is computed from maps $S_1(p)$ and $S_2(p)$ at HEALPix resolution $2^N$ for all pixels $p$ within a region $\Omega$, defined by a grid of resolution $2^M$ with $M < N$, see Equation 3.11. Picking a different combination of values for $N$ and $M$, leads to a different total number of pixels, $N_\Omega$, contributing to one correlation coefficient. In this way, correlations can be probed on different scales, as to be seen below.

$$K_\Omega = \frac{\mathrm{Cov}_\Omega(S_1, S_2)}{\sqrt{\mathrm{Cov}_\Omega(S_1, S_1) \cdot \mathrm{Cov}_\Omega(S_2, S_2)}} \tag{3.11}$$

$$\mathrm{Cov}_\Omega(S_i, S_j) = \frac{1}{N_\Omega - 1} \sum_{p \in \Omega} \left(S_i(p) - \langle S_i(p) \rangle_\Omega\right) \left(\left(S_j(p) - \langle S_j(p) \rangle_\Omega\right) \tag{3.12}$$

Both, the Planck 2015 results. X as well as Hensley et al. (2016) combine the two AME maps, as recommended in Planck 2015 results. XXV, to a single map, which they evaluate at 22.8 GHz. Even though the Collaboration stresses that the two maps do not each represent physically meaningful components, I argue that neither the combination of the two does so. In this analysis I therefore also investigate the two AME maps separately (from here on referred to as AME1 and AME2), each evaluated at their nominal frequency of 22.8 and 41.0 GHz, respectively.

The Commander maps come at resolution $N_{\mathrm{Side}} = 256$ (corresponding to $N = 8$). Choosing, e.g., $M = 4$ leads to a correlation map, the $K$-map, of resolution $N_{\mathrm{Side}} = 16$ with $N_\Omega = 256$ pixels contributing to one correlation coefficient and thereby one pixel on the $K$-map. For this choice of resolution, Figure 3.9 shows the $K$-maps obtained for correlating the maps of AME1 (top row) and AME2 (bottom row) respectively with those of synchrotron, free-free[4] and thermal dust emission. For completeness, the K-maps computed from the composite AME map are shown as well, to demonstrate that the qualitative result remains unchanged.

[4]Since morphologically only marginally different, I use the $EM$ (emission measure) map for free-free emission instead of the temperature of the emission for the correlations. This will prove to be much easier to handle when later considering the error maps of the components.

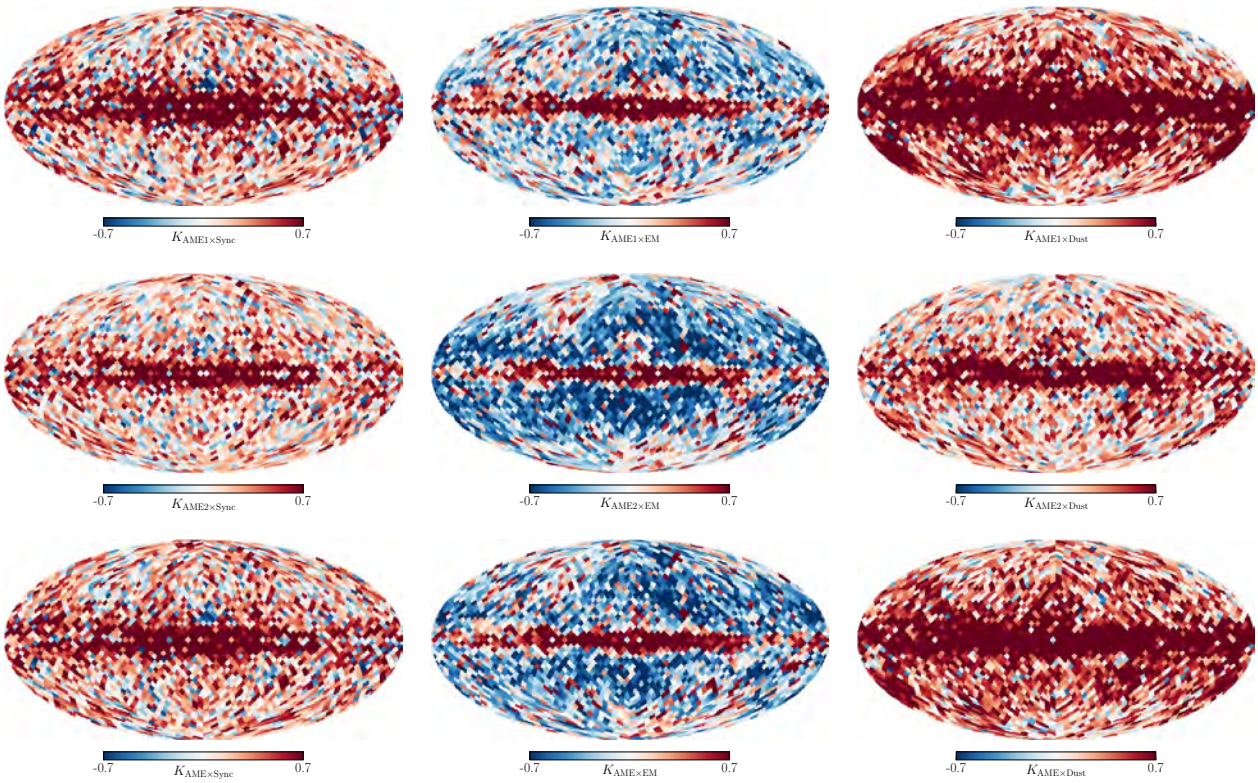


Figure 3.9 *Top panels:* $K$-maps of AME1 with synchrotron radiation (*left*), AME1 with free-free emission (*middle*) and AME1 with thermal dust emission (*right*). *Middle panels:* Same as top, but with AME2 instead of AME1. *Bottom row:* Same as top, but with the composite AME map as prescribed by the *Planck* Collaboration instead of AME1. All $K$-maps are at resolution $N_{\mathrm{Side}} = 16$.

All maps show strong correlations along the Galactic plane, as expected beforehand. Also the mainly positive correlation of the AME with thermal dust emission was anticipated and briefly discussed above. The correlations with synchrotron radiation away from the Galactic plane are less pronounced though still predominantly positive. I interpret the tendency towards positive values as the common relation of both the AME and the synchrotron radiation to the Galactic magnetic field.

Surprising, however, is the strong negative correlation with the COMMANDER map of free-free emission (for histograms of these correlations values also see Figure A.1). Free-free emission by nature occurs in regions of gaseous environment, but so does dust emission. A negative correlation between free-free emission and AME implies that the dust grains emitting the anomalous radiation are located in distinctly different regions, than the plasma causing free-free emission (or at least radiate in different regions, respectively). However, there is a second viable possibility, namely that the component separation algorithm has produced maps, which systematically misstate realilty. In order not to draw too quick conclusions, one should first consider statistical fluctuations.

### 3.2.2 Weighted Mosaic Correlation

I repeat the above analysis, now taking into account the errormaps, $\sigma_i(p)$, provided by COMMANDER. For this purpose I define weights, $w_i(p)$, in Equation 3.13, which emphasize regions of high signal-to-noise ratio over those with large uncertainty.

$$w_i \equiv \left[1 + \left(\frac{\sigma_i(p)}{S_i(p)}\right)^n\right]^{-1} \quad , \qquad n = 1, 2, \ldots \tag{3.13}$$

Different weights are obtained for different choices of $n$: A higher value of $n$ produces weights favoring pixels with a signal-to-noise ratio > 1 and suppressing those with SNR< 1. Figure 3.10 shows the weights (for a choice of $n = 2$)[5] of all COMMANDER component maps. It is clear (mind the color bar) that the application of weights essentially only has an effect for combinations of the AME and free-free emission maps — precisely the correlations of interest. I therefore will not dwell on the correlations with synchrotron radiation and thermal dust emission anymore.

The weights are now included in the definition of the correlation coefficient, Equation 3.11,

[5] The conclusions hold also for other choices of $n$.

by replacing $\mathrm{Cov}_\Omega(S_i, S_j)$ with $\mathrm{Cov}_\Omega(S_i, w_i, S_j, w_j)$:

$$\mathrm{Cov}_\Omega(S_i, w_i, S_j, w_j) = f_\Omega(w_i, w_j) \cdot \sum_{p\in\Omega} \sqrt{w_i(p) w_j(p)}\,(S_i(p) - \langle S_i(p)\rangle_{p\in\Omega})\,((S_j(p) - \langle S_j(p)\rangle_{p\in\Omega})\,, \tag{3.14}$$

where $\langle S_i(p)\rangle_{p\in\Omega}$ now is replaced by the weighted average $\sum_{p\in\Omega} w_i(p) S_i(p) / \sum_{p\in\Omega} w_i(p)$. where the factor $f$ was defined as

$$f_\Omega(w_i, w_j) = \frac{\sum_{p\in\Omega} \sqrt{w_i(p) w_j(p)}}{\left(\sum_{p\in\Omega} \sqrt{w_i(p) w_j(p)}\right)^2 - \sum_{p\in\Omega} w_i(p) w_j(p)}. \tag{3.15}$$

Note that, if $w_i(p) = w_j(p) = 1,\ \forall p \in \Omega$ the covariance reduces to its previous form. In particular, $f(\Omega, w_i, w_j)$ reduces to $1/(N_\Omega - 1)$. Due to the normalization, $f$, the preference of certain pixels over others (by assigned an weight) only takes effect within one patch. In other words, patches including solely pixels with low weights do not pale in comparison to high weight patches.

Even after including the weights, the pronounced negative correlations in the AME-free-free K-maps hardly change on medium latitudes, see Figure 3.11 (and corresponding histograms in Figure A.2). If the unexpected negative correlation between the AME maps and free-free in fact is a result of a flawed component separation, this corresponds to the presence of systematic biases in the method, not statistical uncertainties. These might have established themselves in mainly the maps of free-free emission and AME2, noticeable in the uncertainties at medium and especially high Galactic latitudes. The spectral template of free-free emission might have picked up non-free-free emission on medium to high latitudes which happens to be morphologically distinct from the emission picked up by the AME templates or vice versa. A more thorough investigation of the reliability of Commander's free-free map might clear up this issue.

### 3.2.3 Discussion

Concrete physical implications of this potential inharmoniousness are still unclear at this point. Rather than clarifying this problem to satisfaction, it seemed important to, as a first step, complement the correlation analysis done previously on the full sky by more local estimators of similarity, such that Galactic structures could be identified on different scales. Here, I only

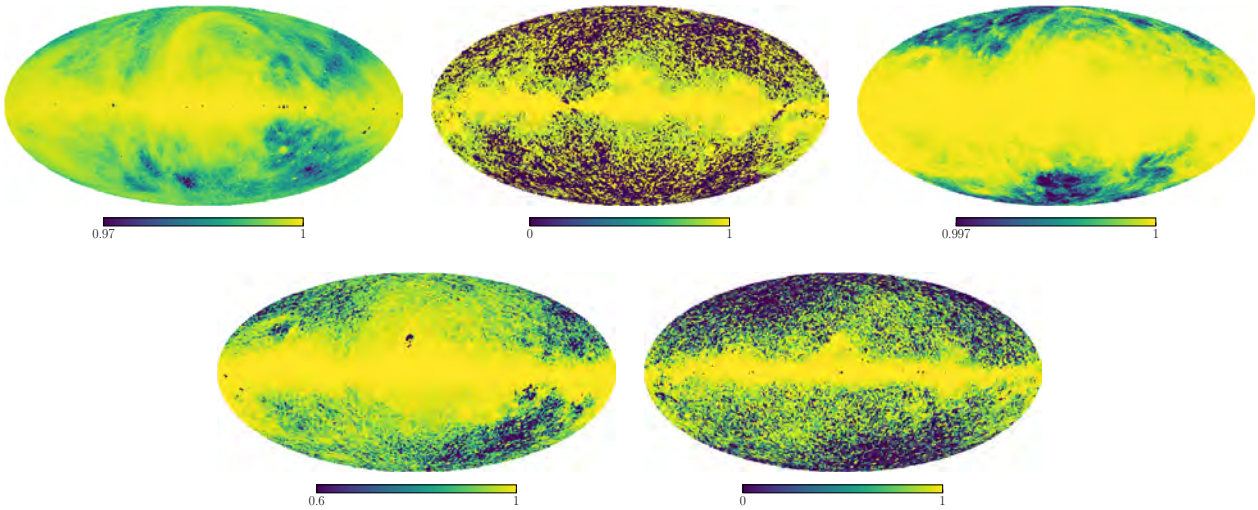


Figure 3.10 *Upper panels:* Weights for synchrotron (*left*), free-free (*middle*) and thermal dust emission (*right*). *Bottom panels:* Weights for AME1 (*left*) and AME2 (*right*). The weights were computed with $n = 2$.

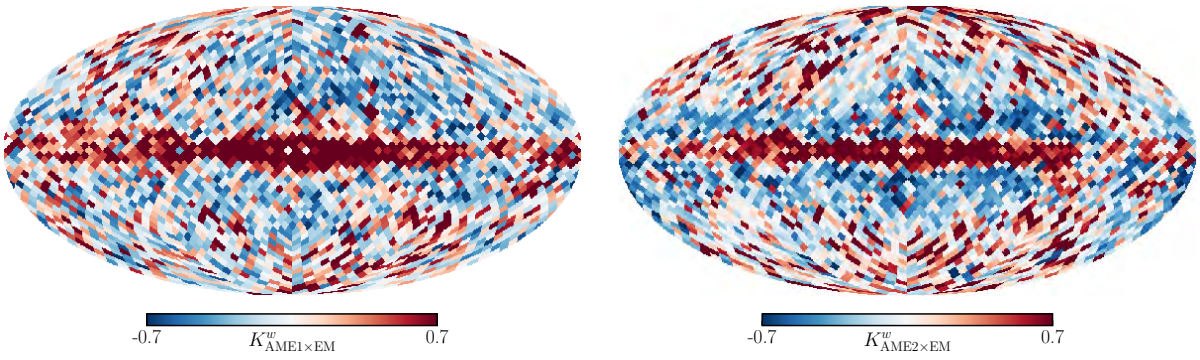


Figure 3.11 Weighted K-maps. AME1 with free-free emission (*left panel*) and AME2 with free-free emission (*right panel*). The correlation coefficient and weights were defined according to Equations 3.14 - 3.15 with $n = 2$.

briefly highlighted key points of the analysis, while details might become more important with future work and/or understanding of the AME. As both, free-free emission and AME, are present at low frequencies, additional measurements at these frequencies will hopefully shed light on this matter, especially by complementing current data with more information about the polarization of the emitted light. With more available frequency channels less compromises in the spectral fits will have to be made, such that more elaborate models will be able to be tested. Still, due to mentioned possibility of biases, the choice of these models will have to be made wisely.

CHAPTER 4

# Statistics of foreground maps

As presented in the introduction, Section 1.1.5, foreground removal techniques for CMB analyses make specific assumptions about the properties of foregrounds in temperature and in polarization. In this chapter I argue that, by investigating the statistics of foreground components more understanding about the degree to which these assumptions are valid can be obtained. To this purpose, a novel method is proposed for analyzing a data set in terms of skewness and kurtosis in locally defined regions that collectively cover the entire sky. It is found that skewness and kurtosis should be evaluated in combination to reveal local physical information. The method is applied to temperature maps only and finally extended also to polarization maps.

At first, in Section 4.1, I present arguments to how the assumptions in foreground removal techniques involve the foregrounds' statistics. This motivates not only general statistical investigations of foreground maps, but also explains the particular approach presented in this chapter. Subsequently, the method is introduced (Section 4.2) and applied (Section 4.3) to different maps for illustration and comparison. One of these maps is a map of synchrotron emission at 408 MHz, and serves as an example of a foreground intensity map. After discussing these results in Section 4.4, synchrotron polarization, and also dust polarization maps are also investigated and their correlations highlighted, using the method of mosaic correlations presented in the previous chapter (Section 4.5). I close with discussing the results and concluding on this topic in Section 4.6.

The investigation of foregrounds' statistics became more popular only recently, after the publication of our first work. In particular, the importance also for 21 cm cosmology has been brought forward and corresponding studies have been initiated (Rana et al., 2018). In addition, reference was made to primordial non-Gaussianity in the CMB (Jung et al., 2018; Hill, 2018): Residual foregrounds might be expected to carry the same statistics as the original foreground

maps themselves — finding non-Gaussian signal in a CMB map, which is similar in appearance to the non-Gaussian foreground signal, therefore might raise doubt about its primordial origin. In the work I present here, however, no specific assumptions are made and this method is just one example of a general approach, which can be extended to specific questions if wished so. In line with this, I would like to emphasize that the term *non-Gaussianity* should *not* be understood as a reference to *primordial* distortions to an otherwise Gaussian distribution, but rather stand, as well, for general departures from a Gaussian expectation, in the CMB, or in foreground maps.

*The content of this chapter is based on Ben-David et al. (2015b) and von Hausegger et al. (2018).*

## 4.1 Motivation

To illustrate the necessity of studying the statistics of foregrounds, I provide the following motivation. I hereto refer back to the ILC method from Section 1.1.5. As mentioned there, this method comes with a list of caveats. I shall elaborate on them here and print the two most important equations here again, for convenience:

The weighted sum

$$\mathcal{S}(p) = \sum_\nu w_\nu S_\nu(p) = M(p) + \sum_\nu w_\nu F_\nu(p), \tag{4.1}$$

and its variance

$$\langle \mathcal{S}^2 \rangle_\Omega = \langle M^2 \rangle_\Omega + 2 \sum_\nu \langle M\, F_\nu \rangle_\Omega\, w_\nu + \sum_{\nu\mu} \langle F_\nu\, F_\mu \rangle_\Omega\, w_\nu w_\mu. \tag{4.2}$$

To understand the construction of the ILC method I first consider the simplified case in which one can express the foreground term as

$$F_\nu(p) = \alpha_\nu F(p), \tag{4.3}$$

where $\alpha_\nu = const.$ and scales the template $F(p)$ along frequencies. In the case of a foreground with power-law emission, $\alpha_\nu = (\nu/\nu_0)^\beta$, the spectral index $\beta = const.$ across the entire region $\Omega$.

From Equation (4.1) it can be seen that the CMB is solved for by computing the weights as

$$\sum_{\nu} \alpha_\nu w_\nu = 0, \tag{4.4}$$

which at the same time[1] minimizes the variance, Equation (4.2). This even generalizes to the case where $F$ describes the superposition of $n$ foregrounds, each scaled similarly to Equation (4.3). Such a system is fully determined for observations at $n+1$ frequencies, or more.

In reality, and for reasons mentioned in Chapter 1, Galactic foregrounds do not follow Equation (4.3) perfectly, i.e. $\alpha_\nu$ is promoted to be direction dependent, or $\alpha_\nu = \alpha_\nu(p)$. In terms of a power-law foreground, this translates into a spatially varying spectral index.[2] The minimization of Equation (4.2) then results in $w_\nu$ such that there are pixels, $p$, for which $\sum_\nu w_\nu F_\nu(p) = 0$ does not hold. In other words, residual emission in the final CMB product becomes inevitable with this method. I expand on this point and consider the factor $\alpha_\nu \to \alpha_\nu(1+\Delta_\nu(p))$, where $\Delta_\nu(p)$ can be assumed Gaussian. One finds that the equivalent of Equation (4.4),

$$\sum_{\nu} \alpha_\nu w_\nu (1 + \Delta_\nu(p)) = 0, \tag{4.5}$$

now cannot be satisfied within the entire region $\Omega$ up to the Gaussian term $\sum_\nu \alpha_\nu w_\nu \Delta_\nu(p)$. For the same reason the variance of $\mathcal{S}$ is biased by the term

$$\left\langle F^2(p) \sum_{\nu\mu} \left[2 + \Delta_\nu(p)\right] \Delta_\mu(p) \alpha_\nu \alpha_\mu w_\nu w_\mu \right\rangle_\Omega, \tag{4.6}$$

in addition to the one describing chance correlations between the CMB and $\Delta_\nu(p)$. The first term accounts for the correlation between $\Delta_\nu(p)$ and the foreground 'intensity', $F^2(p)$, while the second term, $\propto (F(p)\Delta_\nu(p))^2$, scales like the variance of these correlations. In the case of a power-law foreground with $\alpha_\nu(p) = (\nu/\nu_0)^{\beta(p)}$ the spectral index can be written as $\beta(p) =$

[1] It should be clear that in the case where Equation (4.3) (or its extension to $n$ foregrounds) is fulfilled, the minimization of the variance becomes redundant. In the case of a single foreground only two observations at different frequencies are required to solve for the weights $w_\nu$:

$$w_1 = -\frac{\alpha_2}{\alpha_1}\left(1 - \frac{\alpha_2}{\alpha_1}\right)^{-1}, \quad w_2 = \left(1 - \frac{\alpha_2}{\alpha_1}\right)^{-1}$$

[2] Indeed, with the onset of more precise measurements of the radio sky, it will become increasingly clear that the spectral index of synchrotron emission varies across the sky (Taylor, 2018; Krachmalnicoff et al., 2018), and also for thermal dust emission such variation has been observed and is known as de-correlation (Planck intermediate results. L) (see, however, Sheehy and Slosar (2018) and Planck 2018 results. XI).

$\beta + \delta\beta(p)$. Assuming that the variation $|\delta\beta(p)| \ll \beta$ one can approximate $\alpha_\nu(p) \approx \alpha_\nu(1 + \delta\beta(p)\ln(\nu/\nu_0))$ which leads to the corresponding form of Equation (4.6),

$$\left\langle F^2(p) \sum_{\nu\mu} \left[ 2 + \delta\beta(p) \ln\left(\frac{\nu}{\nu_0}\right) \right] \delta\beta(p) \ln\left(\frac{\mu}{\nu_0}\right) \alpha_\nu \alpha_\mu w_\nu w_\mu \right\rangle_\Omega . \tag{4.7}$$

Keeping in mind the potentially varying properties of foregrounds across the sky, I allow myself one last remark about the ILC approach, where I consider those patches of the sky, in which the foregrounds are completely uncorrelated from band to band. In these zones one can model the correlation matrix $\langle F_\nu\, F_\mu \rangle_\Omega$ in Equation (4.2) as a diagonal matrix:

$$\langle F_\nu\, F_\mu \rangle_\Omega = \langle F_\nu\, F_\mu \rangle_\Omega\, \delta_{\nu,\mu} \tag{4.8}$$

where $\delta_{\nu,\mu}$ is the Kronecker symbol. Then, the contribution to the total variance $\langle \mathcal{S}^2 \rangle_\Omega$ from the foreground components simplifies to

$$\sum_{\mu\nu} \langle F_\nu\, F_\mu \rangle_\Omega\, w_\nu w_\mu = \sum_{\nu} \langle F_\nu^2 \rangle_\Omega\, w_\nu^2, \tag{4.9}$$

which is overall positive-definite. Already given Equation (4.8), one sees that foregrounds of this sort cannot be removed by linear combination.

In this rough exploration I have not considered noise terms. However, their inclusion would only lead to the addition of the noise covariance matrix, and the corresponding cross-covariance matrices in Equation (4.2), and not change the arguments about the foreground properties made above. In particular, Equations (4.8)–(4.9) look equivalent for non-correlated noise terms. Yet there is an essential difference between uncorrelated foreground and uncorrelated noise: By the continuing improvement in detector technology, one may obtain lower noise levels and thereby reduce the influence of this term; the contribution from uncorrelated foregrounds, however, remains the same. In the case of *Gaussian*, uncorrelated foregrounds (or noise) Equation (4.8) completely describes their properties, and in the light of the previous discussion one finds Gaussianity in a region $\Omega$ to arise from either the foreground 'template' $F(p)$ itself, or from the direction-dependent term $\Delta_\nu(p)$, while the respective other remains nearly constant. In particular, any residual of the sort described in Equation (4.5), will itself be Gaussian. The later distinction of such contamination from the also Gaussian CMB will be challenging.

It is these considerations which motivate a spatially resolved investigation of foregrounds

with regards to their statistics — in specific, I shall investigate their similarity (or dissimilarity) to Gaussian variables in small patches distributed over the sky, in addition to studying correlations between foreground maps on the same scales.

## 4.2 Method

In the light of the above, I present a general approach for studying sky maps by investigating their local one-point distribution in small patches. This approach has the advantage of being blind to the global structure of the map. An obvious feature of foreground maps is that they reflect structures in our Galaxy. It is unreasonable to expect that its myriad distinct, specific and complex features can be regarded as a whole suitable for a global analysis with statistical tools. On the other hand, simple statistical measures can provide useful tools for analyzing sufficiently small local patches of these maps.[3] This is simply an example of the fact that the properties of data sets are often scale-dependent. By selecting an appropriate patch size, it is possible to focus on a specific scale of interest and thus to add flexibility to the analysis. Working with patches also enables one to identify regions of the sky with anomalous properties such as non-Gaussian regions of the CMB map and Gaussian regions of foreground maps. In addition, the characterization of local foreground properties can be an important aid in the design of experiments that wish to focus on small regions of the sky with favorable local properties. Given the large scale structures expected in foreground maps, it is natural to consider the dimensionless moments (i.e., moments that are independent of the local mean and variance) one patch at a time. Thus, here I investigate the use of the skewness and kurtosis as statistical probes.

I will demonstrate the method of analysis using two sky maps with quite different properties. One will be a map where the values for each pixel were independently drawn from a Gaussian, and another will be the *Planck* 2015 SMICA sky map of CMB temperature fluctuations (Planck 2015 results. IX), encountered and introduced previously. While the first example is Gaussian by construction, the SMICA map and its predecessors have been studied in considerable detail in recent years, and its properties are well-understood. It is known in particular that it can be regarded as consistent with a realization of a statistically homogeneous and isotropic random Gaussian process.

[3] These patches, which will be defined more precisely below, are locally defined non-overlapping regions that collectively cover the entire sky, equivalent to those patches defined in section 3.2 for the mosaic correlations.

### 4.2.1 Skewness, kurtosis and non-Gaussianity

At first I clarify definitions and general properties of the statistics which shall be employed. Consider a data set consisting of $n$ random draws of the variable $x$ on a given distribution. The moments of this data set relative to the mean, $\overline{x}$, are given simply as

$$m_k = \frac{1}{n}\sum_i (x_i - \overline{x})^k, \tag{4.10}$$

where $m_2$ is the usual variance. For present purposes I will be concerned with the moments in various patches of the sky. Thus, the sum in Equation (4.10) should extend over all pixels in the patch under consideration, and the mean $\overline{x}$ is similarly that of the patch. For $k > 2$, it is useful to adopt $m_2^{1/2}$ as a unit of length in order to obtain moments, $\mu_k = m_k/m_2^{k/2}$, that depend on the shape of the underlying distribution but are independent of its scale. If the distribution in question is Gaussian, $\mu_k = 0$ for odd $k$ and $\mu_k = (k-1)!!$ for even $k$ in the limit $n \to \infty$. For studying the non-Gaussianity of a general distribution, it is convenient to measure these moments relative to their Gaussian values. Thus, the skewness and excess kurtosis are defined respectively as

$$\gamma_1 = \mu_3 \quad \text{and} \quad \gamma_2 = \mu_4 - 3. \tag{4.11}$$

The skewness and excess kurtosis of the elements of a data set have distributions whose low moments are known for the special case of Gaussian distributions. Specifically, the mean and variance values of $\gamma_1$ are

$$\begin{aligned} \mathrm{E}[\gamma_1] &= 0 \\ \mathrm{Var}[\gamma_1] &= \frac{6(n-2)}{(n+1)(n+3)}, \end{aligned} \tag{4.12}$$

while for $\gamma_2$ they are

$$\begin{aligned} \mathrm{E}[\gamma_2] &= -\frac{6}{n+1} \\ \mathrm{Var}[\gamma_2] &= \frac{24n(n-2)(n-3)}{(n+1)^2(n+3)(n+5)}. \end{aligned} \tag{4.13}$$

Further, each of these distributions is known to be normal in the limit of large $n$.

Comparison of the distribution of skewness *or* excess kurtosis resulting from random draws on an unknown distribution with such known results can provide a test of non-Gaussianity. I

will argue here that it is of potentially greater value to consider the distribution of skewness *and* kurtosis. Before addressing this point, however, it is important to note that the values of $\gamma_1$ and $\gamma_2$ resulting from $n$ random draws on any given distribution are not independent. To see this, consider a single random draw of any size, $n$, on an arbitrary distribution. Without loss of generality, shift and rescale these numbers to ensure mean 0 and variance 1. Calculate the average value of the non-negative function $(x-a)^2(x-b)^2$ in terms of the moments $m_3$ and $m_4$ for this draw, and minimize the result with respect to the real parameters $a$ and $b$. The result of these operations is the Pearson inequality (Pearson, 1916),

$$\gamma_2 \geq \gamma_1^2 - 2. \tag{4.14}$$

Note that the equality is satisfied if and only if the distribution permits only the values $x = a$ and $x = b$. Thus, although stronger inequalities can be constructed for special classes of distributions (e.g., unimodal or symmetric unimodal distributions (Rohatgi and Székely, 1989; Klaassen et al., 2000)), there is no stronger general inequality involving skewness and kurtosis.

As stated above, the distributions of skewness and kurtosis are normal in the large-$n$ limit for the special case of a Gaussian. Noting that their associated variances differ by a factor of 4 in this limit, Jarque and Bera (1980) were led to study the properties of the combination $(\gamma_1^2 + \gamma_2^2/4)$ and to show that its asymptotic behaviour in the large-$n$ limit is precisely that of a $\chi^2$-distribution with two degrees of freedom. In principle, comparison with this familiar distribution offers a more accurate measure of Gaussianity than either the skewness or kurtosis alone. In practice, convergence to the asymptotic limit is slow. This has prompted the introduction of ad hoc transformations (D'Agostino, 1970) to render the skewness and kurtosis "more Gaussian" with the aim of improving the accuracy of this combined measure. The fact that these transformations treat skewness and kurtosis as independent means that they cannot respect the Pearson inequality and serves as a reminder that their utility is greatest in the region of maximum probability ($\gamma_1 = 0$ and $\gamma_2 \to 0$).

With the aid of Equations (4.12) and (4.13), the skewness and kurtosis can be useful in deciding whether a given data set is the result of uncorrelated random draws on a Gaussian or a non-Gaussian distribution. They are not a priori suitable for treating systems such as the SMICA map of CMB temperature fluctuations where the expectation of uncorrelated random draws in harmonic space necessarily implies the existence of correlations in pixel space. I will address this problem in the following.

### 4.2.2 Uncorrelated vs. Correlated Data

When attempting to analyze the distribution of pixel values of sky maps in small patches, one must deal with the complication that these pixels are expected to be correlated. Maps depicting mainly Galactic foreground emissions are correlated on scales corresponding to the sizes of structures in the Galaxy, which can vary greatly when projected on the sphere. According to the standard cosmological model, however, maps of CMB temperature fluctuations, such as the *Planck* SMICA map, are expected to be correlated in pixel space. Although the harmonic coefficients can be assumed to have been drawn uncorrelated in harmonic space, the transformation to the pixel domain then ensures that the pixels are correlated. Assuming a homogeneous and isotropic distribution based on the angular power spectrum, $C_\ell$, the angular correlation function depends only on the separation angle, $\theta$, between pixels and is given by

$$C(\theta) = \sum_\ell \frac{2\ell+1}{4\pi} C_\ell P_\ell(\cos\theta), \tag{4.15}$$

where $P_\ell$ are the Legendre polynomials. One can then define the expected angular scale of the correlation, $\theta_c$, as

$$\theta_c^2 = \frac{C(0)}{|C''(0)|} = \frac{2\sum_\ell (2\ell+1)C_\ell}{\sum_\ell \ell(\ell+1)(2\ell+1)C_\ell}. \tag{4.16}$$

For example, here I will consider the SMICA map smoothed with a Gaussian kernel of $20'$ FWHM, which allows to use only scales up to $\ell_{\max} \simeq 1000$. If $C_\ell = g_\ell^2 C_\ell^{\Lambda\mathrm{CDM}}$, where $C_\ell^{\Lambda\mathrm{CDM}}$ is the *Planck* best-fit $\Lambda$CDM power spectrum (Planck 2015 results. XI) and $g_\ell$ is the smoothing kernel, Equation (4.16) results in a correlation angle $\theta_c = 29'$. When considering data in a patch of angular size $\theta_p$, one should expect that correlations will have a non-negligible effect on the joint distribution of the skewness and excess kurtosis of the data unless $\theta_p/\theta_c \gg 1$.

The effect of correlations is readily demonstrated. The hierarchical nature of the tesselization scheme HEALPix (Gorski et al., 2005) is used to partition a sky map of resolution $N_{\mathrm{Side}} = 512$ into non-overlapping patches by assigning each pixel to a patch on a grid of $N_{\mathrm{Side}} = 16$. This results in $N_p = 3072$ patches with an angular size of $\theta_p = 3.7°$, each containing 1024 pixels. I calculate the skewness and excess kurtosis of the pixels in each patch and bin them into a bivariate histogram. In order to smooth the statistical fluctuations of the histograms, I draw 1000 realizations of sky maps and calculate the mean of all histograms. I consider two such ensembles. The first is drawn in pixel space with pixels drawn uncorrelated from a normal distribution. The second ensemble is drawn in harmonic space, and I use the smoothed angular

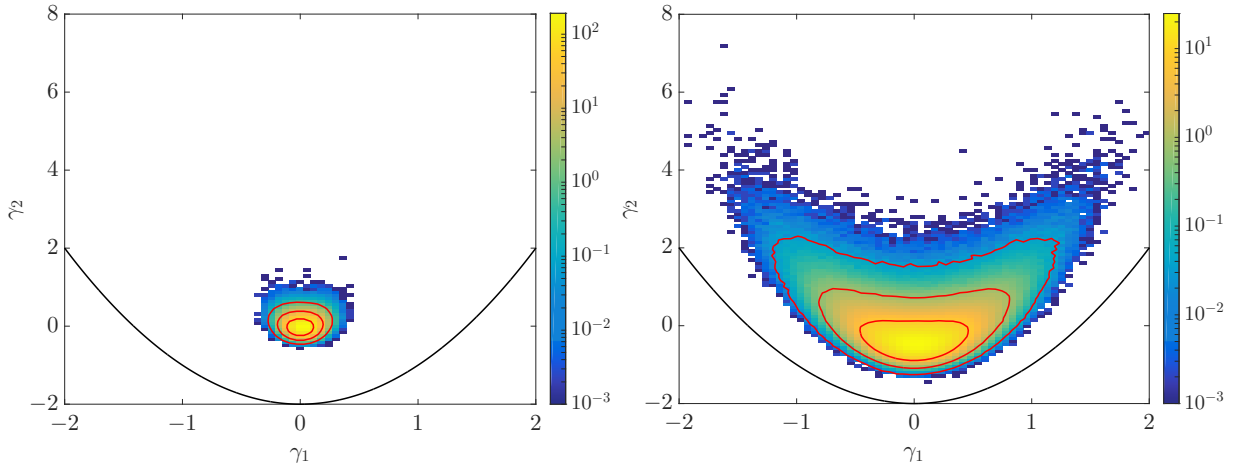


Figure 4.1 Mean histogram of skewness and excess kurtosis, calculated on uncorrelated (*left panel*) and correlated (*right panel*) pixels with $\theta_\mathrm{p}/\theta_\mathrm{c} = 7.5$. The colors represent (mean) counts, on a logarithmic scale. Also plotted are the constraint parabola (*black*) imposed by Pearson's inequality (4.14) and the 1–3$\sigma$ contour lines (*red*).

power spectrum $C_\ell$ mentioned above to draw the uncorrelated harmonic coefficients from a Gaussian distribution. This results in correlated pixels with $\theta_\mathrm{p}/\theta_\mathrm{c} = 7.5$. The two mean histograms are shown in Figure 4.1. The difference between the two is striking. Pixel correlations cause the distributions of both $\gamma_1$ and $\gamma_2$ to be much wider, and their interdependence is made more apparent by the fact that the contour lines of the histogram are no longer elliptic.

An alternative strategy is therefore required for analyzing the joint distribution of $\gamma_1$ and $\gamma_2$ on the patches of a given sky map that will allow for correlations of the pixels. To this end, a straightforward generalization of the strategy is chosen — common in one dimension — of comparing to an ensemble. Given an ensemble of realizations, I calculate the mean bivariate histogram, as those shown in Figure 4.1, and use it as a proxy for the two-dimensional probability distribution of the moments. This histogram, $h_{ij} = h(\gamma_{1,i}, \gamma_{2,j})$, where $\gamma_{1,i}$ and $\gamma_{2,j}$ are the bins of the moments, can now be used to assign a $p$-value to each point, $(\gamma_1, \gamma_2)$, in the skewness–kurtosis plane in the following way. First, I calculate the value $h(\gamma_1, \gamma_2)$ by interpolation of the discrete histogram $h_{ij}$. I then find the bins comprising the appropriate 'tail' of the distribution, i.e. the set of all bins with smaller counts, $T = \{(i,j) \mid h_{ij} \leq h(\gamma_1, \gamma_2)\}$. Finally, the probability to exceed the given value is calculated as $p = N_\mathrm{p}^{-1} \sum_{(i,j)\in T} h_{ij}$, where the number of patches, $N_\mathrm{p}$, is obviously also the sum of $h_{ij}$ over all bins. This procedure allows one to draw in Figure 4.1 contours representing the 1–3$\sigma$ bounds of the distribution, where I use the standard definition for the normal distribution to convert the language of $p$-values to that of $\sigma$-values, i.e. $1\sigma$ corresponds to $p = 31.7\%$, etc.

With a $p$-value assigned to each patch, it is possible to identify anomalous regions and to

inspect them more closely. However, these $p$-values still depend on the nature of the ensemble of realizations chosen as a basis of comparison. I will utilize this procedure to analyze the SMICA and Haslam maps in the following section. Note that the assumption of statistical homogeneity and isotropy cannot be justified for foreground maps such as the Haslam map. While there is thus no guarantee that the strategy outlined here is quantitatively reliable when applied to foreground maps, I shall demonstrate that it can provide useful qualitative guidance.

## 4.3 Analysis of sky maps — Temperature

### 4.3.1 The SMICA Map

I start by analyzing the *Planck* 2015 SMICA map of CMB temperature fluctuations (Planck 2015 results. IX) (Planck 2015 results. IX). I degrade the map from its native HEALPix resolution of $N_{\mathrm{Side}} = 2048$ to a resolution of $N_{\mathrm{Side}} = 512$ after first smoothing it with a Gaussian kernel of $20'$ FWHM. Using an $N_{\mathrm{Side}} = 16$ grid for the patches as described above, one obtains the skewness–kurtosis of the SMICA patches shown in Figure 4.2. Note that the choice of smaller patches, e.g. by using a grid of $N_{\mathrm{Side}} = 32$, would result in larger statistical fluctuations of the moments since each patch would contain fewer pixels. In addition, the smaller patch would be closer to the correlation angle of the map. While smaller patches could still be used for SMICA, they would not be appropriate for the Haslam map to be analyzed below.

In order to assess the expected distribution of the moments for the SMICA map, I draw a Gaussian ensemble for purposes of comparison. While the SMICA map also contains other effects (such as instrumental noise and foreground residuals) in addition to the dominant Gaussian signal, it was recently shown (Ben-David et al., 2015a) that the statistical properties of a Gaussian ensemble are close to those of the *Planck* full focal plane (FFP) simulations, which include some of these additional effects on sufficiently large scales. I therefore use a Gaussian ensemble here and will show that the statistical properties of the skewness and excess kurtosis of the SMICA map are consistent with it. Since it should be ensured that the Gaussian ensemble has the same correlation structure in pixel space as the SMICA map, I use the ensemble of 1000 realizations based on the best-fit ΛCDM angular power spectrum described in the previous section. The mean histogram for this ensemble was shown in the right panel of Figure 4.1, and the 1–3$\sigma$ contour lines calculated based on it are superimposed on the SMICA histogram in Figure 4.2.

The contour lines strongly suggest that the distribution of patch $p$-values for the SMICA map follows the expected distribution, with $\approx 0.1\%$ of the patches crossing the $3\sigma$ boundary. I

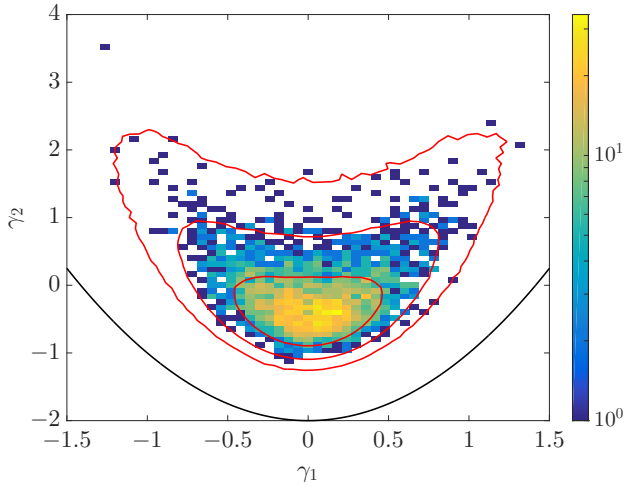


Figure 4.2 The skewness–kurtosis histogram for the SMICA map. Also plotted are the constraint parabola and the same contour lines as in the right panel of Figure 4.1.

use the mean histogram to assign a $p$-value to each patch as described above and plot in the left panel of Figure 4.3 the distribution of the values.

It is apparent that the distribution is quite uniform. This provides confirmation that the SMICA map is indeed consistent with our ensemble of realizations and provides further support for the conclusion of Ben-David et al. (2015a) that the more complicated FFP simulations are not essential for analyzing the statistical properties of the SMICA map; simple Gaussian appear to be sufficient.[4] Moreover, in the context of the present analysis, this conclusion can be extended to smaller scales with $\ell_{\rm max}$ as large as 1000.

Having labeled each patch with a $p$-value, or the corresponding $\sigma$-levels, the spatial distribution of these values can now be considered. I therefore plot in Figure 4.3 a map showing the $p$-values, translated to $\sigma$-levels, of the patches of the SMICA map. Visual inspection of the SMICA patches suggests a tendency towards an excess of outliers in the Galactic plane, though I did not investigate this question quantitatively.

### 4.3.2 The Haslam map

In addition to the SMICA map of CMB temperature fluctuations, I also apply our method to a reprocessed version (Remazeilles et al., 2015) of the 408 MHz radio map of Haslam et al. (1982). I adopt this map as typical of the maps used as templates for cleaning foreground contributions

[4]This, of course, does not exclude the possible benefit FFP simulations can have in quantifying the influence of systematics arising during mapmaking on a particular estimator of interest. It simply states sufficiency for the statistics presented here.

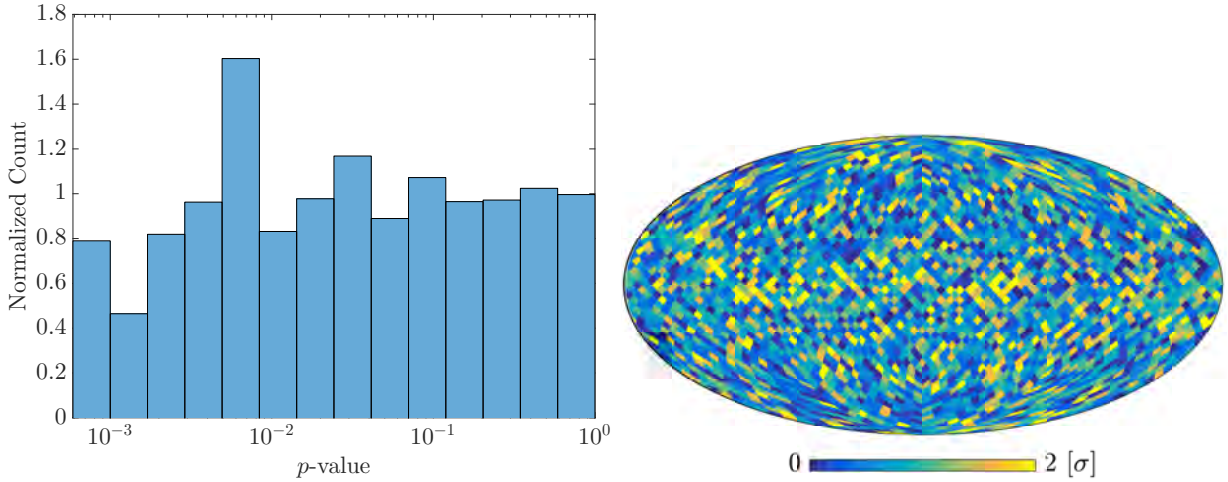


Figure 4.3 *Left panel:* The distribution of $p$-values for the SMICA patches. The bin edges are logarithmically spaced and the histogram is normalized to unit total area. *Right panel:* The $\sigma$-level for each patch of the SMICA map, in Galactic coordinates.

to the CMB data. Understanding the statistical properties of such maps, or at least finding outlying regions in them, could improve the accuracy of CMB extraction. Since it is primarily a map of Galactic emissions, one does not expect the Haslam map as a whole to be Gaussian-distributed. Working in small patches, however, allows one to inspect the distributions in local areas of the map that may or may not be Gaussian. The 56′ resolution of the map enables one to choose a patch grid (with $N_{\text{Side}} = 16$ but not smaller) identical to that chosen for the SMICA map. Since the Haslam map is provided in an $N_{\text{Side}} = 512$ pixelization, I am again left with 1024 pixels in each patch.

The skewness–kurtosis histogram for the Haslam map is shown in the left panel of Figure 4.4. The range of values of $\gamma_1$ and $\gamma_2$ is far larger than that found in the case of the SMICA map (Figure 4.2). It is also immediately apparent that it is much more probable for a Haslam patch to have positive skewness than negative. I will comment more on this asymmetry below.

As before, an ensemble is required in order to assign a $p$-value to each patch. In contrast to the map of CMB fluctuations, however, the Haslam map is not believed to be a Gaussian realization drawn in harmonic space using some angular power spectrum. Thus, it is not clear how to generate a suitable ensemble. Note first that the ensemble should be Gaussian. This is a result of *my* wish to classify the patches by their level of Gaussianity and is unrelated to the intrinsic distribution of the data. The determination of the nature of this Gaussian or, equivalently, of the corresponding correlation matrix of the Haslam map would require detailed knowledge of the specific physical processes that govern synchrotron emissions in the Galaxy. In the interests of simplicity and generality, I prefer using the correlation structure

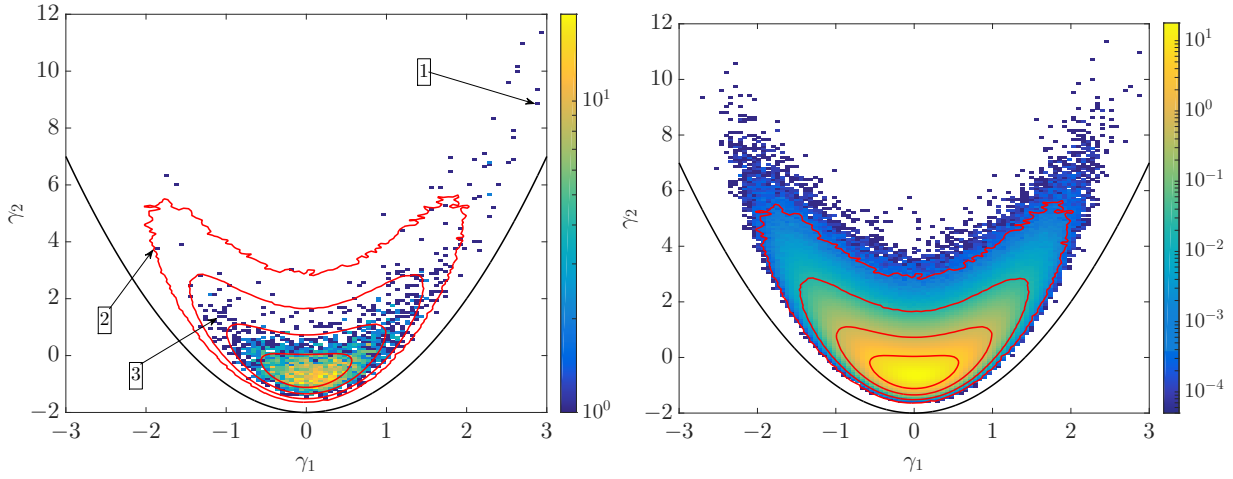


Figure 4.4 *Left panel:* The skewness–kurtosis histogram for the Haslam map. The bins of the three patches given as examples below are marked with arrows. *Right panel* Mean histogram based on Gaussian realizations using the Haslam power spectrum, as explained in the text. The same set of 1–4$\sigma$ contour levels, calculated using the mean histogram, is shown in both panels (*red*).

of the Haslam map itself as a reference point. In order to obtain a statistical measure of the correlations, one is then led to treat the map as a realization of a homogeneous and isotropic distribution. I transform the map to the spherical harmonic domain and calculate the observed power spectrum,

$$\widehat{C}_\ell = \frac{1}{2\ell+1} \sum_{m=-\ell}^{\ell} |a_{\ell m}|^2, \tag{4.17}$$

where the $a_{\ell m}$ are the harmonic coefficients. I then use this power spectrum to draw Gaussian realizations in harmonic space. This results in an ensemble of maps having, on average, the same structure of correlations as the Haslam map. Here I set $\ell_{\max} = 600$ since the Haslam angular power is negligible for smaller scales (larger values of $\ell$). I draw 20 000 realizations, which allows to reach a significance level of 4$\sigma$.

The mean histogram obtained using this ensemble is shown in the right panel of Figure 4.4. I use it to calculate the 1–4$\sigma$ contour levels and superimpose them, as an illustration, on both histograms of Figure 4.4. It is clear that many patches of the Haslam map are located far beyond the 4$\sigma$ contour and are therefore potentially interesting. However, it is also intriguing that so many of the patches are located within the 1$\sigma$ contour in light of the fact that the map as a whole is highly non-Gaussian. This is an illustration of the advantage of an analysis of small patches; it can highlight local features while disregarding global features of the map. I

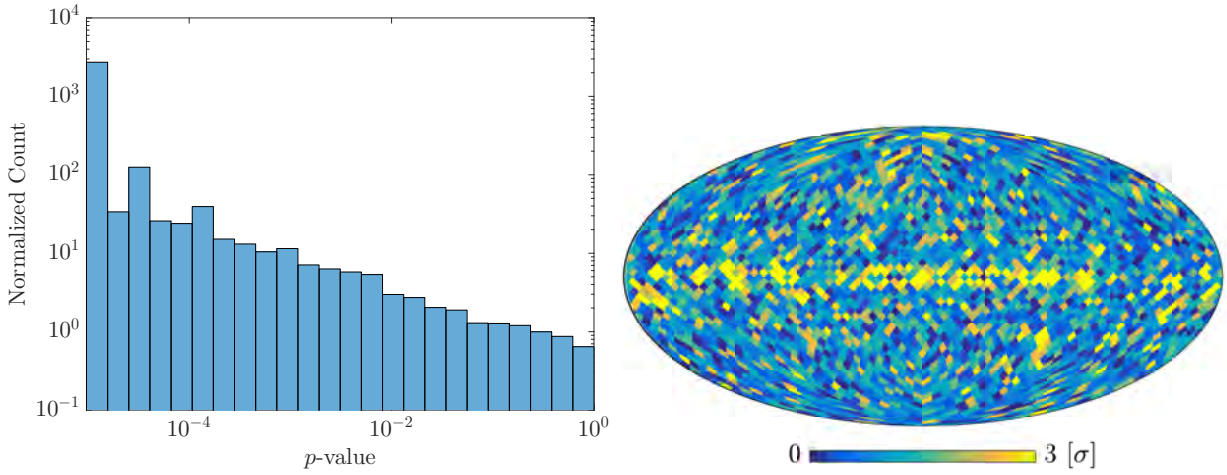


Figure 4.5 *Left panel:* The distribution of $p$-values for the Haslam patches. The bin edges are logarithmically spaced and the histogram is normalized to unit total area. Note that the leftmost column here represents the sum of all patches with $p \lesssim 10^{-5}$. *Right panel* The $\sigma$-level for each patch of the Haslam map, in Galactic coordinates.

can now assign $p$-values to the patches. Their distribution is plotted in Figure 4.5. One can see that the distribution is not uniform. This indicates, as expected, that the Haslam map as a whole is not a consistent realization of the ensemble.

As with the SMICA map, one can examine the spatial distribution of the patches labeled by their significance levels. This map is shown in Figure 4.5. It is immediately apparent that many of the highly non-Gaussian patches are located in the area of the Galactic plane. More surprisingly, it is evident that many of the patches in the Galactic plane are labeled with a very low value of $\sigma$. (I will suggest below that this result does not necessarily indicate that these patches are free of non-Gaussian foreground effects.) Also note some highly non-Gaussian patches at high Galactic latitudes far from the Galactic plane.

The intriguing results of Figure 4.5 (right panel) provide motivation to examine some of the patches by eye in the hope of determining why they are anomalous. The labeling of the patches by $p$-values (or $\sigma$-levels) provides a natural ordering scheme for their examination. I select three patches that are each characteristic of their locations in the skewness–kurtosis histogram, Figure 4.4 (left panel). Their positions in this histogram are indicated by the labels '1', '2' and '3'. In addition, in Figure 4.6 I show the Haslam map and indicate on it the location of the patches. They lie in different areas of the map and have distinct characteristics. The panels of Figure 4.7 show the patches in question (enclosed in white) along with portions of their neighboring patches.

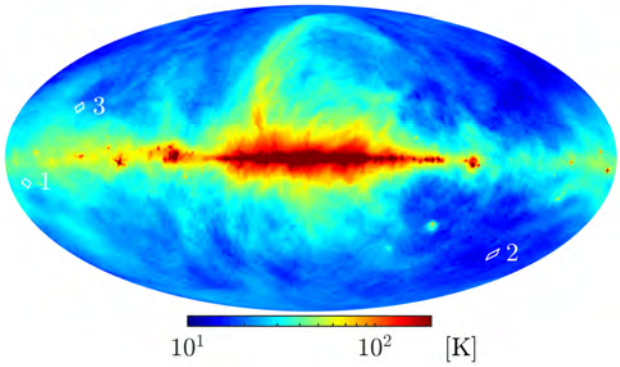


Figure 4.6 The reprocessed 408 MHz Haslam map, in Galactic coordinates with locations of the three sample patches marked in white.

- The first of these patches, Figure 4.7(a), belongs to the relatively well-populated branch of the histogram with high kurtosis and large positive skewness. Such values arise naturally when the distribution of the patch contains a small area of relatively high intensity. These conditions are easily produced by a point source as is the case in the figure shown. The region of high intensity covers only a small fraction of the patch; the bulk has an intensity that is relatively low compared to the mean intensity of the patch. Patches with similar distributions are most frequently found along the Galactic plane. This fact is clearly visible in Figure 4.5 and incidentally provides qualitative confirmation of the success of the method in Remazeilles et al. (2015), which was designed to remove extragalactic point sources from the original Haslam map.

- I now consider patch 2—a patch selected from the less populated branch of the histogram in Figure 4.4. The large magnitudes of the kurtosis and skewness again ensure that the $p$-value of this patch is small. In this case, however, the skewness is strongly negative. The patch should contain a small region of very low intensity while the complementary area should have an intensity somewhat above the average value. The obvious analogy to Figure 4.7(a) thus makes it reasonable to expect to find a cold spot or point sink. Clearly, Figure 4.7(b) meets this expectation. Although a cursory glance at the night sky is sufficient to remind one of the existence of point sources, it is more challenging to think of explanations for the phenomenon of cold spots. There are several possible explanations for the existence of regions where the intensity of synchrotron radiation is low. Small magnetic fields and/or low electron densities can reduce the intensity of radiation emitted from a given region. Alternatively, intervening matter can absorb synchrotron radiation once it has been emitted. These effects can work individually or in concert. The relative paucity of patches with large negative skewness, evident in the left histogram of Figure 4.4,

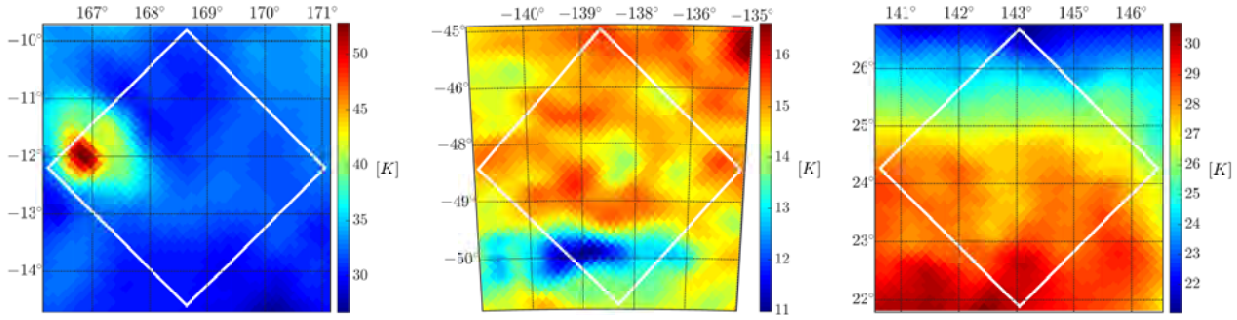


(a) (b) (c)

Figure 4.7 From left to right, patches 1, 2, and 3 and portions of their neighboring patches. The vertical and horizontal axes show Galactic latitude and longitude, respectively. The skewness and kurtosis of each patch can be seen in Figure 4.4, and Figure 4.6 shows their locations on the Haslam map.

suggests that localized radiation sinks are significantly less likely than bright point sources.

- The results reported here were obtained from a single patching pattern. It can happen, however, that the specific values of skewness and kurtosis of a given patch can be highly sensitive to its particular position on the map. Thus, a patch with high skewness and kurtosis need not necessarily contain a point source but can rather lie at an advantageous location, grazing a larger-scale structure. This can also occur for other values $(\gamma_1, \gamma_2)$, e.g., also simulating cold point sources. Thus, patch 3 in Figure 4.7(c) illustrates a case where the patch lies on top of a larger structure in which the temperature changes smoothly over the area of the patch. The value of the skewness—including its sign—will depend on the precise location of the patch relative to this fixed large scale structure.

- The last case, not shown in a figure here, is that of random fluctuations. Large fractions of the sky are dominated by diffuse emission, which in the case of the Haslam map is closely connected to the morphology and fluctuations in the Galactic magnetic field and the local electron density. The pixels contained in patches lying in these regions will be distributed in a largely Gaussian manner. The histogram in the left panel of Figure 4.4, reveals that approximately 52% of the patches in the Haslam map are Gaussian with $\sigma \leq 1$, and inspection of the map in Figure 4.5 provides visual confirmation. The dominance of Gaussian patches was expected for the SMICA map and is quantitatively confirmed by Figures 4.2–4.3. A similar dominance in the Haslam map was *not* expected. I will return to this surprising result in the following section.

## 4.4 Intermediate discussion

The content of sections 4.2 and 4.3 is intended to illustrate the role that higher moments can play in understanding the statistical behaviour of foreground maps, especially in different patches of the sky. In practice, it is necessary to adjust the size of the patches to ensure that two obvious criteria are met: The patches must be large on a scale set by the correlation angle, $\theta_c$, in order to ensure that individual pixels have a reasonable degree of statistical independence. Second, the patches must be small in comparison with the size of diffuse foreground effects. Such considerations led me to choose patches with $N_{\mathrm{Side}} = 16$. Clearly, patch size can be tuned to the scale of phenomena that one would like to identify. For example, the southern hemisphere cold spot seen in both *WMAP* and CMB temperature maps has an angular size of approximately 5°. As a consequence, it does not appear to be exceptional in the SMICA plot of Figure 4.3 (right panel) that was obtained with a patch size of 3.7°. It should be easy to spot with a larger patch size. I have also presented the method using a single realization of tesselization. Since I have noted some phenomena that can be sensitive to the precise location of a patch, it would be prudent to consider several tilings displaced by an amount comparable to the patch size. Patch selection here was made using the HEALPix package that produces a subdivision of a spherical surface into patches of equal area, but this method can evidently be used for other patch forms and sizes. Also note that, although the decision to consider the statistics of skewness and kurtosis was natural, the same approach could be expanded to include a larger number of higher moments. The only technical challenge in such an extension would be the determination of the inequalities analogous to Equation (4.14) that such higher moments must satisfy.

Turning to the results of this analysis, note that the SMICA map of CMB temperature fluctuations is entirely consistent with the expectation of Gaussian behaviour. This agreement is confirmed with considerable accuracy by the fact that the distribution of $p$-values shown in Figure 4.3 is independent of $p$.[5]

With a far larger fraction of patches with small $p$-values, the Haslam map would appear to confirm the a priori belief that this foreground map is strongly non-Gaussian. Closer inspection suggests that this conclusion may be premature. Figures 4.7(a)–4.7(c) show that classification of a patch by its $p$-value alone is not sufficient to describe its full physical content. These figures reveal three classes of anomalous patches that can be distinguished by their structure in pixel

[5] Bear in mind, for example, that the number of patches contributing to this histogram decreases rapidly as $p \to 0$.

space: point sources, cold spots and strong intensity gradients. Although it was not the goal to identify such structures, our method has the potential to do so mechanically. In practice, implementation should include shifting the location and changing the size of patches in order to avoid misidentification. Such localized phenomena differ distinctly from the diffuse effects of synchrotron radiation and merit special treatment when sky maps are to be cleaned. Their removal from Figure 4.4 (left panel) would eliminate many of the patches with $\sigma > 3$ and virtually all patches with $\sigma > 4$. The resulting histogram would have a significantly greater resemblance to a Gaussian result such as that shown in Figure 4.4 (right panel). There are two distinct explanations for this somewhat unexpected result. First, I note that the maps in Figures 4.3 and 4.5 contain a large number of patches with $p \approx 1$ in the Galactic plane in spite of the fact that this region should be filled with sources of foreground effects. Mertsch and Sarkar (2013) have argued that many independent foreground contributions can combine to create Gaussian distributions as a consequence of the central limit theorem.[6] For high Galactic latitudes, it is probably of greater importance to reconsider the assumptions of homogeneity and isotropy that led to the Gaussian realizations of the Haslam map shown in the right panel of Figure 4.4. While these assumptions are not expected to be valid for the map as a whole, they may well be valid locally on the relatively small scale of the patch size. In other words, large scale diffuse foreground effects can be described by correlations between spherical harmonics of relatively low order, $\ell \leq \ell_0$ without the involvement of components with $\ell > \ell_0$. These correlated terms will be approximately constant over patches whose characteristic size is smaller than $1/\ell_0$. They will not contribute to dimensionless moments such as the skewness and kurtosis that will be determined by the uncorrelated harmonics with large $\ell$. In either language, no deeper explanation is required to understand the abundance of Gaussian patches.

In summary, the possibility that Galactic foreground emission appears to have properties with directional dependence warrants an investigation in local patches. On the scales investigated, fluctuations in the Haslam map, selected as a representative for Galactic foreground maps, were shown to be consistent with Gaussian fluctuations according to the applied estimators. Assuming that foreground residuals in CMB maps, if present, correlate strongly with the guilty foregrounds themselves, one may be left with the sum of two Gaussian signals, which again is Gaussian-distributed. The presence of foreground residuals in CMB maps therefore need not be obvious at all, as the expected Gaussian statistics of the CMB would not be distorted. Naturally, these issues are more pressing in the more delicate analysis of polarized

[6] While this may not be the explanation of the global abundance of Gaussian patches seen in the Haslam map, it provides a useful reminder that the absence of evidence for the existence of non-Gaussian foreground effects does *not* constitute evidence of their absence.

microwave emission. In the next section I therefore present the work published as von Hausegger et al. (2018), in which the same procedure was applied to polarized foreground maps. While in the previous part only one single foreground map, namely the Haslam map of synchrotron emission, was investigated, in the following analyses of maps of the two strongest contributors to polarized Galactic emission will be presented — maps dominated by synchrotron, and maps dominated by thermal dust emission.

## 4.5 Analysis of sky maps — Polarization

### 4.5.1 Skewness and kurtosis

In the previous subsections I have tested departures from Gaussianity in patches of a full-sky temperature map at 408 MHz, representative for Galactic synchrotron radiation; I here extend the analysis to polarized foregrounds: maps of both polarized synchrotron and thermal dust emission. Even though formulated for temperature fields, the considerations of section 4.1 hold also for the removal of polarization foregrounds.[7] I will investigate the $E$- and $B$-modes of full-sky polarized foreground maps.

The maps under investigation here are the $E$ and $B$ maps of the *WMAP* K-band map (Bennett et al., 2013) and the *Planck* 353 GHz map (Planck 2018 results. III) primarily, which in polarization well describe synchrotron and thermal dust polarization, respectively[8]. All maps are smoothed with a 1° beam, prior to all calculations. As before, I present results from investigating maps at $N_{\mathrm{Side}} = 512$ in patches of $N_{\mathrm{Side}} = 16$, which corresponds to scales of approximately 3.7°. Despite this smoothing, the presence of noise in the polarization maps of both *WMAP* and *Planck* influences the signal at high Galactic latitudes. While this might not severely affect the results in this section, the clear consequence of this shall be seen in subsection 4.5.2.

In the context of polarization maps it is important to emphasize that finding any one region on the $E$- or $B$-mode sky to be particularly Gaussian (or non-Gaussian) does *not* equate to stating that physical processes in the same direction contribute to this finding. This is due to the non-local definition of the $E$- and $B$-modes: Each point on the $E/B$ sky receives contributions from all other points on the $Q/U$ sky, except its own direction (and its antipole; for a nice explanation, see Rotti and Huffenberger (2018)). One might argue, that therefore the many contributions are expected to render the signal in any particular direction Gaussian by the central limit theorem. None the less, the introductory arguments and searches for non-Gaussianity also in the CMB's $E$- or $B$-modes motivate a characterization of the foregrounds along similar lines.

[7] In addition to the assumptions about constant spectral indices or the like, the ILC approach in polarization requires the polarization angles of each component to be constant across frequencies. It is not clear whether the ILC in polarization is best performed on the Stokes parameters $Q$ and $U$, or their non-local transformations $E$ and $B$. Depending on the particular method, both are in use. Also combinations of both in decompositions like those proposed in Liu et al. (2018) and Rotti and Huffenberger (2018) might be of interest.

[8] I break consistency of using only *Planck* maps for I want to avoid the results being contaminated by residual systematics in the *Planck* 30 GHz map (see e.g. Weiland et al. (2018), or Table C.1 in Liu (2018)).

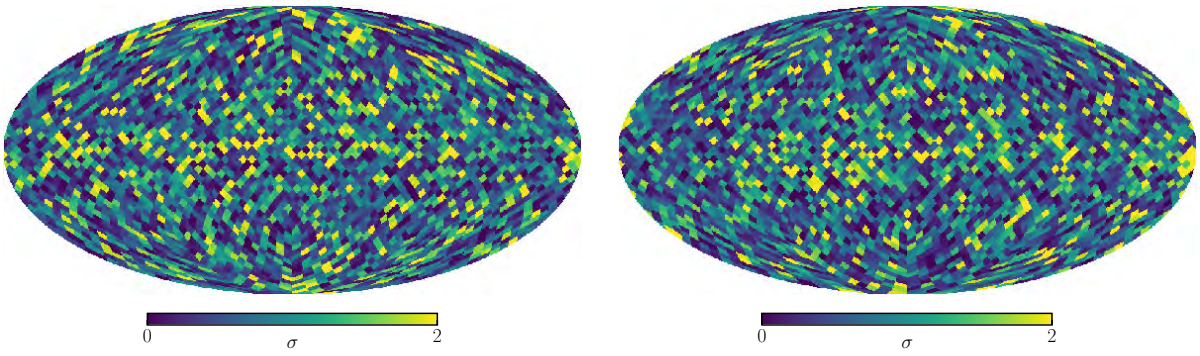


Figure 4.8 Significance of the skewness and kurtosis values in terms of the simulated Gaussian distributions in units of standard deviations, $\sigma$. The values were computed from the *WMAP* K-band $E$- (*left panel*) and $B$-mode (*right panel*) maps in patches of $N_{\mathrm{Side}} = 16$. The standard deviations are calculated using the probability distribution functions obtained from the simulations.

Equivalent to the procedures above, I produce Gaussian simulations of $E$ and $B$ maps based on the respective power spectra to compute skewness-kurtosis histograms á la Figure 4.4 (right panel). Using the simulations' probability distribution functions one again can assign a probability to each pair of skewness/kurtosis values, and thereby to each patch. By doing this I compute maps of departures from the Gaussian expectation in units of standard deviations for both $E$- and $B$-modes.

**Synchrotron polarization** I show maps of the standard deviations computed for the $E$- and $B$-modes of *WMAP*'s K-band map in Figure 4.8. Most patches deliver values below $2\sigma$ and therefore, according to this estimator, qualify as consistent (at this level) with arising from a Gaussian sample. Apart from hints towards peculiarities along the Galactic plane the distribution of values further does not seem to prefer certain regions on the sky. This finding resembles the one for the 408 MHz Haslam map, shown above.

**Dust polarization** Equivalent to the synchrotron results in the previous section I compute those of *Planck*'s 353 GHz polarization maps for the same patch sizes. These appear to be very similar, see Figure 4.9, apart from a slight surplus of high skewness patches, which lead to a correspondingly higher abundance of $> 2\sigma$ patches. This tendency is also observed in dust *temperature* maps and can be traced back to the presence of pronounced filaments and point sources in the dust maps. While point sources are not expected to be intrinsically polarized, filaments might appear visibly on polarization maps. In particular the $E$-mode will inherit power from polarized filaments, due to its sensitivity to elongated structures (see, e.g., Liu

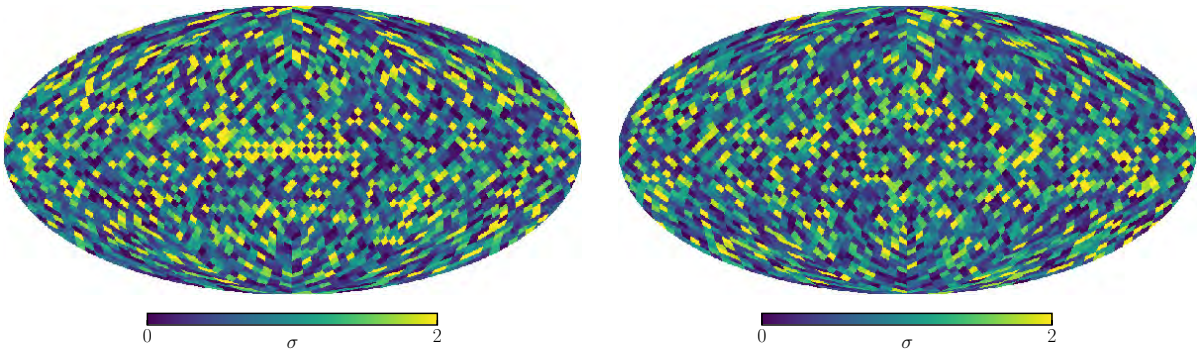


Figure 4.9 Same as Figure 4.8, just for the polarization of the *Planck* 353 GHz map.

et al. (2018)), and indeed the 353 GHz $E$-mode map is found to give $\approx 26\%$ more patches with values above $2\sigma$ than the $B$-mode map.

### 4.5.2 Correlations

In section 4.1 I discussed the possibility of spatially varying spectral indices, or, more generally, spatial variation in the scaling coefficient of a 'template' per foreground component. Another point of discussion was formed by regions $\Omega$ on the sky within which foreground or noise signal are uncorrelated from band to band. Both lead to terms in the $\mathcal{S}$ map's variance which prevent a minimization which is independent of sky location, and thereby constitute potential contamination in the final CMB product. I shall here investigate the same patches with regards to these properties which previously were tested for Gaussianity. For this I also utilize the *WMAP* Ka-band polarization maps and those of the *Planck* 217 GHz map.

As before, I at first focus on low and high frequency foregrounds separately. I each consider correlations between the signals measured in two bands, which are dominated by the same foreground mechanism. To make comparison to the results of the previous subsection, also here I compute Pearson correlations in patches of $N_{\mathrm{Side}} = 16$ via mosaic correlation known from section 3.2. Any correlation short from perfect, i.e. any change in a signal from one frequency to one nearby, can only be induced by spatial variations of the spectral index (or of an equivalent scaling of the foreground), or by instrumental noise; for the frequencies considered, no other polarized foreground components nor CMB should play a significant role besides synchrotron or thermal dust.

**Synchrotron polarization** To detect changes in the synchrotron sky in nearby frequencies I compare the *WMAP* K-band (23 GHz) with the Ka-band (33 GHz) polarization maps. Neither

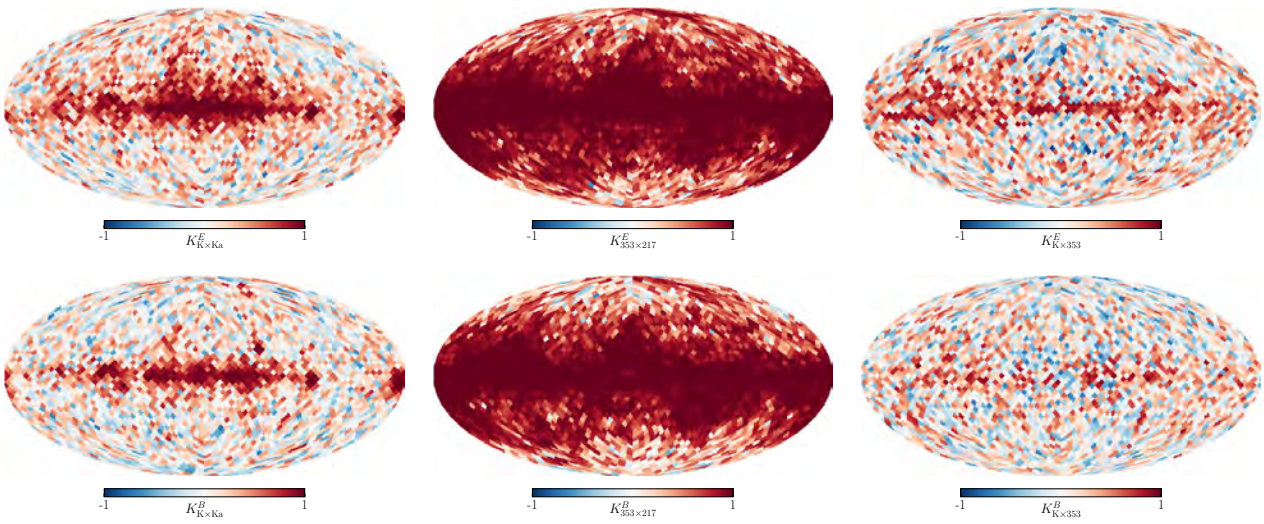


Figure 4.10 Mosaic correlations between $E$-mode (*upper panels*) and $B$-mode maps (*lower panels*). *Left panels:* Correlations between *WMAP* K- and Ka-band maps. *Middle panels:* Correlations between *Planck* 217 and 353 GHz maps. *Right panels:* Correlations between *WMAP* K-band and *Planck* 353 GHz maps.

of free-free emission, spinning dust emission, nor molecular line emission, is expected to be polarized at a level comparable to synchrotron emission over most of the sky, such that one can assume both maps to carry signal from either synchrotron emission or noise. I present the resulting mosaic correlation maps, $K^E_{\mathrm{K}\times\mathrm{Ka}}$ and $K^B_{\mathrm{K}\times\mathrm{Ka}}$, in the left panels of Figure 4.10. Distinct is the area of most pronounced correlations along the Galactic plane, slightly extending also along the North Polar Spur, especially for the $E$-mode maps. While positive correlations overweigh, at intermediate to high Galactic latitudes the correlations weaken and expose many patches with correlations close to zero, see also Figure A.3. In order to understand the origin of this reduced correlation I investigated *WMAP* K- and Ka-band single-year maps which showed that the dominating contributor at high Galactic latitudes is most likely noise. However, recall that it is irrelevant to the point presented in section 4.1 whether this loss in correlation arises from changes in the foregrounds' morphology or from uncorrelated instrumental noise in the two bands — both present challenges for ILC-like methods.

**Dust polarization** Applying the same method to the 217 GHz and 353 GHz *Planck* maps to obtain results for the polarized thermal dust sky, leads to the correlations presented in the middle panels of Figure 4.10. Similar to the case at low frequencies high correlation can be observed close to the Galactic plane and lower to vanishing correlation towards high Galactic latitudes. The larger abundance of high correlation patches, see also Figure A.4, is largely due

to higher signal-to-noise ratios in the maps (a conclusion also supported by analyzing half-mission maps), but could also indicate generally lower amount of spectral index variation in thermal dust emission.

**Correlations between synchrotron and dust** Before concluding one still needs to consider correlations between synchrotron and dust emission. In the case of more than a single foreground the variance $\langle \mathcal{S}^2 \rangle_\Omega$ will also contain cross-terms between the different foreground components such that the weights $w_\nu$ need to be determined according to high or low cross-correlation. I show the corresponding mosaic correlation maps in the right panels of Figure 4.10 for both $E$- and $B$-modes of the *WMAP* K-band and the *Planck* 353 GHz map. The tendency in both is higher correlations along the Galactic plane. However, away from the Galactic plane no strong correlation between the polarized emission of synchrotron and thermal dust emission is established on the scales given by the patch size investigated here. I further point out that while the high Galactic latitudes are most likely, as before, affected by instrumental noise, noticeable differences between the correlations at low Galactic latitudes from $E$- and $B$-modes can be seen — those latitudes where instrumental noise is subdominant. I return to this point in the discussion. However, higher sensitivity observations will be needed to characterize the foregrounds' polarized emission better both at low and at high frequencies.

## 4.6 Discussion

In section 4.5, I investigated statistics of the two strongest CMB foregrounds in polarization, synchrotron radiation and thermal dust emission, in order to draw conclusions on the feasibility of obtaining a clean CMB polarization map. In particular variations of foreground properties across the sky were of motivated interest wherefore I employed two methods which both work in predefined patches on the sky — the skewness-kurtosis method for classification of foreground maps as Gaussian processes (Ben-David et al., 2015b), known from section 4.2, and the mosaic correlations (von Hausegger and Liu, 2015), from section 3.2. The $E$- and $B$-mode maps under investigation were smoothed to $1^\circ$ and the selected patches were of extent $\sim 3.7^\circ$, which can be roughly translated into the multipole range $\ell \in [50, 180]$. I summarize my findings as follows:

- On scales between approximately $1^\circ$ and $3.7^\circ$ the $E$- and $B$-mode maps of both synchrotron and thermal dust polarization exhibit distributions consistent with those expected from Gaussian realizations over most of the sky, with preferred regions of departure only along the Galactic plane, cf. Figures 4.8 and 4.9.

This might prove itself helpful in the construction of polarized foreground simulations à la Hervías-Caimapo et al. (2016). Also studies of measuring polarization of the 21-cm line (Babich and Loeb, 2005) require simulations of polarized radio foregrounds. These findings can be seen as an addition to implementing or justifying assumptions about Gaussianity of foregrounds in such simulations, also in polarization (e.g. Jelic et al. (2008)).[9]

- On the same scales one finds spatial variation of the frequency spectra of both synchrotron and thermal dust polarization to be negligible along the Galactic plane, cf. Figure 4.10.
- At intermediate and higher Galactic latitudes increased instrumental noise prevents me from drawing conclusions about the spectral properties. However, the observed decrease in correlations also in the case of noise will impede ILC-like foreground removal algorithms, as elaborated in section 4.1.
- Mosaic correlations between synchrotron and dust polarization maps were distinctly different for $E$- and $B$-mode maps along the Galactic plane.

Given this last point, weights determined from the ILC approach would therefore be necessarily different for a foreground separation in $E$- or $B$-modes. Separation of foreground and CMB performed, for example, with the Stokes parameter $Q$ and $U$ maps, would thereby mix the distinct statistical properties of $E$- and $B$-mode signals. Exploration of new methods of foreground separation for polarized signals might therefore be desirable. Furthermore, depolarization effects add additional uncertainty and/or bias to foreground cleaning algorithms. Statistical investigations as those presented here offer means to understand such effects or their influences on the final CMB product in more detail, especially once higher fidelity polarization data become available.

It should not be omitted to mention that correlations between synchrotron and dust polarization have been subject to a many of recent studies to assess the potential level of foreground contribution at those frequencies where the CMB signal is strongest (Choi and Page, 2015; Krachmalnicoff et al., 2016, 2018; Akrami et al., 2018c). Their findings underline the existence of these correlations among the components also at high Galactic latitudes, and correlations were quantified for different scales by computing the corresponding cross-power spectra. However, they do not consider spatial variation of the correlation other than imposing Galactic masks of different extent. For the scales chosen in this work, these spatial variations were pointed out here, and, in addition to the differences between those spatial variations from $E$-

[9] Since the findings presented in section4.3 for a temperature map of synchrotron emission could be confirmed by Rana et al. (2018), it would be interesting to see whether the presented results are also confirmed using corresponding methods for polarization such as Chingangbam et al. (2017).

and $B$-modes, their relation to principles in current foreground separation algorithms were shown.

In light of the increasingly precise measurements at microwave frequencies performed for the observation of the CMB, an equally precise understanding of the behavior of those sources interfering with a clean measurement is required. Given that foreground separation algorithms and the subsequent inclusion of the CMB products in a combined framework for determining the cosmological parameters focus on the less contaminated regions of the sky, away from the Galactic plane, these results will need to be taken into account in further analyses. In other words, the supposedly cleanest regions of the sky might contain the most stubborn foregrounds.

CHAPTER 5

# $E$- and $B$-mode decomposition on partial skies

Unveiling the polarized CMB is significantly more difficult than it is in temperature. The preceding chapter already hinted towards complications also arising through differences in the foreground emission in $E$- and $B$-modes, suggesting separate analyses for these modes. However, separation of a polarized signal on the celestial sphere into $E$- and $B$-modes requires the knowledge of the polarized signal across the entire sky, whereas regions of strong Galactic emission are commonly masked out. This introduces the topic of the final chapter of my thesis: The problem of decomposing polarized signals into $E$- and $B$-modes from only a fraction of the sky, or, more specifically, a method for the correction of a failed decomposition.

On an incomplete sky map, a standard separation of a polarized signal into $E$- and $B$-modes is accompanied by "leakage" (the so-called $EB$ leakage). In the case of the CMB, especially the resulting $B$ map get strongly contaminated (Lewis et al., 2002; Bunn et al., 2003). This kind of leakage must be carefully corrected to reach forecasted $B$-mode targets. One way to study the $EB$ leakage due to incomplete sky coverage is by constructing localized estimators that are informed of the mask or window function defined on the sky fraction in question, as was first proposed by Bunn et al. (2003), and subsequently used in many such studies, e.g. Lewis (2003); Bunn (2003); Zaldarriaga (2004); Zhao and Baskaran (2010); Smith (2006); Smith and Zaldarriaga (2007). Commonly such estimators are referred to as "pure" $E/B$-modes, and with their help corrected $E$ - and $B$-mode *power spectra* could be produced. However, corrected *maps* of the standard $E$- and $B$-modes could, so far, not be reconstructed. The advantages of such a solution would be enormous. I will discuss some of them below, and for now mention localized contamination of, of course, Galactic foregrounds, which would otherwise perhaps go unnoticed in a pure power-spectrum-based approach.

In this chapter, two methods for correcting of the $EB$ leakage directly on CMB maps are introduced. As opposed to the methods mentioned above, only the standard, full-sky definitions of $E$- and $B$-modes are used. The first method is motivated by studying properties of the leakage at the mask's boundary. It works well for removing larger scale features, but due to its simple construction is unable to infer information from smaller scales. The second, and main method is formulated in terms of the a new sort of $EB$ decomposition (Liu et al., 2018; Rotti and Huffenberger, 2018), mentioned in Section 1.1.4 which will be briefly reviewed here. Under certain approximations, valid for the CMB, one is able to "simulate" the leaked signal and henceforth correct for it.

In the course of a short introduction, the first method is presented in Section 5.1. Section 5.2 presents the main method, in theory and in preliminary application, to be extended to quantitative studies in Section 5.3. I conclude in Section 5.4.

*The content of this chapter is based on Liu et al. (2018).*

## 5.1 Background

Before discussing polarization fields, I begin with a brief example involving only scalar fields. Obtaining estimates of spherical harmonic coefficients on a masked sky already here illustrates the difficulties arising in polarization. For a full-sky map, Equation 1.27 delivers the corresponding harmonic coefficients. The signal, which here should be called $f(\hat{n})$, could be windowed (or masked), such that only a part of it is available. The coefficients $a_{\ell m}$ change correspondingly, and since they now do not (only) describe the signal $f$ anymore, they are referred to as pseudo-$a_{\ell m}$s:

$$\widetilde{a}_{\ell m} = \int f(\hat{n}) W(\hat{n}) Y^*_{\ell m}(\hat{n})\, \mathrm{d}\hat{n}, \tag{5.1}$$

where $W(\hat{n})$ is the window function. By expanding out $f$ in terms of its actual spherical harmonic coefficients, $a_{\ell m}$ gives

$$\widetilde{a}_{\ell m} = \sum_{\ell' m'} a_{\ell' m'} \int Y_{\ell' m'} W(\hat{n}) Y^*_{\ell m}(\hat{n})\, \mathrm{d}\hat{n}, \equiv a_{\ell' m'}\, \mathsf{M}_{\ell' m' \ell m}, \tag{5.2}$$

where I introduced the coupling matrix $\mathsf{M}$. Equivalently one can introduce the pseudo-$C_\ell$s as

$$\widetilde{C}_\ell = \frac{1}{2\ell+1}\sum_m |a_{\ell' m'}\mathsf{M}_{\ell' m' \ell m}|^2 \,. \tag{5.3}$$

Reconstructing the real $a_{\ell m}$s (or the real $C_\ell$s) therefore is obviously an inverse problem, and most methods attempting to solve this must consider specific regularizing conditions. One such method is the "Monte Carlo Apodized Spherical Transform Estimator" (MASTER, Hivon et al. (2002)), which shall be used later on in this chapter.

In polarization the situation worsens. First worked out by Lewis et al. (2002) and Bunn et al. (2003), one finds that defininining $E$- and $B$-modes on the full sky, yields two orthogonal fields which together completely describe any polarization field; this is not the case on an incomplete sky. There, the obtained $E$- and $B$-modes are still orthogonal to each other, but a third subspace, which in turn is orthogonal to both, is defined to cover the space of polarization fields. This third component is dubbed the ambiguous mode. The $E$- and $B$-modes of the incomplete sky, are now called *pure* modes. However, the pure modes need not (and in the case of a partial sky will not) equal the *true* modes. Also here, techniques have to be developed to assign the power of the ambiguous mode (the leakage) back to the mode it came from, in order to find good estimates of the true $E$ and $B$ fields.

In Bunn (2011), it was shown that the ambiguous mode $\psi$ satisfies the spherical bi-Laplacian equation

$$\nabla^2(\nabla^2+2)\psi = 0, \tag{5.4}$$

subject to homogeneous Neumann and Dirichlet boundary conditions at the edge of the known region. Seemingly more complicated that for the temperature case, there is a way to find an easy solution to correcting the leakage, at least for the case of the CMB.

Assuming that the power in the $E$-mode dominates the power in the $B$-mode, the purified $B$-mode, calculated by removing the ambiguous mode $\psi$ from the corrupted $B$-mode, is a good approximation to the true $B$-mode. One simplified approach to this would be to replace the bi-Laplacian equation by the Laplacian equation and neglecting the Neumann boundary conditions.[1] In this case, a simple numerical solution is the relaxation method.

It was shown by Kim and Naselsky (2010) that the $EB$ leakage is most significant at the edge of the mask, which naturally provides a reliable boundary condition. Therefore, it is tempting to solve the $EB$ leakage $\nabla^2\psi = 0$ for the leakage term $\psi$, by a relaxation method,

[1] The solutions of the simplified Laplacian problem retain the basic large-scale structure of the bi-Laplacian solutions, however, small-scale structures can be neglected.

and by using the corrupted signal at the boundary as the boundary constraint. Here, this is implemented by diffusive inpainting (Planck 2013 Results. XXIV; Planck 2015 results. XVII), in which sky pixels are iteratively replaced by the average of their neighbors, except for the pixels on the boundary.

Therefore, I introduce the first (and mainly illustrative) method as follows:

1. Begin with the corrupted $B$ map derived from a masked sky.
2. Set all pixels on the sky to zero except those at the edge of the valid region, which constitute the boundary condition.
3. Perform diffusive inpainting on the valid sky as mentioned above using the boundary condition in step 2. On convergence, the result can be taken as a template for the $EB$ leakage.
4. Subtract the derived template from the corrupted $B$ map in order to arrive at the corrected $B$ map.

The results of this procedure, performed on simulations, is shown along with the results of the main method of this chapter, in Section 5.2.3. A more quantitative test is performed in Section 5.3.3.

## 5.2 A new method for $E/B$ leakage correction

The method to be proposed here can be understood following a recent suggestion for an $E/B$ decomposition of Stokes $Q$ and $U$ maps (Draine and Lazarian, 1999; Rotti and Huffenberger, 2018). There, each of the Stokes $Q$ and $U$ parameters is dissected into its part which would contribute to $E$- or $B$-modes in a regular decomposition. I therefore first review essentials of this technique, and derive a few new relations. In addition, I hope not to confuse the reader by using the terms $E$- and $B$-mode both for the modes as defined in Equations 1.40, and those parts of the Stokes parameters, which contribute to the former. I first briefly review the proposed decompositions by Liu et al. (2018) and derive additional identities. (Out of personal taste, I choose a different notation.) Then, the proposed method is formulated out and finally applied to data.

### 5.2.1 Collecting $E$ and $B$ modes in the Stokes parameters

Instead of combining the Stokes parameters $Q$ and $U$ to form signals $E$ and $B$, as discussed in Section 1.1.4, one could also attempt the decomposition respectively on $Q$ and $U$. For example,

a $Q$ map alone would be decomposed into $Q_E$ and $Q_B$, its $E$ and $B$ contributions. Denoting $\mathbf{P}(\hat{n}) \equiv (Q(\hat{n}), U(\hat{n}))$, one can write

$$\mathbf{P}(\hat{n}) = \mathbf{P}_E(\hat{n}) + \mathbf{P}_B(\hat{n}), \tag{5.5}$$

with the hopefully obvious notation $\mathbf{P}_X = (Q_X, U_X)$. Such a decomposition can be written as

$$\begin{aligned} \mathbf{P}_E(\hat{n}) &= \int \mathsf{G}_E(\hat{n}, \hat{n}')\, \mathbf{P}(\hat{n}')\, \mathrm{d}\hat{n}' \\ \mathbf{P}_B(\hat{n}) &= \int \mathsf{G}_B(\hat{n}, \hat{n}')\, \mathbf{P}(\hat{n}')\, \mathrm{d}\hat{n}' \end{aligned} \tag{5.6}$$

where the $2 \times 2$ coupling matrices $\mathsf{G}_{E/B}$ are defined as:

$$\begin{aligned} \mathsf{G}_E(\hat{n}, \hat{n}') &\equiv \frac{1}{2}\delta(\hat{n} - \hat{n}') I_{2\times 2} + \mathsf{G}(\hat{n}, \hat{n}'), \\ \mathsf{G}_B(\hat{n}, \hat{n}') &\equiv \frac{1}{2}\delta(\hat{n} - \hat{n}') I_{2\times 2} - \mathsf{G}(\hat{n}, \hat{n}'), \end{aligned} \tag{5.7}$$

and

$$\mathsf{G}(\hat{n}, \hat{n}') \equiv \begin{pmatrix} g_+(\hat{n}, \hat{n}') & -i\, g_-(\hat{n}, \hat{n}') \\ -i g_-(\hat{n}, \hat{n}') & g_+(\hat{n}, \hat{n}') \end{pmatrix}, \tag{5.8}$$

$$g(\hat{n}, \hat{n}') \equiv \frac{1}{4} \sum_{\ell m} \left[ {}_{+2}Y_{\ell m}(\hat{n})\, {}_{-2}Y^*_{\ell m}(\hat{n}') \pm {}_{-2}Y_{\ell m}(\hat{n})\, {}_{+2}Y^*_{\ell m}(\hat{n}') \right]. \tag{5.9}$$

Equations 5.7 further imply the relation

$$\mathsf{G} = \frac{1}{2} \left( \mathsf{G}_E - \mathsf{G}_B \right). \tag{5.10}$$

In practice, this decomposition is conveniently calculated by converting $Q$ and $U$ into $E$ and $B$, setting the $E$ (or $B$) map to zero, and converting back to $Q$ and $U$, which now only contain the $B$ (or $E$) contribution. Yet, the formulation in terms of Equations 5.6 – 5.9 can be helpful in understanding the framework.

Below, I will write out a list of useful identities for above quantities.

**Expanding the polarization vectors $\mathbf{P}(\hat{n})$** Applying Equation 5.5 to Equations 5.6, one finds

$$\begin{aligned}\mathbf{P}_E(\hat{n}) &= \int \mathsf{G}_E(\hat{n},\hat{n}')\ (\mathbf{P}_E(\hat{n}') + \mathbf{P}_B(\hat{n}'))\ \mathrm{d}\hat{n}' \\ \mathbf{P}_B(\hat{n}) &= \int \mathsf{G}_B(\hat{n},\hat{n}')\ (\mathbf{P}_E(\hat{n}') + \mathbf{P}_B(\hat{n}'))\ \mathrm{d}\hat{n}'\end{aligned} \tag{5.11}$$

and therewith

$$\begin{aligned}\int \mathsf{G}_E(\hat{n},\hat{n}')\,\mathbf{P}_B(\hat{n}')\,\mathrm{d}\hat{n}' &= 0 \\ \int \mathsf{G}_B(\hat{n},\hat{n}')\,\mathbf{P}_E(\hat{n}')\,\mathrm{d}\hat{n}' &= 0\end{aligned} \tag{5.12}$$

**Expanding the coupling matrix $\mathsf{G}(\hat{n},\hat{n}')$** Applying Equation 5.10 and 5.5 to Equation 5.6, leads to

$$\int \mathsf{G}(\hat{n},\hat{n}')\,\mathbf{P}(\hat{n}')\,\mathrm{d}\hat{n}' = \frac{1}{2}\left(\mathbf{P}_E - \mathbf{P}_B\right), \tag{5.13}$$

and in particular

$$\begin{aligned}\int \mathsf{G}(\hat{n},\hat{n}')\,\mathbf{P}_E(\hat{n}')\,\mathrm{d}\hat{n}' &= \frac{1}{2}\mathbf{P}_E(\hat{n}), \\ \int \mathsf{G}(\hat{n},\hat{n}')\,\mathbf{P}_E(\hat{n}')\,\mathrm{d}\hat{n}' &= -\frac{1}{2}\mathbf{P}_B(\hat{n}).\end{aligned} \tag{5.14}$$

**Expanding the integral into two regions** In the Section 5, it shall become clear why it can be informative to split up the integrals of Equations 5.12 into two complementary parts (named region "1" and region "2", as will be done in Equation 5.16). For now, I just show which conclusion one can draw from it:

$$\begin{aligned}\int_1 \mathsf{G}_E(\hat{n},\hat{n}')\,\mathbf{P}_B(\hat{n}')\,\mathrm{d}\hat{n}' &= -\int_2 \mathsf{G}_E(\hat{n},\hat{n}')\,\mathbf{P}_B(\hat{n}')\,\mathrm{d}\hat{n}' \\ \int_1 \mathsf{G}_B(\hat{n},\hat{n}')\,\mathbf{P}_E(\hat{n}')\,\mathrm{d}\hat{n}' &= -\int_2 \mathsf{G}_B(\hat{n},\hat{n}')\,\mathbf{P}_E(\hat{n}')\,\mathrm{d}\hat{n}'\end{aligned} \tag{5.15}$$

Just as the regular $E/B$ decomposition, also this decomposition works impeccable, if the whole sky is available. However, if masked, the generated signal on the available part of the sky gets corrupted — since it misses information from outside (this shall underline the non-local

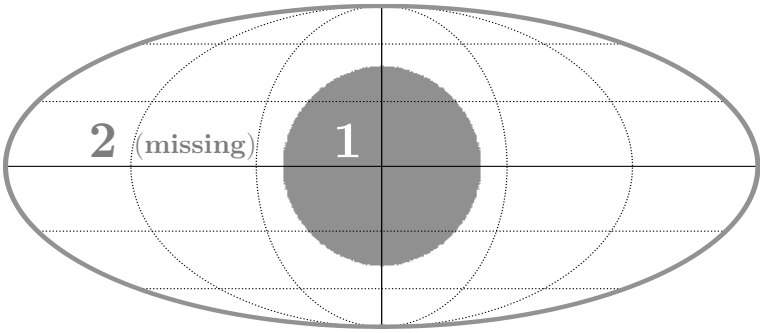


Figure 5.1 Sketch of a map with two separate regions, the available zone "1" and region "2" which is masked out/unorbserved.

definition of the $E$- and $B$-modes), and connected with that, since the two modes on the sky are mixed. This shall made quantitative via a simple, but realistic example.

### 5.2.2 Formulating the method

Consider a sky map, divided into two regions as shown in Figure 5.1. "1" denotes the available region and "2" marks the region which is masked out. On the full sky, the $E$-mode (or $B$-mode) polarization vector is compute via Equation 5.6. Note that the considered mask is *not* apodized. This enables one to simply split the integral of 5.6 into two parts, each of which corresponds to the available or masked part of the sky, as exemplified by the $E$-mode:

$$\mathbf{P}_E(\hat{n}) = \int_1 \mathsf{G}_E(\hat{n},\hat{n}')\,\mathbf{P}(\hat{n}')\,\mathrm{d}\hat{n}' + \int_2 \mathsf{G}_E(\hat{n},\hat{n}')\,\mathbf{P}(\hat{n}')\,\mathrm{d}\hat{n}' \tag{5.16}$$

Due to the mask, the signal in region "2" is set zero, wherefore the second term vanishes; the polarization vector only receives contribution from region "1". In other words, the partial-sky estimate of $\mathbf{P}_E$, which will be denoted $\widetilde{\mathbf{P}}_E$ (in reference to the Pseudo-$a_{\ell m}$s and Pseudo-$C_\ell$s of the previous section), will be biased by a lacking contribution which *should have* been given by the signals in region "2":

$$\begin{aligned}\widetilde{\mathbf{P}}_E(\hat{n}) &\equiv \int_1 \mathsf{G}_E(\hat{n},\hat{n}')\,\mathbf{P}(\hat{n}')\,\mathrm{d}\hat{n}' = \\ &= \int_1 \mathsf{G}_E(\hat{n},\hat{n}')\,\left(\mathbf{P}_E(\hat{n}') + \mathbf{P}_B(\hat{n}')\right)\,\mathrm{d}\hat{n}'.\end{aligned} \tag{5.17}$$

Two realization were made. Firstly, it is obvious that the "pseudo" signal $\widetilde{\mathbf{P}}_E(\hat{n}) \neq \mathbf{P}_E(\hat{n})$ by exactly the second term of Equation 5.16, and secondly, in the second line, one sees that the $E$-mode signal also receives contribution from the $B$-modes. In the previous section, and

identity of Equation 5.15 showed that, if both regions of the sky had been available, the $B$-mode contributions from region "1" and "2" would have cancelled. Now, that "2" is unknown, one is left with the so-called $B$-to-$E$ leakage.

The same holds also for the $B$-mode polarization vector, where the corrupted component reads

$$\widetilde{\mathbf{P}}_B(\hat{n}) \equiv \int_1 \mathsf{G}_B(\hat{n},\hat{n}')\,\mathbf{P}(\hat{n}')\,\mathrm{d}\hat{n}' = \tag{5.18}$$

$$= \int_1 \mathsf{G}_B(\hat{n},\hat{n}')\,\left(\mathbf{P}_E(\hat{n}')+\mathbf{P}_B(\hat{n}')\right)\,\mathrm{d}\hat{n}'. \tag{5.19}$$

The true $B$-mode differs from the corrupted one by the term

$$\int_2 \mathsf{G}_B(\hat{n},\hat{n}')\,\mathbf{P}(\hat{n}')\,\mathrm{d}\hat{n}', \tag{5.20}$$

Of particular interest is any signal in region "1" (or $R_1$). Indeed, one can convince oneself that, within $R_1$, the $E$-to-$B$ leakage equals the $B$-to-$E$ leakage (up to a sign), by applying Equation 5.7 to the respective leakages:

$$\begin{aligned}\int_2 \mathsf{G}_E(\hat{n},\hat{n}')\,\mathbf{P}(\hat{n}')\,\mathrm{d}\hat{n}' &= \frac{1}{2}\int_2 \delta(\hat{n}-\hat{n}')\,\mathbf{P}(\hat{n}')\,\mathrm{d}\hat{n}' + \int_2 \mathsf{G}(\hat{n},\hat{n}')\,\mathbf{P}(\hat{n}')\,\mathrm{d}\hat{n}' \\ &= +\int_2 \mathsf{G}(\hat{n},\hat{n}')\,\mathbf{P}(\hat{n}')\,\mathrm{d}\hat{n}' \qquad , \quad \forall \hat{n}\in R_1\end{aligned} \tag{5.21}$$

$$\begin{aligned}\int_2 \mathsf{G}_B(\hat{n},\hat{n}')\,\mathbf{P}(\hat{n}')\,\mathrm{d}\hat{n}' &= \frac{1}{2}\int_2 \delta(\hat{n}-\hat{n}')\,\mathbf{P}(\hat{n}')\,\mathrm{d}\hat{n}' - \int_2 \mathsf{G}(\hat{n},\hat{n}')\,\mathbf{P}(\hat{n}')\,\mathrm{d}\hat{n}' \\ &= -\int_2 \mathsf{G}(\hat{n},\hat{n}')\,\mathbf{P}(\hat{n}')\,\mathrm{d}\hat{n}' \qquad , \quad \forall \hat{n}\in R_1\end{aligned} \tag{5.22}$$

In the following, $L(\hat{n}) \equiv -\int_2 \mathsf{G}(\hat{n},\hat{n}')\,\mathbf{P}(\hat{n}')\,\mathrm{d}\hat{n}$ should be referred to as the "leakage" term. The signal contributing to this leakage stems from region "2". Since this signal is unavailable (it was masked out), the goal of this section is to find a good replacement — a template, resembling the leakage term, yet constructed from region "1" signal only.

As seen before, the CMB $E$-mode is much more pronounced than its $B$-mode. For any such partial-sky $E/B$ decomposition the $E$-to-$B$ leakage is dominant. It is this fact which is made use of in approximating the leakage term. The idea is the following. Since the $B$-to-$E$ leakage is assumed to be negligible, the corrupted polarization vector $\widetilde{\mathbf{P}}_E(\hat{n})$ can be thought of as similar enough to the real (and unknown) vector $\mathbf{P}_E(\hat{n})$, such that the $E$-to-$B$ leakage would look similar to the leakage from the corrupted $E$-mode to its $B$-mode if the same decomposition was

attempted again. In other words,

$$l(\hat{n}) \equiv \int_1 \mathsf{G}_B(\hat{n},\hat{n}')\,\widetilde{\mathbf{P}}_E(\hat{n}')\,\mathrm{d}\hat{n}' = \int_1 \mathsf{G}_B\left[\int_1 \mathsf{G}_E(\hat{n}',\hat{n}'')\,\mathbf{P}(\hat{n}'')\,\mathrm{d}\hat{n}''\right]\mathrm{d}\hat{n}' \;\propto\; L(\hat{n}). \tag{5.23}$$

Note that in the outer integral the *same* region was selected, i.e. the same mask, as when calculating $\widetilde{\mathbf{P}}_E$. In particular, under approximation $\mathbf{P}_E \gg \mathbf{P}_B$ one finds $l \approx \frac{1}{2}L$.

The procedure for this method simply goes as follows:

1. Begin with the masked $(Q,U)$ and decompose it into $(Q_E,U_E)'$ and $(Q_B,U_B)'$.
2. Apply the same mask on $(Q_E,U_E)'$ and calculate $(Q_B,U_B)''$.
3. Within the mask, or region "1", $(Q_B,U_B)''$ is the template for the $EB$ leakage. Use it to remove the $EB$ leakage from $(Q_B,U_B)'$ by linear fitting.

I only described the method and the procedure in terms of the $E$ and $B$ polarization vectors. Note that while it is necessary to do step 1 in the way described, starting from step 2, one is free to proceed in terms of the actual $B$-modes, and arrive at a $B$ map as a template; both give similar results. For power spectrum estimation, however, the $B$ map template gives slightly better results (about 10% lower error). For correcting the morphology of the corrupted map in the pixel domain, the variant with $(Q_B,U_B)''$ is slightly better. Since below I will eventually compute power spectra, all pixel domain results will be presented in the form of $B$ maps.

### 5.2.3 Examples and comparison

I now present examples of correcting the $EB$ leakage for simulated CMB maps via the method of the previous section, along with those using the simple method of section 5.1. I refer to the simple method as "method 1" and that of the last section as "method 2". The methods are demonstrated by using two different masks (a belt, and a disk mask), shown in Figures 5.2 and 5.3, and a single CMB simulation with $r = 0.05$, taken from *Planck*'s FFP9 suite.

I begin by describing the results in Figure 5.2. The mask was defined to be 20° in width and 2° in height. The two methods give similar leakage templates, and additionally reproduce the real leakage term well. As a measure of similarity, I compute the cross correlation between the real $B$ map and the contaminated one to be only 20%, whereas after correction, the $B$ map corrected by method 1 gives 86% correlation with the real $B$ map, and that of method 2, 66%. While method 1 leads to better correction on larger scales, method 2 captures the small scale

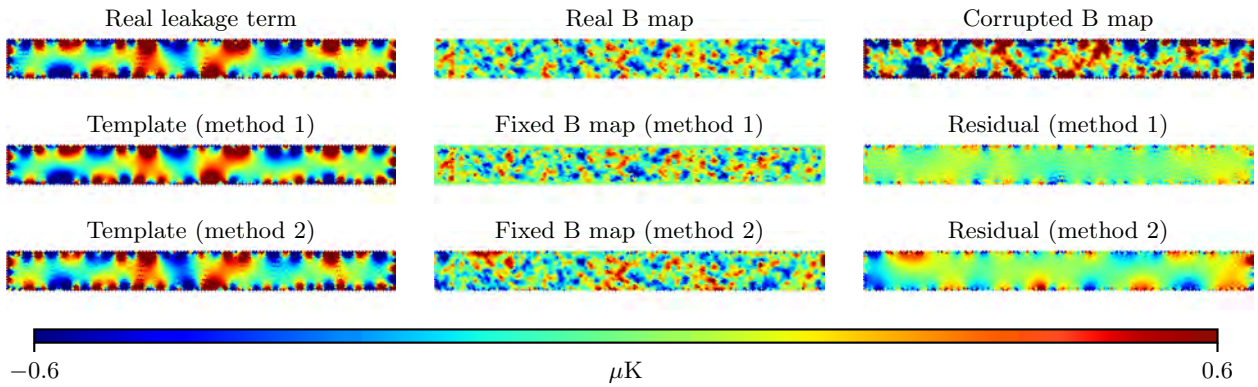


Figure 5.2 Examples of pixel domain $EB$ leakage corrections with a $r = 0.05$ simulation. The mask is 20° wide and 2° high.

leakage better, as can be seen in the right panels of rows 2 and 3. While it was expected that method 1 catches the large scales, it is surprising to see that it outperforms method 2!

I then repeat this test by instead using a disk-shaped region with 20° radius as shown in Figure 5.3. This time, the cross correlation between the real $B$ map and the contaminated one is 70%, whereas after correction, method 1 leads to 97.7% correlation of the fixed $B$ map with the real one, and that of method 2 gives 97.6%, in strong agreement with one another, as well as with the real $B$ map.[2] Given the small fraction of the edge area in comparison to the whole region, the cross correlations are only marginally influenced by the edge, especially after correction. A glance at the figures makes clear that most of the interior of the map is significantly contaminated, which is captured well by both templates.

It was seen that, method 1 can perform better in the case of narrow regions, where the edge condition becomes relatively more important. In Section 5.3.3 another comparison between the methods is made, which will show that method 2 gives relatively smaller error at the desired multipole range, whereas method 1 mainly involves the correction of the large-scale features (see also the smoothness of the template by method 1 in Figure 5.2). Therefore, in all other sections method 2 will be taken as the default.

[2]Note that the listed cross correlation values each are associated with a given mask, and are not comparable across masks.

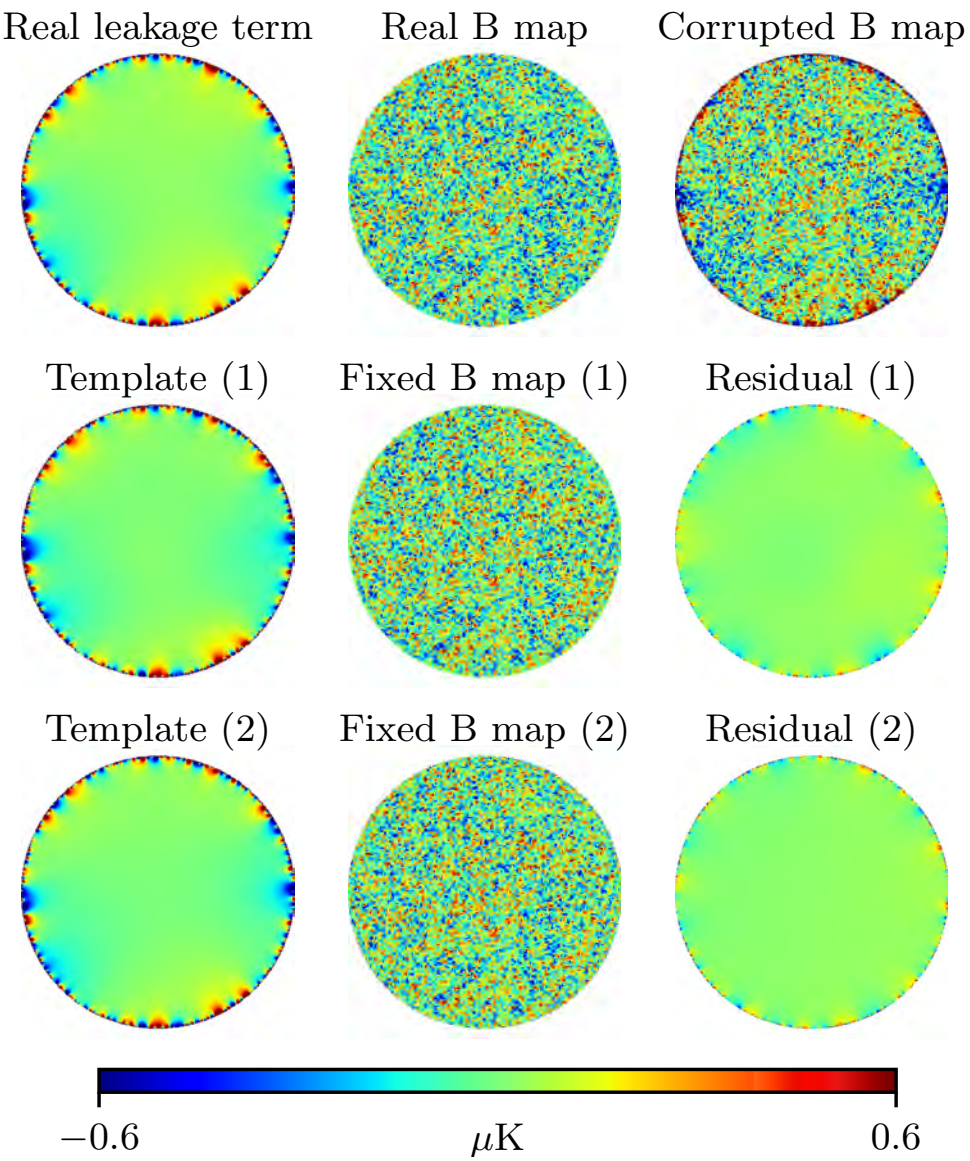


Figure 5.3 Same as Figure 5.2 but for a disk mask with 20° radius.

### 5.2.4 Advantages of correction in pixel domain

Concluding this section, I summarize the advantages a correction of $EB$ leakage in the pixel domain has over conventional methods that only recover the $EE$ and $BB$ power spectra.

- Both methods 1 and 2 operate only in the pixel domain without involving the power spectrum, i.e., they are independent of assumptions on the, e.g. $B$-mode angular power spectrum, and therefore should be considered an *additional* contribution to existing polarized power spectrum reconstruction methods.

- Another important advantage of pixel domain correction is that it is very easy to deal with noise, because there noise and CMB are added linearly, and the proposed correction methods are also linear.

- Since the $EB$ leakage has already been corrected in the pixel domain, the challenge to arrive at an estimation of the $E$- or $B$-mode power spectrum simplifies to estimating the angular power spectrum of a *scalar* field given a mask. This problem has been intensively studied by many authors, e.g., Tegmark (1997); Hivon et al. (2002); Efstathiou (2004); Jewell et al. (2004); Polenta et al. (2005); Saha et al. (2006); Abrial et al. (2008); Inoue et al. (2008); Gruppuso et al. (2009); Jewell et al. (2009); Zacchei et al. (2011); Kim et al. (2012); Starck et al. (2013); Molinari et al. (2014). This idea will be implemented in Section 5.3.2, gives excellent reconstruction results.

- As was seen, neither method 1 nor 2 requires any apodization of the mask; they work simply with a top-hat mask. One is thus free to choose any *posterior* apodization scheme to improve the $B$-mode angular power spectrum estimation. This will be presented in Section 5.3.3.

## 5.3 Testing the level of residual after correction

Even with perfect $EB$ leakage correction, the $B$-mode spectrum obtained from the cut sky is still different from the known full-sky spectrum, due to sampling uncertainty (among others). To focus on the effectiveness of the present methods, in this section, I show results of tests that measure which uncertainties to expect in $B$-mode power spectra *only* from the contribution of the $EB$ leakage or its correction. For all tests a disk-shaped sky region of about 47° radius will be investigated, which covers roughly 15% of the sky. This choice was made, again, with reference to one of the specifications of the GreenPol experiment.

First, in Section 5.3.1, I perform test run on a maps with zero $B$-mode. Subsequently simulations with non-zero $B$-modes are investigated and compared to those obtained from using a state-of-the-art implementation of MASTER (Section 5.3.2). Lastly, I illustrate how to further optimize these results by different choices of posterior apodization (Section 5.3.3).

### 5.3.1 Zero initial B-mode

I begin with an idealistic test, in which I select a single simulated CMB map without noise, and manually set the input $B$-mode to zero. This automatically marks any detection of a derived $B$-mode signal — either before or after correction — to be due to leakage or residual leakage. After masking, an $E/B$ decomposition is attempted and the resulting leakage from the corrupted $B$ map is removed by method 1. I compare this to a case where no correction has been done to the corrupted maps. The final output $B$-mode spectra are then calculated directly from the masked maps, in two ways: once where the maps were apodized with a Tukey window with a taper fraction of 0.1,[3] and once where they were not. Those that were apodized were rescaled such that the spectra are comparable. These spectra correspond to pseudo-spectra and, as mentioned before, are sufficient for highlighting the advantages of our method, without including sample uncertainties. As pointed out by Bunn et al. (2003), oversampling can help to reduce the leakage due to pixelization, thus I use $N_{\mathrm{Side}} = 2048$ in this test, and show the results in Figure 5.4. In the upper panels it can be seen that the leakage from $E$- to $B$-modes is removed almost completely. (I amplify the residuals by a factor of 10 to make them visible.) In the bottom panel I show the angular power spectra of the residual leakages before (*red*) and after (*blue*) correction. One can see that those whose maps were apodized (*dashed lines*) generally give better results than those which were not (*solid lines*). The corrected and apodized spectrum gives the best result, which lies up to 12 orders of magnitude below the input $EE$ spectrum. The other variants are either worse at large scales (the corrupted $BB$ spectra), or worse at small scales (without posterior apodization), or both. I already here refer to Section 5.3.3, where this result is further improved by about two orders of magnitude by optimizing the apodization.

### 5.3.2 Combination with the MASTER method

I now extend above test, in which only $BB$ pseudo-spectra were considered, to the reconstruction of full $B$-mode spectra. A widely used algorithm to reconstruct an unbiased full-sky

[3] This roughly corresponds to an apodization length of 5°. In Section 5.3.3 present results of applying different window functions for apodization, including the one used here.

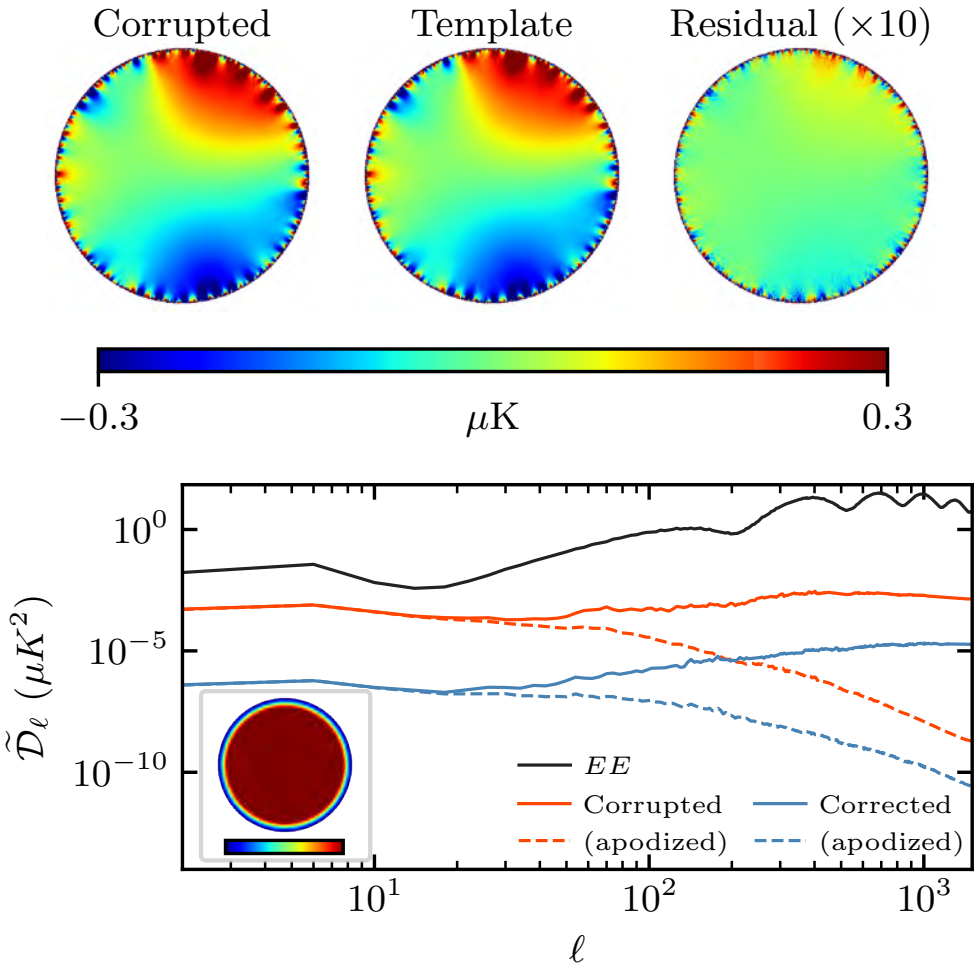


Figure 5.4 Maps and power spectra after $EB$ leakage correction when the input $B$-mode is zero. *Upper panels:* The corrupted $B$-mode (*left*), the template generated by method 2 (*middle*), and the residual leakage after correction (multiplied by 10; *right*). *Lower panel:* Comparison of the $EE$ pseudo-spectrum, and the residual $BB$ pseudo-spectra (both binned with $\Delta\ell = 4$) derived from either corrupted or corrected $B$ maps, using either the mask (*solid*) or apodization shown in the inset (*dashed*).

angular power spectrum from the cut sky is the MASTER method (Hivon et al., 2002). Pixel domain $EB$ leakage correction can be easily combined with the MASTER method (or any other pseudo-$C_\ell$ method) as described below. The simulations in use here are $N_{\rm Side} = 256$ simulations with $r = 0.1$, including lensing.

I employ the Python package, PYMASTER, of the NaMaster code (Alonso et al., 2018; Alonso et al.) as an implementation of the MASTER method to reconstruct the full-sky $BB$ spectrum by two ways for comparison: one is by using NaMaster with a built-in purifying (Smith, 2006) option for the $B$-mode, whose results are denoted $B^i_{\rm pure}(\ell)$ for 100 different CMB simulations $i$, and will in the following be referred to as "MASTER+PURE"; and the second is to first correct the $B$-mode map by method 2, and subsequently use NaMaster in the *non-polarized* mode to reconstruct the full-sky $BB$ spectrum from the corrected $B$ map as $B^i_{\rm m2}(\ell)$. Lastly, I run MASTER on the *real* $B$ map for each simulation masked with the same apodization to provide a reference $B^i_{\rm ref}(\ell)$.

Recall that there are two errors involved: The sampling uncertainty due to a reduced sky fraction and the ignorance towards what lies below the mask, and the error in the $B$ mode map even after correction. Only comparing to a spectrum, which misses the same information, helps skip the sampling uncertainty and focus only on the error of $EB$ leakage correction. For each simulation I calculate the difference between each of its reconstructions and the reference; the corresponding RMS reads:

$$\Delta B^i_{\rm pure/m2}(\ell) = B^i_{\rm pure/m2}(\ell) - B^i_{\rm ref}(\ell); \tag{5.24}$$

$$\Delta B_{\rm pure/m2}(\ell) = \sqrt{\frac{1}{N_{sim}} \sum_{i=1}^{N_{sim}} [\Delta B^i_{\rm pure/m2}(\ell)]^2}, \tag{5.25}$$

Both $\Delta B_{\rm pure}(\ell)$ and $\Delta B_{\rm m2}(\ell)$ are shown in Figure 5.5. One can see that, on average, and under all the same conditions (resolution, sky region, and apodization), method 2 helps to reduce the error of reconstruction by 2–3 orders of magnitude at higher $\ell$ compared to the MASTER and "pure" scheme. The latter gives leakage correction uncertainties roughly at the level of $r \approx 10^{-2}$, whereas, by an improvement of 2–3 orders of magnitude, the method proposed here ensures that the $EB$ leakage is corrected down to a level of $r \approx 10^{-4}$ or even lower. I should emphasize again, that this statement holds *only* for uncertainties arising from $EB$ leakage. Other issues such as sufficient foreground removal, noise, delensing, sampling uncertainties, etc., provide additional sources of error.

In these calculations the 'C1' apodization from NaMaster was used, without any optimization for our method. As shall be seen in the following section, additional optimization for

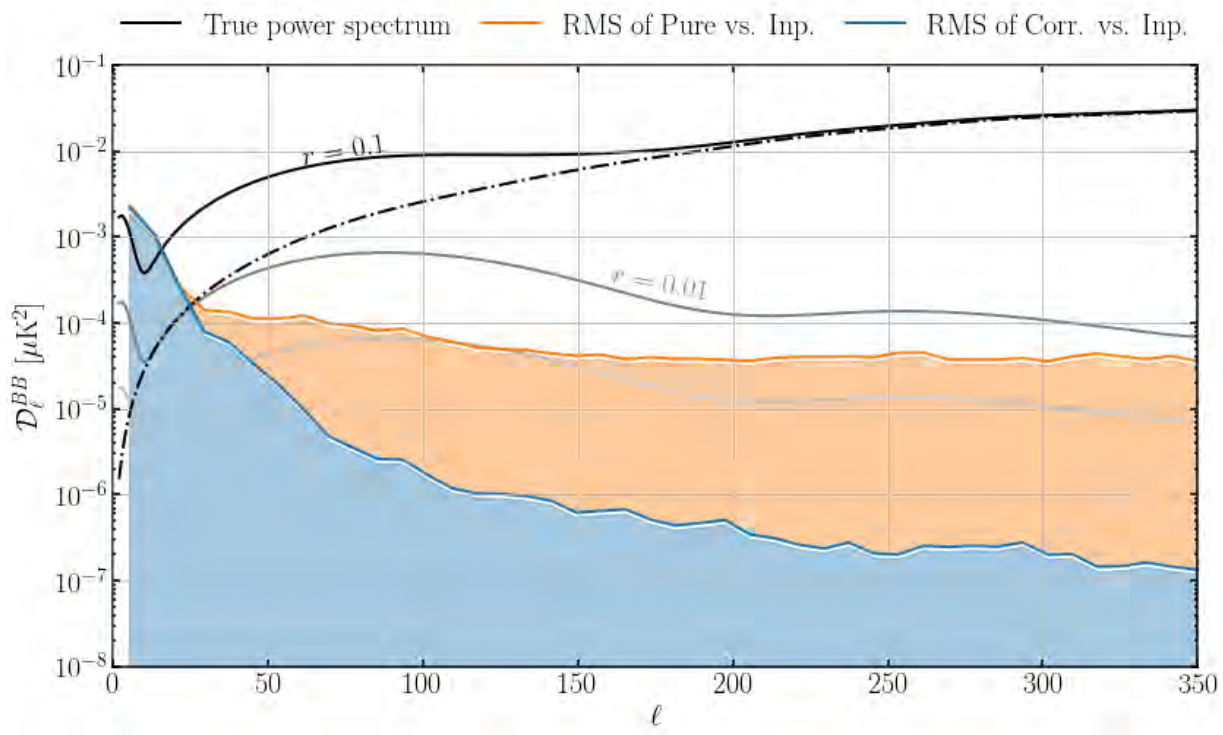


Figure 5.5 Comparison of the errors of $EB$ leakage correction: $\Delta B_{\text{pure}}(\ell)$ is shown in orange, and $\Delta B_{\text{m2}}(\ell)$ is shown in blue, cf. Equation 5.24 and Section 5.3.2 for details. The expected primordial $B$-mode spectra for $r \sim 10^{-1}$–$10^{-3}$ and the lensing $B$-mode spectrum are also plotted for comparison. The input spectrum in shown as the black solid line.

the window function can further improve the results by orders of magnitude, which may allow for even lower $r$. Also note that, as stated before, a higher resolution than $N_{\text{Side}} = 256$, used here, could decrease the uncertainties of this method further.

### 5.3.3 Optimization of the posterior pixel domain apodization

It is already known from Figures 5.2–5.4 that the residual $EB$ leakage after correction is most significant at the edge of the available sky region, and it therefore can be further suppressed by applying a posterior apodization/window function, where "posterior" means that the apodization is applied independently of and after the pixel domain $EB$ leakage correction. Naturally, a more aggressive apodization gives further suppression of the residual leakage, but at the same time, the overall signal strength is reduced. In this section different window functions are tested to show how to find a balance between higher signal and lower residual. I use the same mask as in the two previous subsections. Here, however, *Planck* FFP9 simulations are used.

Given a symmetric one-dimensional window function defined on the unit interval, $w(x)$,

where $0 \leq x \leq 1$, its corresponding two-dimensional window function can be constructed on the available region by

$$W(n) = w\left(\frac{d(n)}{2d_{\max}}\right), \tag{5.26}$$

where $d(n)$ is the distance from the $n$th pixel to the edge of the mask, and $d_{\max}$ is the maximum such distance over all pixels in the available region. This ensures that the pixel domain window function is 0 at the edge and 1 at the points that are most distant to the edge. The types of $w(x)$ are chosen from the following (the abbreviations in brackets are to be used in Figure 5.6):

- Hamming (ha) and Tukey windows with taper fractions in increments of 0.1 (tu0.1, etc.) (Harris, 1978)
- Bartlett window (ba) (Gautam et al., 1996)
- Nuttall window (nu) (Nuttall, 1981)
- Exact Blackman window (bl) (Blackman and Tukey, 1958; Harris, 1978)

Note that the Tukey window is also known as the tapered cosine window; the conventional cosine window, also known as the Hann window, is recovered with a taper fraction of 1.0 ("tu1.0").

To evaluate the aggressiveness of each window function, one can calculate

$$f_W = \frac{1}{N}\sum_{n=1}^{N} W^2(n) \tag{5.27}$$

where $N$ is the total number of pixels in the available region. $f_W$ is an effective measure of the sky-fraction, normalized such that a top-hat mask gives $f_W = 1$. More aggressive windows remove more power, and $f_W \in [0, 1]$.

Given a window/apodization function, the amplitude of the residual leakage after correction is estimated by $R$, defined as the RMS of the relative error, averaged over a range of multipoles for all simulations, as follows:

$$R = \sqrt{\frac{1}{N_{\rm sim}\cdot\Delta\ell}\cdot\sum_{\ell=\ell_1}^{\ell_2}\sum_{i=1}^{N_{\rm sim}}\left[\frac{\widetilde{B}^i_{\rm ref}-\widetilde{B}^i_{\rm cor}}{\widetilde{B}^i_{\rm ref}}\right]^2}, \tag{5.28}$$

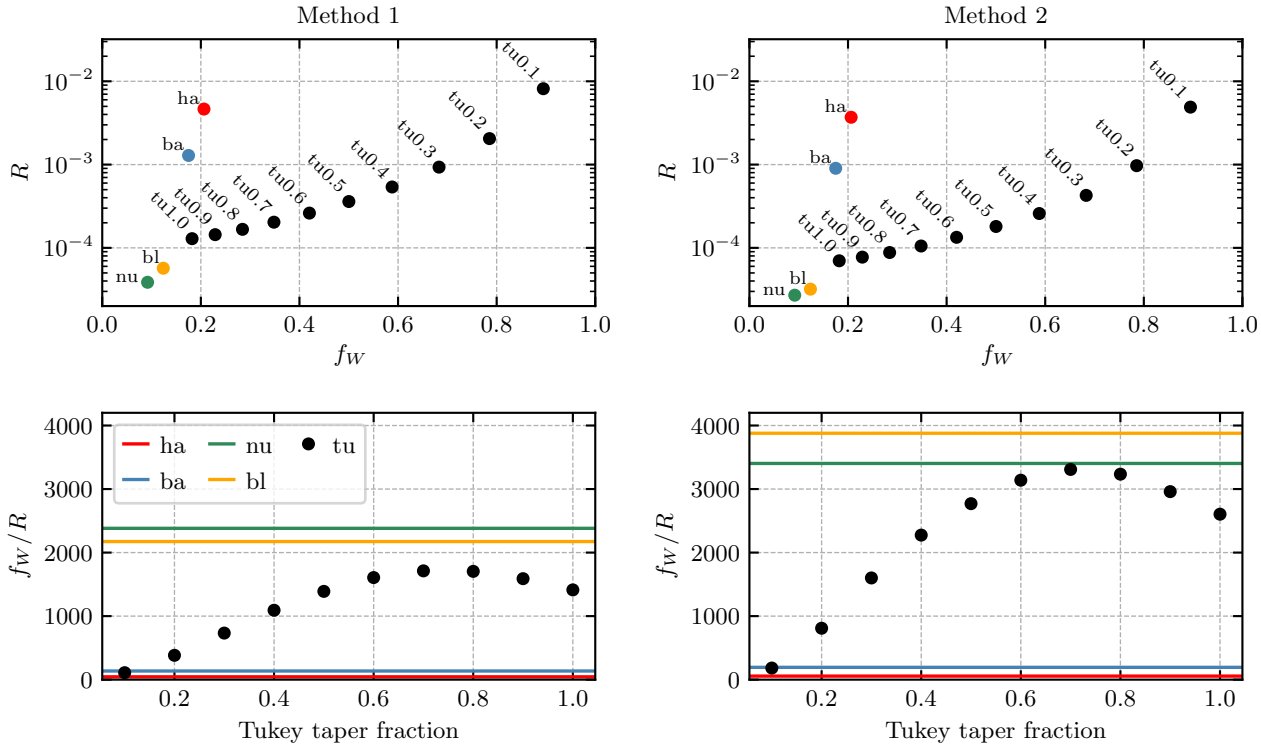


Figure 5.6 *Upper panels:* Comparison of different window functions in terms of $f_W$ (Equation 5.27) and $R$ (Equation 5.28). The labels are defined in Section 5.3.3. *Lower panels:* Ratio $f_W/R$ as a function of the taper fraction of Tukey windows, where higher values indicate better overall performance.

where $\widetilde{B}^i_{\rm ref}$ and $\widetilde{B}^i_{\rm cor}$ are the pseudo-power spectra of the apodized real and corrected $B$ maps for the $i$-th simulation, and $\Delta\ell = \ell_2 - \ell_1 + 1$. The multipole range used here is $(\ell_1, \ell_2) = (60, 120)$, including the recombination bump of the $BB$ spectrum.

A set of 14 standard window functions is employed, including 10 Tukey windows with taper fractions in increments of 0.1. For each window, I show $R$ vs. $f_W$, and the results for method 1 and method 2 are both shown in Figure 5.6. It is seen that method 2 gives smaller residual error (lower $R$) than method 1 for each posterior apodization. Furthermore, I also plot the ratio $f_W/R$ for the different window functions. This ratio is a measure of the overall performance of each window. While its exact form is arbitrary, it shoul dhighlight the tradeoff between sky fraction and residual contamination. According to this, for the mask under investigation, Tukey windows with a taper fraction of around 0.7, as well as Nuttall and Blackman windows, seem to perform best for both method 1 and 2. One can clearly see that method 2 outperforms method 1 by a factor of 2.

## 5.4 Discussion

In this work, I presented two methods (Section 5.1–5.2) that both are capable of correcting the $EB$ leakage in the pixel domain. With emphasis on one of them, various tests showed the effectiveness of these corrections, e.g., the residual error is 2–3 orders of magnitude lower than an implementation of a conventional method (the MASTER+PURE scheme). The idea of pixel domain $EB$ leakage correction is based on the idea of $EB$-family decomposition previously proposed in (Liu et al., 2018; Liu, 2018), which herewith is proved to be an extremely useful framework for the study of polarization maps.

The advantages of a correction in pixel space are many. In Section 5.3.2 our $EB$ leakage correction method was combined with MASTER, a pseudo-$C_l$ method for the reconstruction of a full-sky power spectrum. I demonstrated that the results obtained are orders of magnitude better than without explicit leakage correction.

Our method provides the possibility to be combined with any pseudo-$C_l$ or maximum likelihood method to improve their ability for $B$-mode power spectrum reconstruction.

In addition, as shown in Section 5.3.3, it is possible to further reduce the error of power spectrum reconstruction by optimizing the posterior apodization applied to the corrected $B$ map, see Figure 5.6. I there explained how to use the large library of one-dimensional window functions from digital signal processing in CMB science, which provides an easy way to explore variations two dimensional window functions.

The $EB$ leakage is driven more by large scale structures than by small scale structures, since small scale structures are locally more confined, and therefore do not propagate as far. Hence, a satisfactory correction of $EB$ leakage only requires the $E$-mode to be much larger than the $B$-mode at large scales, which is always true for the CMB — also if noise is added, given that the noise is subdominant compared with the $E$-mode signal at large scales, which will be the case for upcoming CMB missions.

The methods also enable an easy treatment of noise in power spectrum reconstructions, because in the pixel domain noise and CMB simply are added linearly to make up the total signal, and our correction methods are also linear. Therefore, the $B$-mode residual $\Delta\mathbf{B}$ after correction is simply

$$\Delta\mathbf{B} = \Delta\mathbf{B}_{\mathrm{CMB}} + \Delta\mathbf{B}_{\mathrm{noise}}. \tag{5.29}$$

In general, further removal of the noise in the pixel domain is impossible; however, if one assumes that the noise is Gaussian and uncorrelated with the CMB, then the two residual terms in equation (5.29) are independent, which means their cross covariance does not con-

tribute to the overall covariance matrix. With this assumption, one can easily remove the noise contribution to the angular spectra using one of the standard methods, by using, e.g., cross spectra (Hinshaw et al., 2003b), noise spectrum models (Planck 2013 results. XV), null maps obtained from two half-mission maps (Planck 2015 results. XI), or null maps obtained from two sub-bands (Hinshaw et al., 2003a).

To our knowledge, these two methods are the first attempt to provide solutions to the $EB$ leakage in the pixel domain. The five main obstacles in the detection of CMB $B$-modes are foreground removal, delensing, noise, systematics, and the $EB$ leakage. The present method to overcome the last also enables the more reliable investigation of $B$-mode morphology in a local sky region, opening up possibilities to have a closer look at the remaining obstacles.

CHAPTER 6

# Closing remarks

The Cosmic Microwave Background is a huge treasure chest full of stories and, maybe more importantly, riddles about the Universe we live in. Analyses of its measurements further include understanding of topics ranging from statistics, over signal processing to Galactic astrophysics. With an ever-growing CMB community it is important to keep an overview of these subjects, their relation to each other, as well as to the inferred theory which we eventually aim at.

The amount and quality of data, as well as the obtained knowledge from *Planck* is invaluable, and it is exciting to follow and participate in the advancement of future experiments and methodologies. Forecasts on how capable these experiments will be of improving on the current status quo are highly promising, but of course depend on the information with which they are fed. The great advantage of more accurate measurements is the ability to perform more thoughtful analyses — not more precise results of what already is accepted knowledge. One must be wary not bias oneself with the perhaps simplifying assumptions one was led to by insufficient data.

In this thesis, I presented studies of different aspects of CMB analysis. Particular emphasis was given to understanding Galactic foregrounds in relation to their treatment in techniques that attempt their removal. I discussed caveats of such algorithms throughout the chapters and in each of them focused on a particular question.

The first question I addressed was "Have we overlooked some foreground emission while producing CMB maps?". Based on the results shown in Chapter 2, my answer is "probably, yes". While there are still open issues, I weighed many of the *Planck* collaboration's objections. Correlations, as those shown here can indicate certain phenomena, yet the next step is to explore more physical reasons for the supposedly difficult emission within Loop I. Such investigations

might also shed light on the anomaly found in the direction of Filament IIIs, which so far is unexplained.

In addition to maps of the CMB, the *Planck* collaboration also inferred maps of foregrounds. Chapter 3 went after the question whether the different foreground products are consistent with each other, or consistent with the physical expectation one might have of their emission. The results showed striking differences in dust products and also provided further support to scrutinize the AME products. The former finding is most likely due to the simple dust model, while the latter also suffers from too few measurements at the right frequencies. Future surveys are expected to shed light on these problems.

While also of astrophysical interest, statistical investigations of Galactic foregrounds were shown also to have great relevance in regard to sufficient foreground removal, Chapter 4. As in the two previous chapters, local estimates were given special attention, as the overall anisotropy in the ISM advises against globally averaging analyses. In such local regions synchrotron emission was found to be consistent with being a Gaussian process. Subsequently the approach, as well as the results, were extended to polarization data for synchrotron and dust. In particular, distinct statistical properties of $E$- and $B$-mode signals were found, which place value on separate treatment in foreground separation methods. Such separation might be realized via ideas presented the last chapter.

If one tries to escape such questions and restricts analyses to a patch of the sky with unproblematic foreground emission, polarization leakage poses another difficulty. In chapter 5, the last chapter of my thesis, I present an approximate solution to overcome this problem. It was shown that, combined with auxiliary tools, it outmatches currently used algorithms. So far, only application to CMB polarization (or similar) is worked out. Yet, in the framework in which it is formulated, further improvements are expected, as well as applications to other areas of polarization analysis.

All these topics will occupy me for some time more. With new surveys coming up, a shift in those methods treating Galactic foreground emission will eventually become inevitable. It will be great fun developing and applying those to the data to dig for more treasures in the expanding box we live in.

# APPENDIX A

## A.1 CMB units

In Section 1 I presented various results in different units. Here, I derive how those units are related to each other. (I should also say, that for this section I restore $c$ back to its dimensionful value.)

**Surface Brightness** Out of, by now hopefully, obvious relevance to the CMB, I begin with the blackbody spectrum in its known form

$$B_\nu(T) = \frac{2h\nu^3}{c^2}\left[\exp\left(\frac{h\nu}{kT}\right) - 1\right]^{-1}, \tag{A.1}$$

where $T$ is the thermodynamic temperature. The quantity $B_\nu(T)$ describes ***surface brightness*** (i.e. "How much power does some material of a temperature $T$ emit per unit solid angle and frequency?"). Other names for the same quantity include ***spectral radiance***. This should not be confused with simply ***radiance*** (a term used in the dust community), or ***irradiance***, which both are the former integrated over all frequencies:

$$\mathcal{R}(T) = \int B_\nu(T)\,\mathrm{d}\nu. \tag{A.2}$$

**Brightness Temperature** Equation A.1 in its limit $h\nu \ll kT$, the Rayleigh-Jeans limit, reads

$$B_\nu^{\mathrm{RJ}} = \frac{2k\nu^2}{c^2}T. \tag{A.3}$$

Also in this limit, $T$ still is the thermodynamic temperature.

Solving for $T$ and *defining* the relation A.3 to hold for all frequencies and temperatures gives the ***brightness temperature***

$$T_B(\nu) = \frac{c^2}{2k\nu^2} B_\nu. \tag{A.4}$$

In the Rayleigh-Jeans limit, the brightness temperature becomes the thermodynamic temperature again.

**CMB thermodynamic temperature** The CMB fluctuation are small enough, $\Delta T_{CMB} \ll T_0$, that the blackbody formula can be linearized. Fluctuations in brightness temperature can therefore be related to fluctuations in the thermodynamic temperature around $T_0$ as

$$\Delta T_B = \frac{c^2}{2k\nu^2} \left.\frac{\partial B_\nu(T)}{\partial T}\right|_{T_0} \Delta T_{CMB} \tag{A.5}$$

$$\Rightarrow \Delta T_{CMB} = \frac{(\exp(x)-1)^2}{\exp(x)x^2} \Delta T_B. \tag{A.6}$$

The CMB thermodynamic temperature is the unit of all sky maps shown in this thesis.

## A.2 Additional tables

Table A.1 Corrected radii for the respective loops/arcs reported in Vidal et al. (2015).

| Loop/Arc | V | VI | IIIS | X | XI | XII |
|---|---|---|---|---|---|---|
| Radius [deg] | 33.6 | 36.2 | 25.0 | 33.5 | 40.5 | 55.2 |

## A.3 Additional figures

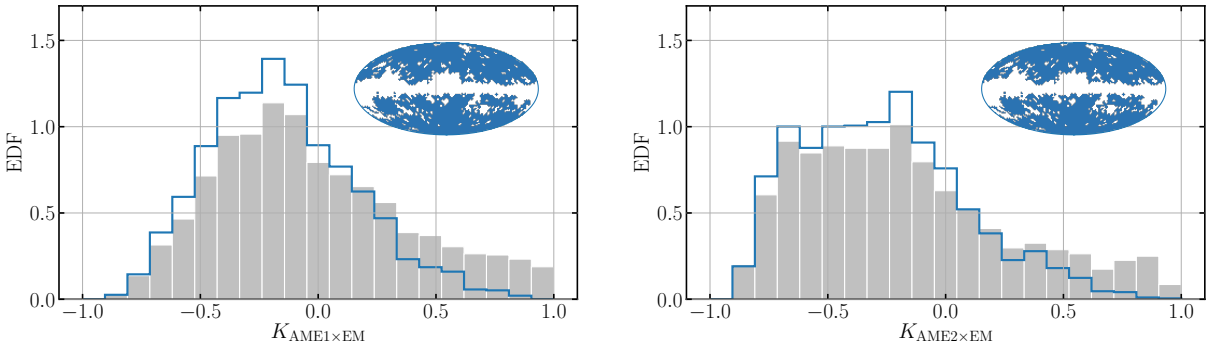


Figure A.1 Histograms of the mosaic correlations between the free-free emission measure EM and AME1 (*left panel*) and AME2 (*right panel*), as shown in Figure 3.9. The inset shows in blue those regions from which the blue distribution is plotted, corresponding to the *Planck* intensity mask. The gray histogram contains the values from the full sky.

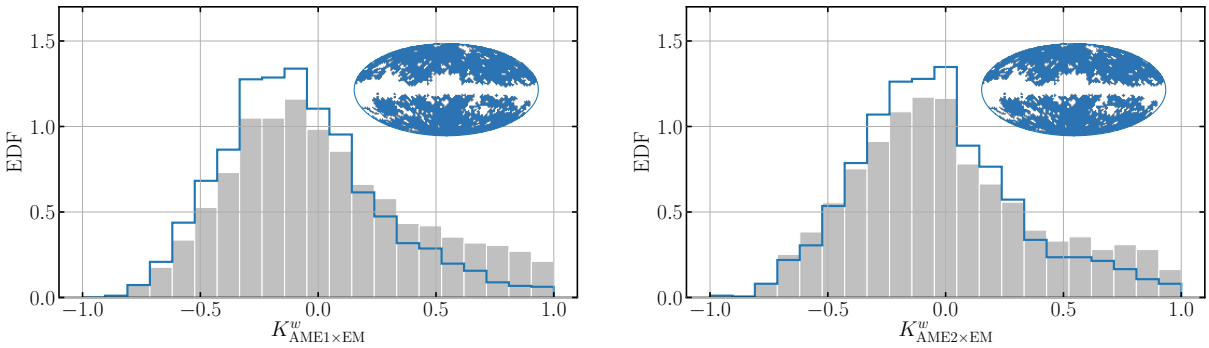


Figure A.2 Same as Figure A.1, but for weighted mosaic correlations with $n = 2$, as shown in Figure 3.11.

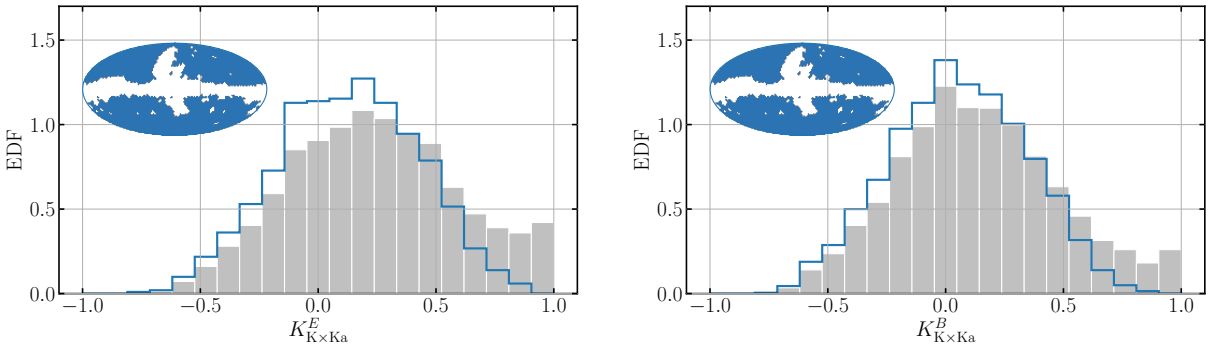


Figure A.3 Histograms of the mosaic correlations between *WMAP* K- and Ka-band *E*-mode (*left panel*) and *B*-mode maps (*right panel*), as shown in Figure 4.10. The inset shows in blue those regions from which the blue distribution is plotted, corresponding to the *WMAP* polarization mask. The gray histogram contains the values from the full sky.

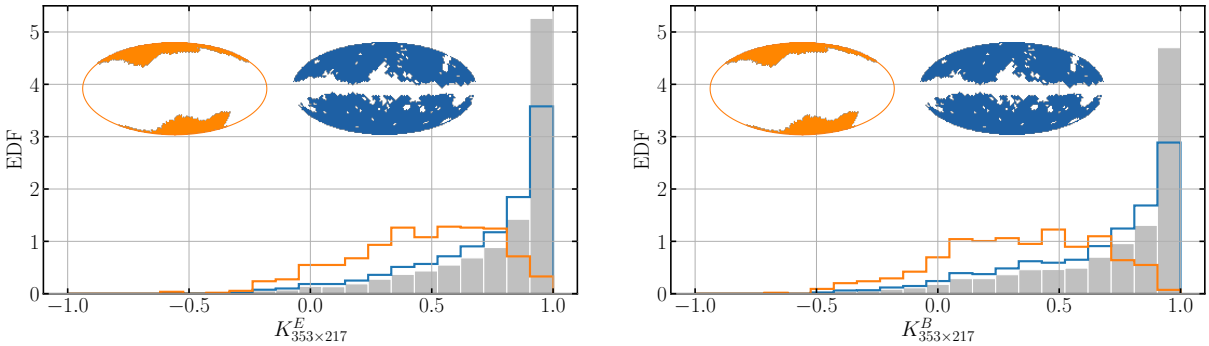


Figure A.4 Same as Fig. A.3, but for mosaic correlations between the *Planck* 353 GHz and the 217 GHz maps. The blue mask here is the *Planck* polarization mask. In addition we select patches via a more aggressive mask, the *Planck* Gal20 mask, shown in orange.

# Bibliography


Abazajian, K. N. et al. (2016). CMB-S4 Science Book, First Edition, preprint (arXiv:1610.02743).

Abergel, A. et al. (2014). Planck 2013 results. XI. All-sky model of thermal dust emission, Astron. Astrophys., 571, A11.

Abrial, P., Moudden, Y., Starck, J.-L., Fadili, J., Delabrouille, J., and Nguyen, M. K. (2008). CMB data analysis and sparsity, Statistical Methodology, 5, 289.

Adam, R. et al. (2016a). Planck 2015 results. IX. Diffuse component separation: CMB maps, Astron. Astrophys., 594, A9.

Adam, R. et al. (2016b). Planck 2015 results. X. Diffuse component separation: Foreground maps, Astron. Astrophys., 594, A10.

Adam, R. et al. (2016c). Planck intermediate results. XXX. The angular power spectrum of polarized dust emission at intermediate and high Galactic latitudes, Astron. Astrophys., 586, A133.

Ade, P. A. R. et al. (2013). Planck Intermediate Results. IX. Detection of the Galactic haze with Planck, Astron. Astrophys., 554, A139.

Ade, P. A. R. et al. (2014a). Planck 2013 results. XIII. Galactic CO emission, Astron. Astrophys., 571, A13.

Ade, P. A. R. et al. (2014b). Planck 2013 results. XV. CMB power spectra and likelihood, Astron. Astrophys., 571, A15.

Ade, P. A. R. et al. (2014c). Planck 2013 Results. XXIV. Constraints on primordial non-Gaussianity, Astron. Astrophys., 571, A24.

Ade, P. A. R. et al. (2015a). BICEP2 / Keck Array V: Measurements of B-mode Polarization at Degree Angular Scales and 150 GHz by the Keck Array, Astrophys. J., 811, 126.

Ade, P. A. R. et al. (2015b). Joint Analysis of BICEP2/*Keck Array* and *Planck* Data, Phys. Rev. Lett., 114, 101301.

Ade, P. A. R. et al. (2016a). Planck 2015 results. XVII. Constraints on primordial non-Gaussianity, Astron. Astrophys., 594, A17.

Ade, P. A. R. et al. (2016b). Planck 2015 results. XXV. Diffuse low-frequency Galactic foregrounds, Astron. Astrophys., 594, A25.

Ade, P. A. R. et al. (2017). A Measurement of the Cosmic Microwave Background $B$-Mode Polarization Power Spectrum at Sub-Degree Scales from 2 years of POLARBEAR Data, Astrophys. J., 848, 121.

Aghanim, N. et al. (2014). Planck 2013 results. XXVII. Doppler boosting of the CMB: Eppur si muove, Astron. Astrophys., 571, A27.

Aghanim, N. et al. (2016a). Planck 2015 results. XI. CMB power spectra, likelihoods, and robustness of parameters, Astron. Astrophys., 594, A11.

Aghanim, N. et al. (2016b). Planck intermediate results. XLVIII. Disentangling Galactic dust emission and cosmic infrared background anisotropies, Astron. Astrophys., 596, A109.

Aghanim, N. et al. (2017). Planck intermediate results - L. Evidence of spatial variation of the polarized thermal dust spectral energy distribution and implications for CMB B-mode analysis, Astron. Astrophys., 599, A51.

Aghanim, N. et al. (2018a). Planck 2018 results. III. High Frequency Instrument data processing and frequency maps, preprint (arXiv:1807.06207).

Aghanim, N. et al. (2018b). Planck 2018 results. VI. Cosmological parameters, preprint (arXiv:1807.06209).

Aguirre, J. et al. (2018). The Simons Observatory: Science goals and forecasts, preprint (arXiv:1808.07445).

Akrami, Y. et al. (2018a). Planck 2018 results. I. Overview and the cosmological legacy of Planck, preprint (arXiv:1807.06205).

Akrami, Y. et al. (2018b). Planck 2018 results. IV. Diffuse component separation, preprint (arXiv:1807.06208).

Akrami, Y. et al. (2018c). Planck 2018 results. XI. Polarized dust foregrounds, preprint (arXiv:1801.04945).

Ali-Haïmoud, Y., Hirata, C. M., and Dickinson, C. (2009). A refined model for spinning dust radiation, Monthly Notices of the Royal Astronomical Society, 395, 1055.

Alonso, D., Sanchez, J., and Slosar, A. Namaster: A unified pseudo-cl framework. https://github.com/LSSTDESC/NaMaster.

Alonso, D., Sanchez, J., and Slosar, A. (2018). A unified pseudo-$C_\ell$ framework, preprint (arXiv:1809.09603).

Anderson, A. J., Ade, P. A. R., Ahmed, Z., Austermann, J. E., Avva, J. S., Barry, P. S., Thakur, R. B., Bender, A. N., Benson, B. A., Bleem, L. E., Byrum, K., Carlstrom, J. E., et al. (2018). Spt-3g: A multichroic receiver for the south pole telescope, Journal of Low Temperature Physics, 193, 1057.

André, P. et al. (2014). PRISM (Polarized Radiation Imaging and Spectroscopy Mission): An Extended White Paper, JCAP, 1402, 006.

Babich, D. and Loeb, A. (2005). Polarization of 21cm radiation from the epoch of reionization, Astrophys. J., 635, 1.

Basak, S. and Delabrouille, J. (2012). A needlet internal linear combination analysis of WMAP 7-year data: estimation of CMB temperature map and power spectrum, MNRAS, 419, 1163.

Basu, A., Beck, R., Schmidt, P., and Roy, S. (2015). Synchrotron spectral index and interstellar medium densities of star-forming galaxies, MNRAS, 449, 3879.

Basu, A., Schwarz, D., Klöckner, H.-R., von Hausegger, S., Kramer, M., and Burkhart, B. (2019). Cmb foreground measurements through broad-band radio spectro-polarimetry: prospects of the ska-mpg telescope. to be published.

Baumann, D. (2011). Inflation. In *Physics of the large and the small, TASI 09, proceedings of the Theoretical Advanced Study Institute in Elementary Particle Physics, Boulder, Colorado, USA, 1-26 June 2009*, pages 523–686.

Ben-David, A., Liu, H., and Jackson, A. D. (2015a). The Kullback-Leibler Divergence as an Estimator of the Statistical Properties of CMB Maps, JCAP, 1506, 051.

Ben-David, A., von Hausegger, S., and Jackson, A. D. (2015b). Skewness and kurtosis as indicators of non-Gaussianity in galactic foreground maps, JCAP, 1511, 019.

Bennett, C. L., Banday, A. J., Górski, K. M., Hinshaw, G., Jackson, P., Keegstra, P., Kogut, A., Smoot, G. F., Wilkinson, D. T., and Wright, E. L. (1996). Four-year cobe dmr cosmic microwave background observations: Maps and basic results, The Astrophysical Journal Letters, 464, L1.

Bennett, C. L. et al. (2003). First year Wilkinson Microwave Anisotropy Probe (WMAP) observations: Preliminary maps and basic results, Astrophys. J. Suppl., 148, 1.

Bennett, C. L. et al. (2013). Nine-Year Wilkinson Microwave Anisotropy Probe (WMAP) Observations: Final Maps and Results, Astrophys. J. Suppl., 208, 20.

Bergh, S. V. and Tammann, G. A. (1991). Galactic and extragalactic supernova rates, Ann. Rev. Astron. Astrophys., 29, 363.

Berkhuijsen, E. M., Haslam, C. G. T., and Salter, C. J. (1971). Are the galactic loops supernova remnants?, A&A, 14, 252.

Blackman, R. B. and Tukey, J. W. (1958). The measurement of power spectra from the point of view of communications engineering ? part i, The Bell System Technical Journal, 37, 185.

Bouchet, F. R. et al. (2011). COrE (Cosmic Origins Explorer) A White Paper, preprint (arXiv:1102.2181).

Bunn, E. F. (2003). Separating E from B, New Astronomy Reviews, 47, 987.

Bunn, E. F. (2011). Efficient decomposition of cosmic microwave background polarization maps into pure E, pure B, and ambiguous components, PhRvD, 83, 083003.

Bunn, E. F., Zaldarriaga, M., Tegmark, M., and de Oliveira-Costa, A. (2003). E/B decomposition of finite pixelized CMB maps, Phys. Rev., D67, 023501.

Burn, B. J. (1966). On the depolarization of discrete radio sources by Faraday dispersion, MNRAS, 133, 67.

Cheng, K.-S., Chernyshov, D. O., Dogiel, V. A., Ko, C.-M., and Ip, W.-H. (2011). Origin of the fermi bubble, The Astrophysical Journal Letters, 731, L17.

Chingangbam, P., Yogendran, K. P., K., J. P., Ganesan, V., Appleby, S., and Park, C. (2017). Tensor Minkowski Functionals for random fields on the sphere, JCAP, 1712, 023.

Choi, S. K. and Page, L. A. (2015). Polarized galactic synchrotron and dust emission and their correlation, JCAP, 1512, 020.

Chu, M., Eriksen, H. K., Knox, L., Górski, K. M., Jewell, J. B., Larson, D. L., O'Dwyer, I. J., and Wandelt, B. D. (2005). Cosmological parameter constraints as derived from the Wilkinson Microwave Anisotropy Probe data via Gibbs sampling and the Blackwell-Rao estimator, PhRvD, 71, 103002.

Condon, J. J. and Random, S. M. (2016). *Essential Radio Astronomy*. Princeton University Press.

D'Agostino, R. B. (1970). Transformation to normality of the null distribution of g1, Biometrika, 57, pp. 679.

Delabrouille, J., Cardoso, J.-F., and Patanchon, G. (2003). Multidetector multicomponent spectral matching and applications for cosmic microwave background data analysis, MNRAS, 346, 1089.

Dicke, R. H., Peebles, P. J. E., Roll, P. G., and Wilkinson, D. T. (1965). Cosmic Black-Body Radiation., The Astrophysical Journal, 142, 414.

Dickinson, C., Davies, R., and Davis, R. (2003). Towards a free-free template for CMB foregrounds, MNRAS, 341, 369.

Dickinson, C. et al. (2015). Studies of Anomalous Microwave Emission (AME) with the SKA, PoS, AASKA14, 124.

Dickinson, C. et al. (2018). The State-of-Play of Anomalous Microwave Emission (AME) Research, New Astron. Rev., 80, 1.

Dobler, G., Finkbeiner, D. P., Cholis, I., Slatyer, T., and Weiner, N. (2010). The fermi haze: A gamma-ray counterpart to the microwave haze, The Astrophysical Journal, 717, 825.

Draine, B. T. (2011). *Physics of the Interstellar and Intergalactic Medium*.

Draine, B. T. and Hensley, B. (2013). Magnetic Nanoparticles in the Interstellar Medium: Emission Spectrum and Polarization, Astrophys. J., 765, 159.

Draine, B. T. and Lazarian, A. (1998). Diffuse Galactic Emission from Spinning Dust Grains, ApJL, 494, L19.

Draine, B. T. and Lazarian, A. (1998). Electric dipole radiation from spinning dust grains, The Astrophysical Journal, 508, 157.

Draine, B. T. and Lazarian, A. (1999). Magnetic Dipole Microwave Emission from Dust Grains, ApJ, 512, 740.

Draine, B. T. and Li, A. (2007). Infrared Emission from Interstellar Dust. 4. The Silicate-Graphite-PAH Model in the Post-Spitzer Era, Astrophys. J., 657, 810.

Dwek, E., Arendt, R. G., Fixsen, D. J., Sodroski, T. J., Odegard, N., Weiland, J. L., Reach, W. T., Hauser, M. G., Kelsall, T., Moseley, S. H., Silverberg, R. F., Shafer, R. A., Ballester, J., Bazell, D., and Isaacman, R. (1997). Detection and Characterization of Cold Interstellar Dust and Polycyclic Aromatic Hydrocarbon Emission, from COBE Observations, ApJ, 475, 565.

Efstathiou, G. (2004). A maximum likelihood analysis of the low cosmic microwave background multipoles from the Wilkinson Microwave Anisotropy Probe, MNRAS, 348, 885.

Eriksen, H. K., Banday, A. J., Gorski, K. M., and Lilje, P. B. (2004). Foreground removal by an internal linear combination method: Limitations and implications, Astrophys. J., 612, 633.

Eriksen, H. K., Jewell, J. B., Dickinson, C., Banday, A. J., Górski, K. M., and Lawrence, C. R. (2008). Joint Bayesian Component Separation and CMB Power Spectrum Estimation, Astrophys. J., 676, 10.

Eriksen, H. K., O'Dwyer, I. J., Jewell, J. B., Wandelt, B. D., Larson, D. L., Górski, K. M., Levin, S., Banday, A. J., and Lilje, P. B. (2004). Power Spectrum Estimation from High-Resolution Maps by Gibbs Sampling, ApJS, 155, 227.

Fermi-LAT Collaboration, Ackermann, M., et al. (2014). The spectrum and morphology of the fermi bubbles, The Astrophysical Journal, 793, 64.

Field, G. B. and Hitchcock, J. L. (1966). Cosmic black-body radiation at $\lambda$ = 2.6 mm, Phys. Rev. Lett., 16, 817.

Fields, B. D., Molaro, P., and Sarkar, S. (2014). Big-Bang Nucleosynthesis, Chin. Phys., C38, 339.

Finkbeiner, D. P. (2004a). Microwave interstellar medium emission observed by the wilkinson microwave anisotropy probe, The Astrophysical Journal, 614, 186.

Finkbeiner, D. P. (2004b). WMAP Microwave Emission Interpreted as Dark Matter Annihilation in the Inner Galaxy, arXiv, pages arXiv:astro–ph–0409027.

Fixsen, D. J. (2009). The Temperature of the Cosmic Microwave Background, ApJ, 707, 916.

Fuskeland, U., Kaplan, A., Wehus, I. K., Christensen, P. R., Eriksen, H. K., von Hausegger, S., Liu, H., Lubin, P. M., Meinhold, P. R., Naselsky, P., and Zonca, A. B-mode polarization forecasts for greenpol. in preperation.

Gautam, J. K., Kumar, A., and Saxena, R. (1996). On the modified bartlett-hanning window (family), IEEE Transactions on Signal Processing, 44, 2098.

Genova-Santos, R. et al. (2015). The QUIJOTE experiment: project overview and first results. In *11th Scientific Meeting of the Spanish Astronomical Society (SEA2014) Teruel, Spain, September 8-12, 2014*.

Gorski, K. M., Hivon, E., Banday, A. J., Wandelt, B. D., Hansen, F. K., Reinecke, M., and Bartelman, M. (2005). HEALPix - A Framework for high resolution discretization, and fast analysis of data distributed on the sphere, Astrophys. J., 622, 759.

Górski, K. M., Hivon, E., Banday, A. J., Wandelt, B. D., Hansen, F. K., Reinecke, M., and Bartelmann, M. (2005). HEALPix: A Framework for High-Resolution Discretization and Fast Analysis of Data Distributed on the Sphere, ApJ, 622, 759.

Greaves, J. S., Holland, W. S., Friberg, P., and Dent, W. R. F. (1999). Polarized co emission from molecular clouds, The Astrophysical Journal Letters, 512, L139.

Gruppuso, A., de Rosa, A., Cabella, P., Paci, F., Finelli, F., Natoli, P., de Gasperis, G., and Mandolesi, N. (2009). New estimates of the CMB angular power spectra from the WMAP 5 year low-resolution data, MNRAS, 400, 463.

Gush, H. P. and Halpern, M. (1992). Cooled submillimeter fourier transform spectrometer flown on a rocket, Review of Scientific Instruments, 63, 3249.

Gush, H. P., Halpern, M., and Wishnow, E. H. (1990). Rocket measurement of the cosmic-background-radiation mm-wave spectrum, Phys. Rev. Lett., 65, 537.

Guzmán, A. E., May, J., Alvarez, H., and Maeda, K. (2011). All-sky galactic radiation at 45 mhz and spectral index between 45 and 408 mhz, A&A, 525, A138.

Génova-Santos, R. et al. (2015). QUIJOTE scientific results – I. Measurements of the intensity and polarisation of the anomalous microwave emission in the Perseus molecular complex, Mon. Not. Roy. Astron. Soc., 452, 4169.

Harding, J. P. and Abazajian, K. N. (2010). Morphological tests of the pulsar and dark matter interpretations of the wmap haze, Phys. Rev. D, 81, 023505.

Harris, F. J. (1978). On the use of windows for harmonic analysis with the discrete fourier transform, Proceedings of the IEEE, 66, 51.

Haslam, C. G. T., Salter, C. J., Stoffel, H., and Wilson, W. E. (1982). A 408 MHz all-sky continuum survey. II. The atlas of contour maps, A&AS, 47, 1.

Hazumi, M., Borrill, J., Chinone, Y., Dobbs, M. A., et al. (2012). LiteBIRD: a small satellite for the study of B-mode polarization and inflation from cosmic background radiation detection. In *Space Telescopes and Instrumentation 2012: Optical, Infrared, and Millimeter Wave*, volume 8442 of *Proc. SPIE*, page 844219.

Hensley, B. S. and Draine, B. T. (2017). Modeling the anomalous microwave emission with spinning nanoparticles: No pahs required, The Astrophysical Journal, 836, 179.

Hensley, B. S., Draine, B. T., and Meisner, A. M. (2016). A case against spinning pahs as the source of the anomalous microwave emission, The Astrophysical Journal, 827, 45.

Hervías-Caimapo, C., Bonaldi, A., and Brown, M. L. (2016). A new model of the microwave polarized sky for CMB experiments, Mon. Not. Roy. Astron. Soc., 462, 2063.

Hill, J. C. (2018). Foreground Biases on Primordial Non-Gaussianity Measurements from the CMB Temperature Bispectrum: Implications for Planck and Beyond, Phys. Rev., D98, 083542.

Hinshaw, G., Barnes, C., Bennett, C. L., Greason, M. R., Halpern, M., Hill, R. S., Jarosik, N., Kogut, A., Limon, M., Meyer, S. S., Odegard, N., Page, L., Spergel, D. N., Tucker, G. S., Weiland, J. L., Wollack, E., and Wright, E. L. (2003a). First-Year Wilkinson Microwave Anisotropy Probe (WMAP) Observations: Data Processing Methods and Systematic Error Limits, ApJS, 148, 63.

Hinshaw, G., Spergel, D. N., Verde, L., Hill, R. S., Meyer, S. S., Barnes, C., Bennett, C. L., Halpern, M., Jarosik, N., Kogut, A., Komatsu, E., Limon, M., Page, L., Tucker, G. S., Weiland, J. L., Wollack, E., and Wright, E. L. (2003b). First-Year Wilkinson Microwave Anisotropy Probe (WMAP) Observations: The Angular Power Spectrum, ApJS, 148, 135.

Hivon, E., Górski, K. M., Netterfield, C. B., Crill, B. P., Prunet, S., and Hansen, F. (2002). MASTER of the Cosmic Microwave Background Anisotropy Power Spectrum: A Fast Method for Statistical Analysis of Large and Complex Cosmic Microwave Background Data Sets, ApJ, 567, 2.

Hooper, D., Finkbeiner, D. P., and Dobler, G. (2007). Possible evidence for dark matter annihilations from the excess microwave emission around the center of the galaxy seen by the wilkinson microwave anisotropy probe, Phys. Rev. D, 76, 083012.

Inoue, K. T., Cabella, P., and Komatsu, E. (2008). Harmonic inpainting of the cosmic microwave background sky: Formulation and error estimate, PhRvD, 77, 123539.

Irfan, M. O., Dickinson, C., Davies, R. D., Copley, C., Davis, R. J., Ferreira, P. G., Holler, C. M., Jonas, J. L., Jones, M. E., King, O. G., Leahy, J. P., Leech, J., Leitch, E. M., Muchovej, S. J. C., Pearson, T. J., Peel, M. W., Readhead, A. C. S., Stevenson, M. A., Sutton, D., Taylor, A. C., and Zuntz, J. (2015). C-Band All-Sky Survey: a first look at the Galaxy, MNRAS, 448, 3572.

Jaffe, W. and Perola, G. (1973). Dynamical Models of Tailed Radio Sources in Clusters of Galaxies, A&A, 26, 423.

Jarque, C. M. and Bera, A. K. (1980). Efficient tests for normality, homoscedasticity and serial independence of regression residuals, Economics Letters, 6, 255 .

Jelic, V. et al. (2008). Foreground simulations for the LOFAR - Epoch of Reionization Experiment, Mon. Not. Roy. Astron. Soc., 389, 1319.

Jewell, J., Levin, S., and Anderson, C. H. (2004). Application of Monte Carlo Algorithms to the Bayesian Analysis of the Cosmic Microwave Background, ApJ, 609, 1.

Jewell, J. B., Eriksen, H. K., Wandelt, B. D., O'Dwyer, I. J., Huey, G., and Górski, K. M. (2009). A Markov Chain Monte Carlo Algorithm for Analysis of Low Signal-To-Noise Cosmic Microwave Background Data, ApJ, 697, 258.

Jones, M. E., Taylor, A. C., Aich, M., Copley, C. J., Chiang, H. C., Davis, R. J., Dickinson, C., Grumitt, R. D. P., Hafez, Y., Heilgendorff, H. M., Holler, C. M., Irfan, M. O., Jew, L. R. P., et al. (2018). The c-band all-sky survey (c-bass): design and capabilities, Monthly Notices of the Royal Astronomical Society, 480, 3224.

Jung, G., Racine, B., and van Tent, B. (2018). The bispectra of galactic CMB foregrounds and their impact on primordial non-Gaussianity estimation, JCAP, 1811, 047.

Kaplinghat, M., Phalen, D. J., and Zurek, K. M. (2009). Pulsars as a source of the wmap haze, Journal of Cosmology and Astroparticle Physics, 2009, 010.

Kardashev, N. (1962). Nonstationarity of Spectra of Young Sources of Nonthermal Radio Emission, SvA, 6, 317.

Kim, J. and Naselsky, P. (2010). E/B decomposition of CMB polarization pattern of incomplete sky: a pixel space approach, A&A, 519, A104.

Kim, J., Naselsky, P., and Christensen, P. R. (2008). CMB map derived from the WMAP data through harmonic internal linear combination, Phys. Rev., D77, 103002.

Kim, J., Naselsky, P., and Mandolesi, N. (2012). Harmonic In-painting of Cosmic Microwave Background Sky by Constrained Gaussian Realization, ApJL, 750, L9.

Klaassen, C. A., Mokveld, P. J., and van Es, B. (2000). Squared skewness minus kurtosis bounded by 186/125 for unimodal distributions, Statistics & Probability Letters, 50, 131 .

Klein, U., Lisenfeld, U., and Verley, S. (2018). Radio synchrotron spectra of star-forming galaxies, A&A, 611, A55.

Kogut, A. (2012). Synchrotron spectral curvature from 22 mhz to 23 ghz, ApJ, 753, 110.

Kogut, A., Banday, A. J., Bennett, C. L., Gorski, K. M., Hinshaw, G., and Reach, W. T. (1996). High-Latitude Galactic Emission in the COBE Differential Microwave Radiometer 2 Year Sky Maps, ApJ, 460, 1.

Krachmalnicoff, N., Baccigalupi, C., Aumont, J., Bersanelli, M., and Mennella, A. (2016). Characterization of foreground emission on degree angular scales for CMB B-mode observations - Thermal dust and synchrotron signal from Planck and WMAP data, Astron. Astrophys., 588, A65.

Krachmalnicoff, N. et al. (2018). S–PASS view of polarized Galactic synchrotron at 2.3 GHz as a contaminant to CMB observations, Astron. Astrophys., 618, A166.

Kun, M. (2007). The enigmatic loop III and the Local Galactic Structure. In Elmegreen, B. G. and Palous, J., editors, *Triggered Star Formation in a Turbulent ISM*, volume 237 of *IAU Symposium*, pages 119–123.

Lawson, K. D., Mayer, C. J., Osborne, J. L., and Parkinson, M. L. (1987). Variations in the Spectral Index of the Galactic Radio Continuum Emission in the Northern Hemisphere, MNRAS, 225, 307.

Lazarian, A. and Draine, B. T. (2000). Resonance paramagnetic relaxation and alignment of small grains, The Astrophysical Journal Letters, 536, L15.

Leitch, E. M., Readhead, A. C. S., Pearson, T. J., and Myers, S. T. (1997). An Anomalous component of galactic emission, Astrophys. J., 486, L23.

Lewis, A. (2003). Harmonic E/B decomposition for CMB polarization maps, PhRvD, 68, 083509.

Lewis, A. and Bridle, S. (2002). Cosmological parameters from CMB and other data: A Monte Carlo approach, PhRvD, 66, 103511.

Lewis, A., Challinor, A., and Turok, N. (2002). Analysis of CMB polarization on an incomplete sky, PhRvD, 65, 023505.

Linden, T. and Profumo, S. (2010). Systematic effects in extracting a "gamma-ray haze" from spatial templates, The Astrophysical Journal Letters, 714, L228.

Liu, H. (2018). Fingerprint of Galactic Loop I on polarized microwave foregrounds, Astron. Astrophys., 617, A90.

Liu, H. (2018). Fingerprint of Galactic Loop I on polarized microwave foregrounds, A&A, 617, A90.

Liu, H., Creswell, J., and Naselsky, P. (2018). E and B families of the Stokes parameters in the polarized synchrotron and thermal dust foregrounds, JCAP, 5, 059.

Liu, H., Creswell, J., von Hausegger, S., and Naselsky, P. (2018). Methods for pixel domain correction of EB leakage, preprint (arXiv:1811.04691).

Liu, H., Mertsch, P., and Sarkar, S. (2014). Fingerprints of Galactic Loop I on the Cosmic Microwave Background, Astrophys. J., 789, L29.

Liu, H., von Hausegger, S., and Naselsky, P. (2017). Towards understanding the Planck thermal dust models, Phys. Rev., D95, 103517.

Louis, T. et al. (2017). The Atacama Cosmology Telescope: Two-Season ACTPol Spectra and Parameters, JCAP, 1706, 031.

Mather, J. C., Cheng, E. S., Eplee, Jr., R. E., Isaacman, R. B., Meyer, S. S., Shafer, R. A., Weiss, R., Wright, E. L., Bennett, C. L., Boggess, N. W., Dwek, E., Gulkis, S., Hauser, M. G., Janssen, M., Kelsall, T., Lubin, P. M., Moseley, Jr., S. H., Murdock, T. L., Silverberg, R. F., Smoot, G. F., and Wilkinson, D. T. (1990a). A preliminary measurement of the cosmic microwave background spectrum by the Cosmic Background Explorer (COBE) satellite, The Astrophysical Journal, 354, L37.

Mather, J. C., Cheng, E. S., Eplee, Jr., R. E., Isaacman, R. B., Meyer, S. S., Shafer, R. A., Weiss, R., Wright, E. L., Bennett, C. L., Boggess, N. W., Dwek, E., Gulkis, S., Hauser, M. G., Janssen, M., Kelsall, T., Lubin, P. M., Moseley, Jr., S. H., Murdock, T. L., Silverberg, R. F., Smoot, G. F., and Wilkinson, D. T. (1990b). A preliminary measurement of the cosmic microwave background spectrum by the Cosmic Background Explorer (COBE) satellite, ApJL, 354, L37.

McKellar, A. (1941). Molecular Lines from the Lowest States of Diatomic Molecules Composed of Atoms Probably Present in Interstellar Space, Publications of the Dominion Astrophysical Observatory Victoria, 7.

Mertsch, P. and Sarkar, S. (2010). Systematic effects in the extraction of the 'WMAP haze', J. Cosmol. Astropart. Phys., 2010, 019.

Mertsch, P. and Sarkar, S. (2011). Fermi gamma-ray "bubbles" from stochastic acceleration of electrons, Phys. Rev. Lett., 107, 091101.

Mertsch, P. and Sarkar, S. (2013). Loops and spurs: The angular power spectrum of the Galactic synchrotron background, JCAP, 1306, 041.

Molinari, D., Gruppuso, A., Polenta, G., Burigana, C., De Rosa, A., Natoli, P., Finelli, F., and Paci, F. (2014). A comparison of CMB angular power spectrum estimators at large scales: the TT case, MNRAS, 440, 957.

Mukhanov, V. F. (2004a). CMB-slow, or how to estimate cosmological parameters by hand, Int. J. Theor. Phys., 43, 623.

Mukhanov, V. F. (2004b). Nucleosynthesis without a computer, Int. J. Theor. Phys., 43, 669.

Nuttall, A. (1981). Some windows with very good sidelobe behavior, IEEE Transactions on Acoustics, Speech, and Signal Processing, 29, 84.

Pacholczyk, A. (1970). *Radio astrophysics. Nonthermal processes in galactic and extragalactic sources.*

Paladino, R., Murgia, M., and Orrú, E. (2009). Radio spectral index images of the spiral galaxies NGC 0628, NGC 3627, and NGC 7331, A&A, 503, 747.

Pearson, K. (1916). Mathematical contributions to the theory of evolution. xix. second supplement to a memoir on skew variation, Phil. Trans. R. Soc. A, 216, 429.

Peebles, P. J. E. (1966). Primordial Helium Abundance and the Primordial Fireball. II, ApJ, 146, 542.

Penzias, A. A. and Wilson, R. W. (1965). A Measurement of Excess Antenna Temperature at 4080 Mc/s., The Astrophysical Journal, 142, 419.

Platania, P., Caserini, E., Maino, D., Burigana, C., Bersanelli, M., Cappellini, B., and Mennella, A. (2003). Full sky study of diffuse galactic emission at long wavelengths, Astron. Astrophys., 410, 847.

Polenta, G., Marinucci, D., Balbi, A., de Bernardis, P., Hivon, E., Masi, S., Natoli, P., and Vittorio, N. (2005). Unbiased estimation of an angular power spectrum, JCAP, 11, 001.

Puglisi, G., Fabbian, G., and Baccigalupi, C. (2017). A 3D model for carbon monoxide molecular line emission as a potential cosmic microwave background polarization contaminant, Mon. Not. Roy. Astron. Soc., 469, 2982.

Rana, S., Ghosh, T., Bagla, J. S., and Chingangbam, P. (2018). Non-Gaussianity of diffuse Galactic synchrotron emission at 408 MHz, Mon. Not. Roy. Astron. Soc., 481, 970.

Remazeilles, M., Delabrouille, J., and Cardoso, J.-F. (2011). Foreground component separation with generalized Internal Linear Combination, MNRAS, 418, 467.

Remazeilles, M., Dickinson, C., Banday, A. J., Bigot-Sazy, M. A., and Ghosh, T. (2015). An improved source-subtracted and destriped 408 MHz all-sky map, Mon. Not. Roy. Astron. Soc., 451, 4311.

Rogers, K. K., Peiris, H. V., Leistedt, B., McEwen, J. D., and Pontzen, A. (2016). SILC: a new Planck Internal Linear Combination CMB temperature map using directional wavelets, Mon. Not. Roy. Astron. Soc., 460, 3014.

Rohatgi, V. K. and Székely, G. J. (1989). Sharp inequalities between skewness and kurtosis, Statistics & Probability Letters, 8, 297 .

Roll, P. G. and Wilkinson, D. T. (1966). Cosmic background radiation at 3.2 cm-support for cosmic black-body radiation, Phys. Rev. Lett., 16, 405.

Rotti, A. and Huffenberger, K. (2018). Real-space computation of $E/B$-mode maps I: Formalism, Compact Kernels, and Polarized Filaments, preprint, (arXiv:1807.11940).

Rotti, A. and Huffenberger, K. (2018). Real-space computation of $E/B$-mode maps I: Formalism, Compact Kernels, and Polarized Filaments, preprint (arXiv:1807.11940).

Rubino-Martin, J. A. et al. (2010). The QUIJOTE CMB Experiment. In *Proceedings, 8th Scientific Meeting of the Spanish Astronomical Society - Highlights of Spanish Astrophysics V: Santander, Cantabria, Spain, July 7-11, 2008*, pages 127–135.

Saha, R., Jain, P., and Souradeep, T. (2006). A Blind Estimation of the Angular Power Spectrum of CMB Anisotropy from WMAP, ApJL, 645, L89.

Schwarz, D. J., Copi, C. J., Huterer, D., and Starkman, G. D. (2016). CMB Anomalies after Planck, Class. Quant. Grav., 33, 184001.

Sheehy, C. and Slosar, A. (2018). No evidence for dust B-mode decorrelation in Planck data, Phys. Rev., D97, 043522.

Silsbee, K., Ali-Haïmoud, Y., and Hirata, C. M. (2011). Spinning dust emission: the effect of rotation around a non-principal axis, Monthly Notices of the Royal Astronomical Society, 411, 2750.

Smith, K. M. (2006). Pseudo-$C_\ell$ estimators which do not mix E and B modes, PhRvD, 74, 083002.

Smith, K. M. and Zaldarriaga, M. (2007). General solution to the E-B mixing problem, PhRvD, 76, 043001.

Sokoloff, D. D., Bykov, A. A., Shukurov, A., Berkhuijsen, E. M., Beck, R., and Poezd, A. D. (1998). Depolarization and Faraday effects in galaxies, MNRAS, 299, 189.

Starck, J.-L., Fadili, M. J., and Rassat, A. (2013). Low-$l$ CMB analysis and inpainting, A&A, 550, A15.

Su, M., Slatyer, T. R., and Finkbeiner, D. P. (2010). Giant gamma-ray bubbles from fermi-lat: Active galactic nucleus activity or bipolar galactic wind?, The Astrophysical Journal, 724, 1044.

Sunyaev, R. A. and Chluba, J. (2008). The Richness and Beauty of the Physics of Cosmological Recombination, ASP Conf. Ser., 395, 35.

Taylor, A. C. (2018). The C-Band All-Sky Survey, preprint (arXiv:1805.05484).

Tegmark, M. (1997). How to measure CMB power spectra without losing information, PhRvD, 55, 5895.

Tegmark, M. and Efstathiou, G. (1996). A method for subtracting foregrounds from multi-frequency cmb sky maps, Mon. Not. Roy. Astron. Soc., 281, 1297.

Thaddeus, P. and Clauser, J. F. (1966). Cosmic microwave radiation at 2.63 mm from observations of interstellar cn, Phys. Rev. Lett., 16, 819.

Verkhodanov, O. V., Khabibullina, M. L., and Majorova, E. K. (2009). Tessellated Mapping of Cosmic Background Radiation Correlations and Source Distributions, Astrophys. Bull., 64, 263.

Vidal, M., Dickinson, C., Davies, R. D., and Leahy, J. P. (2015). Polarized radio filaments outside the Galactic plane, Mon. Not. Roy. Astron. Soc., 452, 656.

von Hausegger, S., Gammelgaard Ravnebjerg, A., and Liu, H. (2018). Statistical properties of polarized CMB foreground maps, arXiv e-prints, .

von Hausegger, S. and Liu, H. (2015). The Morphology of the Anomalous Microwave Emission in the Planck 2015 data release, JCAP, 1508, 029.

von Hausegger, S., Liu, H., Mertsch, P., and Sarkar, S. (2016). Footprints of Loop I on Cosmic Microwave Background Maps, JCAP, 1603, 023.

Weiland, J. L., Osumi, K., Addison, G. E., Bennett, C. L., Watts, D. J., Halpern, M., and Hinshaw, G. (2018). Effect of Template Uncertainties on the WMAP and Planck Measures of the Optical Depth Due To Reionization, archive.

Weinberg, S. (2008). *Cosmology*. Oxford, UK: Oxford Univ. Pr. (2008) 593 p.

Zacchei, A. et al. (2011). Planck Early Results. V. The Low Frequency Instrument data processing, Astron. Astrophys., 536, A5.

Zaldarriaga, M. (1998). Cosmic microwave background polarization experiments, The Astrophysical Journal, 503, 1.

Zaldarriaga, M. (2004). The Polarization of the Cosmic Microwave Background, Measuring and Modeling the Universe, page 309.

Zaldarriaga, M. and Seljak, U. c. v. (1997). All-sky analysis of polarization in the microwave background, Phys. Rev. D, 55, 1830.

Zel'dovich, Y. (1965). Survey of modern cosmology. volume 3 of *Advances in Astronomy and Astrophysics*, pages 241 – 379. Elsevier.

Zhao, W. and Baskaran, D. (2010). Separating $e$ and $b$ types of polarization on an incomplete sky, Phys. Rev. D, 82, 023001.

# List of Figures


1.1 Measurements of the CMB blackbody spectrum . . . . . 13
1.2 COBE sky maps . . . . . 14
1.3 *Planck* foreground spectra and 100 GHz sky map . . . . . 24
1.4 *Planck* SMICA map and temperature power spectrum . . . . . 30
1.5 CMB polarization power spectra . . . . . 31
1.6 Dust polarization power spectra . . . . . 37
1.7 Map of the Microwave Haze . . . . . 41
1.8 *Planck* HFI spectral bands . . . . . 41

2.1 Haslam 408 MHz map with indicated radio loops . . . . . 45
2.2 *Planck* 30 GHz polarization intensity map with indicated loops and filaments . 46
2.3 *Planck* 30 GHz $E$- and $B$-mode maps . . . . . 47
2.4 Model and profile for Loop I . . . . . 50
2.5 CMB Correlation angles and *Planck* SMICA map with indicated radio loops . . 50
2.6 Latitudinal column density profile of Galactic loops . . . . . 53
2.7 Sketch of polarized filaments . . . . . 57
2.8 Close-up of Loop IIIs . . . . . 61

3.1 *Planck* thermal dust emission parameter maps . . . . . 68
3.2 *Planck* thermal dust emission parameter power spectra . . . . . 70
3.3 *Planck* thermal dust emission parameter distributions . . . . . 70
3.4 *Planck* thermal dust emission parameter correlations . . . . . 71
3.5 *Planck* thermal dust emission intensity ratios . . . . . 72
3.6 *Planck* thermal dust emission parameter correlations, BICEP zone . . . . . 73
3.7 *Planck* thermal dust emission parameter correlations, GreenPol zone . . . . . 73

3.8 *Planck* thermal dust emission intensities at 80 GHz . . . . . 75
3.9 Mosaic correlations of AME and free-free EM maps . . . . . 79
3.10 Foreground weight maps . . . . . 82
3.11 Weighted mosaic correlations of AME and free-free EM maps . . . . . 82

4.1 Skewness and Kurtosis histogram for uncorrelated random and CMB simulations 92
4.2 Skewness and Kurtosis histogram for SMICA . . . . . 94
4.3 Significances SMICA; distribution and map . . . . . 95
4.4 Skewness and kurtosis histograms of Haslam and Haslam simulations . . . . . 96
4.5 Significances Haslam; distribution and map . . . . . 97
4.6 Haslam 408 MHz map with indicated patch locations . . . . . 98
4.7 Three example patches from Haslam map . . . . . 99
4.8 Significances *WMAP* K-band map; $E$- and $B$-modes . . . . . 104
4.9 Significances *Planck* 353 GHz map; $E$- and $B$-modes . . . . . 105
4.10 Mosaic correlations for synchrotron and dust polarizations . . . . . 106

5.1 Sketch of masked map . . . . . 116
5.2 $EB$ leakage corrections; belt mask . . . . . 119
5.3 $EB$ leakage corrections; disk mask . . . . . 120
5.4 $EB$ leakage corrections and power spectra; disk mask . . . . . 123
5.5 Comparison of two $EB$ leakage corrections . . . . . 125
5.6 RMS from $EB$ leakage corrections with different apodizations . . . . . 127

A.1 Histograms of mosaic correlations $K_{\mathrm{AME1\times EM}}$ and $K_{\mathrm{AME2\times EM}}$ . . . . . 136
A.2 Histograms of mosaic correlations $K^{w}_{\mathrm{AME1\times EM}}$ and $K^{w}_{\mathrm{AME2\times EM}}$ . . . . . 136
A.3 Histograms of mosaic correlations $K^{E}_{\mathrm{K\times Ka}}$ and $K^{B}_{\mathrm{K\times Ka}}$ . . . . . 137
A.4 Histograms of mosaic correlations $K^{E}_{353\times 217}$ and $K^{B}_{353\times 217}$ . . . . . 137

# List of Tables

2.1 *Two left columns:* The mean temperature in a ±2° band along Loop I and the corresponding chance probabilities in various CMB maps. *Two right columns:* The cross-correlation $C(d,T)$ between the distance of pixels and their temperature value in a ±10° band along Loop I. . . . . 52

2.2 $p$-values of statistical moments calculated on the unmasked and the masked SMICA map with $\ell \leq 20$. (Probability of finding the computed value or *higher*) 58

2.3 Correlation values and corresponding $p$-values calculated on the masked SMICA map with $\ell \leq 20$. (Probability of finding the computed value or *lower*) . . . . . 59

3.1 Differences in the *Planck* thermal dust emission products. The last column indicates whether the CIB was treated separately in the fitting or not. . . . . 66

3.2 Monopoles and standard deviations for the various full-sky parameter maps . . 69

3.3 Correlation values for the T-T plots of Figure 3.4 . . . . . 71

A.1 Corrected radii for the respective loops/arcs reported in Vidal et al. (2015). . . 135

## More Acknowledgements

This thesis presents results based on observations obtained with Planck (http://www.esa.int/Planck), an ESA science mission with instruments and contributions directly funded by ESA Member States, NASA, and Canada. I further acknowledge the use of the NASA Legacy Archive for Microwave Background Data Analysis (LAMBDA), as well as the Planck Legacy Archive. I have also made extensive use of HEALPix (Górski et al., 2005) in its python implementation HEALPY (https://github.com/healpy/healpy).

This work was funded in part by the Danish National Research Foundation (DNRF) and by Villum Fonden through the Deep Space project.